Spatial data focusing using direct sequence spread spectrum modulation

Michael Derrick Odhiambo

SORBONNE UNIVERSITÉ

DOCTORAL THESIS

Spatial Data Focusing Using Direct Sequence Spread Spectrum Modulation

Author:
Michael Derrick ODHIAMBO

Supervisor:
Dr. Julien SARRAZIN
co-supervisor:
Prof. Phillipe De DONCKER

A thesis submitted in fulfillment of the requirements for the degree of Doctor of Philosophy

in the

Group of electrical engineering, Paris (GeePs)
Faculty of Science and Engineering

M. Nel SAMAMA - Professor Institut Mines-Télécom / Telecom SudParis	Rapporteur
M. Alain SIBILLE - Professor at Telecom Paris	Rapporteur
M. Sebastien TIXEUIL - Professor at Sorbonne University, LIP6	Membre du jury
M. Philippe De DONCKER - Professor at the Université Libre de Bruxelles (ULB)	Co-encadrant
M. Julien SARRAZIN, Maitre de Conférences (HDR), Sorbonne Université	Directeur de thèse

This work is dedicated to people. Those that waited for me as I pursued my dreams. To my mother. To my boy Hawi and niece Amor, that one day you may read it just for inspiration

"It's not that I'm so smart, it's just that I stay with problems longer"

Albert Einstein

SORBONNE UNIVERSITÉ

Abstract

Faculty Name
Faculty of Science and Engineering

Doctor of Philosophy

Spatial Data Focusing Using Direct Sequence Spread Spectrum Modulation

by Michael Derrick ODHIAMBO

This work proposes the implementation of Spatial Data Focusing (SDF) using spread spectrum techniques. SDF was recently proposed as a candidate alternative to classical power focusing schemes in wireless geocasting applications. Unlike power focusing approaches where radiated power is directed to a defined direction, in SDF, it is the data to be transmitted that is processed in such a manner that it can only be decoded at a predefined location. This work exploits the dual orthogonality due to classical quadrature components and orthogonal Gold spreading sequences to design the IQ and spread spectrum based spatial data focusing (DSSS-SDF-IQ) scheme. It is demonstrated that SDF attains better spatial selectivity than classical power focusing for a given antenna array size. The robustness of the proposed scheme is subsequently demonstrated by implementing it over a classical Urban Canyon 6-ray multipath channel model, where it is shown that the scheme can exhibit beamwidth as narrow as 1° with only a 4-antenna array. In SDF, the beamwidth is defined as the area within which data can be decoded as opposed to classical half power beamwidth.

Acknowledgements

I would like to thank my supervisor, Dr. Julien Sarrazin, for the patient guidance, encouragement and advice he has provided throughout my time as his student. I have been extremely lucky to have a supervisor who cared so much about my work, and who took upon himself to hold my hands through the doctoral studies jungle. Getting into the system with a mindset that integrated ideas and solved problems from a purely technical perspective, you inculcated into me the 'scientific perspective'. You sacrificed some of your most precious times (including family times) to guide my work. Thank you. My co-supervisor, Prof. Phillipe de Doncker, thanks for the invitation to stay over in Belgium, the regular meeting at the OPERA group were such an eye opener and gave me a different perspective of research group dynamics, enriching my overall experience. Most of all your candid perspectives on my research work were really appreciated.

I would also like to thank Prof. Nel Samama, and Prof. Alain Sibille not only for accepting to be part of my jury but also taking their time to actually review my work. Again thanks to the jury in its entirety, Prof. Nel Samama, Prof. Alain Sibille, Prof. Sebastian Tixeuil, Prof. Phillipe De Doncker and Dr. Julien Sarrazin, your time and effort is highly appreciated.

The research team, specifically Guylian Molineaux and Sidney Golstein, I owe you, you guys are brilliant and the exchanges we had were my best. Thank you guys. I know your PhD journeys will go very far, wishing you all the very best.

The team at L2E labs (currently GeePs), thank you. Naturally I am a very introverted and silent person, I came out of the Lab a different person. The coffee breaks and the beer breaks, memorable. Did we celebrate new year three times? Chinese new year, Persian new year, and the 'new year' new year. Taro, actually I never adapted to that game, ping pong (in Kenya we called it Table Tennis), coffee, and more coffee, thank you. Speaking of coffee, reminds me of Chloe. Merci Chloé pour tout votre soutien administratif and Pascal for all IT questions.

My office mates. Tianyu, Rudy and Ousamma, how quick time moves. Thanks guys.

Contents

List of Figures

List of Tables

List of Abbreviations

AoA	Angle of Arrival
AF	Array Factor
ARFZ	Adaptive Rectangular Forwarding Zone
ALGS	AT & T Labs Geocast System
ACF	auto-correlation function
C2C-CC	CAR-2-CAR Communication Consortium
CSI	channel state information
CD-P	Centre Distance Priority
DSSS	Direct Sequence Spread Spectrum
DOA	Direction of Arrival
DM	Directional Modulation
DSSS-SDF	Direct Sequence Spread Spectrum - Spatial Data Focusing
DSSS-SDF-IQ	Direct Sequence Spread Spectrum - Spatial Data Focusing with IQ
DENM	Decentralized Environment Notification Message
FRFZ	Fixed Rectangular Forwarding Zone
GA	Geographic Addressing
GNSS	Global Navigation Satellite System
GPSR	Greedy Perimeter Stateless Routing
GPS	Global Positioning System
GBSBM	Geometrically Based Single Bounce Macrocell
HPBW	Half Power Beamwidth
ITS	Intelligent Transport Systems
IoT	Internet-of-Things
I2V	Infrastructure to Vehicle
LAN	Local Area Network
LTE	Long Term Evolution
LBPA	Location-Based PinBoard Application
LFSR	Linear Feedback Shift Registers
LOS	Line of Sight
MANET	Mobile Ad-hoc Networks
MPC	multipath components

PCN	Progressively Closer Nodes
PN	Pseudo-Noise
PA	power allocation
RLS	Reactive Location Service
RT	ray-tracing
SDF	Spatial Data Focusing
TR	Time Reversal
TCP/IP	Transmission Control Protocol/Internet Protocol
TOA	Time-of-Arrival
VANET	Vehicular Ad-hoc Networks
V2V	Vehicle to Vehicle
V2I	Vehicle to Infrastructure
ZOR	Zone of Relevance
ZOF	Zone of Forwarding

Executive Summary

The ability to carry out wireless broadcast of data to predefined spatial locations, *geocasting*, is an active research subject in the advent of 5G and Internet of Things (IoT) technologies [1]. Geocasting can significantly enhance performance of location dependent technologies and applications in the fields of intelligent transport systems (ITS), tourist guide systems, and day to day navigation activities of physically challenged persons in smart city environments, e.g., by provision of accurate location-specific guiding information for the visually impaired. The main goal of wireless geocasting schemes is to enable base stations to broadcast data to predefined locations such that receivers can only decode the transmitted data if they locate themselves within the predefined locations. Classically, this can be implemented via spatial filtering using phased array antennas. However, this approach has certain limitations, key being the required infrastructure, i.e., to be able to illuminate with narrow beams. Indeed, spatial filtering requires the size of the antenna aperture to proportionally increase as the required beamwidth decreases [2]. In view of this limitation, Spatial Data Focusing (SDF) was proposed as a candidate alternative scheme to classical beamforming for wireless *geocasting* applications [3]. SDF seeks to attain enhanced wireless geocasting spatial selectivity at reduced infrastructural cost.

Classical spatial filtering employs complex weighting to electronically steer a beam to a targeted direction or suppress reception from unwanted directions. Its implementation may take an analogue, digital, or hybrid system approach. Whereas the digital approach may exploit Software Defined Radio (SDR) capabilities, they become prohibitive as the number of antennas increases too much because of multiple power hungry ADCs [4]. In SDF, narrow beamwidth can be achieved with a limited number of antennas as shown in this work, which enable lowering the implementation cost and power consumption of wireless geocasting.

Chapter 1 introduces the concept of geocasting, a technique that enables broadcast of data to predefined physical (geographical) locations. It abords the concepts of geographic addressing and geographic routing protocols. It then looks at existing (or proposed) implementation of geocasting in wireless applications. Three research works are particularly discussed which well represent the specificity of geocasting in wireless networks, i.e., the car-to-car and the FleetNet projects, which focus on developing last mile wireless access for Vehicular Ad-hocNetworks (VANET), and the AT & T Labs Geocast System (ALGS) Mobile Ad-hoc Networks (MANET) application. All the three do employ geocasting techniques to broadcast data to predefined location.

Chapter 2 reviews the different techniques that can give directional capabilities to base stations. Since many of them use antenna arrays, we first introduce the necessary background on antenna array theory to illustrate the fundamental limitation of power focusing. Then a state-of-the-art of two main approaches to exploit multiple antenna system to achieve directional properties is drawn. In particular beamforming and Directional Modulation (DM) techniques are detailed. The single-antenna-compatible technique, namely Time Reversal (TR), is also discussed. Finally, the main limitations of such approaches are summarized.

Chapter 3 introduced the concept of direct sequence spread spectrum based spatial data focusing. Its general framework is outlined, and analysis done in the real domain to both understand the mechanism behind the spatial selectivity ability of the proposed scheme, and for purposes of proof of concept. A general review of orthogonal signaling is also discussed, this being at the core of the SDF approach. Subsequently the Direct Sequence Spread Spectrum - Spatial Data Focusing (DSSS-SDF) approach that incorporated the IQ domain as an added degree of freedom is introduced. It is demonstrated that adding this degree of freedom enables efficient channel estimation and equalization at the receiver. The main feature is that SDF achieves much narrower beams than BF and that a number of antennas as low as 4 is sufficient to achieve beamwidths of about 1°. In both the real case and IQ-based scenario, simulations are carried out to demonstrate the robustness of the proposed scheme. In all the simulations in this section, a pure LOS scenario has been considered.

Chapter 4 investigates the influence of multipath channel environments on SDF and to an extension the robustness of the SDF scheme in such an environment. Firstly the general multipath resolution ability of typical DSSS communication system is discussed and the a numerical review of the proposed DSSS-SDF-IQ scheme as implemented over a general multipath environment. After this the characterization of wireless communication channels using ray tracing techniques is carried out. This leads to the introduction of the aspects of DSSS-SDF-IQ over urban canyon channel model. Here, three channel models are investigated, they include, the 2-ray ground reflected model, 4-ray, and 6-ray urban canyon models. This chapter ends with the investigation of the influence of space-time geometrical channel models on SDF, focusing on the GBSBM. Here we analyze the performance of SDF under macrocell environments.

Indeed for all the cases studied above, relevant simulations are implemented to validate the discussions. The results obtained generally demonstrated that the Direct Sequence Spread Spectrum - Spatial Data Focusing with IQ (DSSS-SDF-IQ) scheme is robust, both in ideal LOS environments and multipath propagation scenarios.

Chapter 5 finally ends the work with a conclusion and some perspective on possible future research directions.

Chapter 1

Geocasting

Associating wireless information to certain physical locations is an interesting feature that many applications benefit from. People can receive information related to the place where they are. Whether to enrich navigation applications by indicating where to find the nearest cafe or to broadcast alerts related to severe weather conditions, location-based services have considerably grown in the last decade.

Typical applications that make use of the relationship between content and location include: provision of location-based announcements, e.g., planned local information dissemination and alerts, including in emergency response scenarios to enhance search and rescue and public safety; location-specific resource discovery e.g., delivery of information to tourists/visitors at places of interest like museums; provision of maps for navigation; and local traffic information.

The technology that enables addressing users according to their location is known as geocasting and can be implemented with a number of different techniques depending on the type of network that is considered and the performance that are required.

1.1 Context

1.1.1 Geocasting concept

Geocasting is a technique that enables broadcast of data to predefined physical (geographical) locations. It can be deployed over existing Transmission Control Protocol/Internet Protocol (TCP/IP) networks, *ad-hoc* networks, or a tiered combination of the two. This technique has attracted active research in the recent past, specifically in the location-dependent applications sector[1]. These work focus on the potential of geocasting in the last mile wireless network, which is a very attractive prospect in the advent of 5G and IoT developments. Geocasting techniques have been extensively studied in literature, introducing various implementation approaches [5, 6, 7, 8, 9, 10, 11]. Currently, implementation of geocasting systems depend on stable *geographic routing protocols* to ensure reliable and timely packet delivery to predefined geographical locations. To do so, two main approaches exist, namely, Geographic Addressing (GA) and geographic routing.

Geographical Addressing

GA refers to communication protocols that allow a sender to specify the intended recipients of a message by its location in physical space, specified either as a geometric space, a function of longitudes and latitudes, or a combination of the two. This is to be contrasted with traditional addressing schemes, such as IP addressing where device addresses are specified by an integer that locates them within the Internet's

hierarchical system of subnetworks [12]. Note that, GA does not refer to a particular device or set of devices that is fixed for all time; typically, the sending device does not know in advance which, if any, devices lie in the specified area. The address in this case, thus refers exactly to the set of devices that are in the area at the time the message is transferred, a set characterized by constant change with time [13].

Geographic Routing

Geographic routing protocols are modalities defined to facilitate the selection of efficient ways/paths to transmit packets from a sender to a predefined Zone of Relevance (ZOR) [8, 9], the sender may not have prior knowledge of the presence or none of receiving nodes in the ZOR. It is assumed that nodes in the network know their own location, that of their neighbours, and the destination's location. This information is included in the sent packet header such that individual nodes participating in *geocasting* makes forwarding decisions based on local distance information. Two key protocol design approaches have been proposed in geographic routing; topology free and topology based protocols.

Topology-free protocols largely employ global-flooding-based forwarding where all nodes in the network receive the transmitted packet, if it is addressed to them they accept it, otherwise they forward to all neighbours and then discard it [14]. Nodes are identified based on their geographic location information [15, 16]. To do so, geographic location information such as latitude, longitude, radius, and direction are included in the packet header's address field. The limitation with this approach is that nodes may constantly change position making it inefficient in time.

Topology-based protocols consider devices to send overhead messaging to establish the route in form of a set of realized network graphs. In order to achieve maximum efficiency, a restricted routing strategy referred to as *greedy forwarding* was proposed with the goal of minimizing flooding by restricting forwarding to a fixed region, adapt the forwarding region based on progress to reduce overhead and apply modalities to deal with gaps so as to guarantee delivery [17, 14]. Sent packets are only forwarded towards the ZOR. Thus, in addition to ZOR, a Zone of Forwarding (ZOF) is also specified. When a node in the ZOF receives a geocast packet for the first time, it only forwards the packet (as opposed to the nodes in the ZOR that also accept the packet).

Fig. 1.1 depicts some the of flooding techniques used in routing. A sender, in green, needs to send a message to the nodes in red, which are located within the ZOR indicated by the green rectangle. Fig. 1.1a adopts a simple global flooding approach that guarantees routing delivery at the expense of bandwidth and energy, a classical protocol free routing approach. Fig. 1.1b shows the Fixed Rectangular Forwarding Zone (FRFZ) approach where only nodes inside the dotted border rectangle do forward the packets. Fig. 1.1c shows the case using Adaptive Rectangular Forwarding Zone (ARFZ) approach. Here, the dotted rectangle is adapted to include only the intermediate node and geocast region. Note that in the two previous cases, the forwarding zone must include at least the target area and a path between the sender and the target area. Fig. 1.1d shows the Progressively Closer Nodes (PCN) approach, where only nodes closer to the geocast region forward the packets. The ZOF on the other hand is demarcated with shaded border lines, all nodes within the ZOF will contribute to forwarding the packet towards the ZOR. Clearly, Figs. 1.1b to 1.1d, use some form of directional forwarding strategy and can be classified as

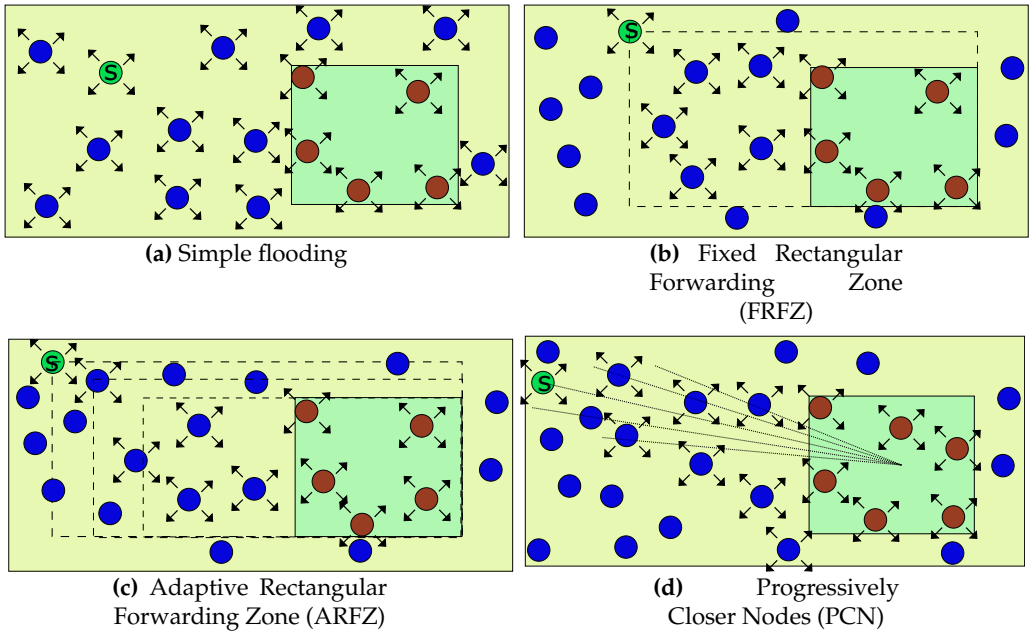

(a) Simple flooding

(b) Fixed Rectangular Forwarding Zone (FRFZ)

(c) Adaptive Rectangular Forwarding Zone (ARFZ)

(d) Progressively Closer Nodes (PCN)

Figure 1.1: Routing techniques

topology-based routing as opposed to Fig. 1.1a, where all nodes in the scheme receive the packets. The latter approaches do contribute to reduction of network traffic congestion during packet transmission [18, 19].

1.1.2 Geocasting in Wireless Communications

This section looks at existing (or proposed) implementation of geocasting in wireless applications. Three research works are particularly discussed which well represent the specificity of geocasting in wireless networks, i.e., the car-to-car and the FleetNet projects, which focus on developing last mile wireless access for Vehicular Ad-hoc Networks (VANET), and the AT & T Labs Geocast System (ALGS) Mobile Ad-hoc Networks (MANET) application. All the three do employ geocasting techniques to broadcast data to predefined locations.

Car-to-X Communications

The CAR-2-CAR Communication Consortium (C2C-CC) project was initiated to develop harmonized VANET standards for the design and implementation of Intelligent Transport Systems (ITS). The harmonized specifications would facilitate interoperability of ITS equipment developed by the various vehicle manufacturers and other roadside units developers. Specifically, it sought to standardise automated data transmission between vehicles, and between vehicles and road side units in an ad-hoc wireless network environment using short range wireless Local Area Network (LAN) technology [20]. *Geocasting* technology was central in the design of the message distribution algorithms used in this project. It motivated the development of the three-way communication schemes used: Vehicle to Vehicle (V2V), surrounding Infrastructure to Vehicle (I2V) and Vehicle to Infrastructure (V2I) communication, collectively referred to as Car-to-X (C2X) communication. The message distribution algorithms formed part of the Geo-Network protocol defined in [21, 22, 23, 24], itself based on Greedy Perimeter Stateless Routing (GPSR) [17]. The Geo-Network protocol defines the operations over wireless multi-hop communication

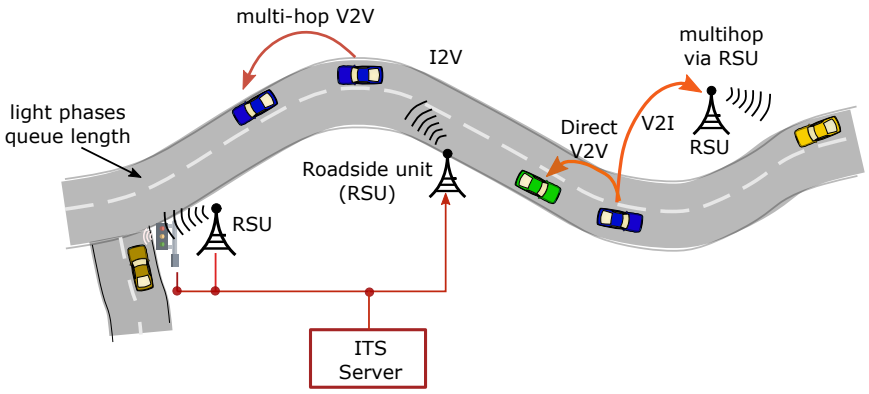

Figure 1.2: Diagram showing typical use cases envisaged in the car-2-car project [20]

and short-range wireless radio (see figure 1.2), including the use of both geographical addressing and geographical routing techniques [25] . The dissemination of data in the network is determined by the exact location of nodes. A node seeking to transmit a packet uses the geo-address in the data packet and its own view of the network topology and position to make an autonomous forwarding decision. Thus, packets are forwarded 'on the fly' and nodes do not need to set up and maintain routing graphs.

Schemes applying geo-network protocol assume that every network node knows its geographical position by Global Positioning System (GPS) or any other positioning systems, and maintains a location table of geographical positions of its immediate neighbouring nodes as soft states [25]. In an ad-hoc network environment, its operation depends on three core services: location service, beaconing service, and forwarding service. Location service identifies the nodes current geographical position, beaconing is responsible for regular broadcasting of the node's geographical location, its direction and speed of travel, and its ID through regular packet broadcasts, and forwarding relays the packet to the next relevant node towards the predefined destination. The forwarding approaches in geo-networking include: geo-unicast, geo-broadcast, geo-anycast, and topologically-scoped broadcast.

Another example of geocasting in car-to-X communications is the FleetNet project, carried out by a consortium of German companies and research institutes with an objective of developing inter-vehicular communication protocols for cooperative driver-assistance systems, local floating car data applications, and Internet communication services [26]. It resulted in the design and development of a software prototype that was installed and test run over a VANET implemented using over-the-shelf 802.11a/b hardware.

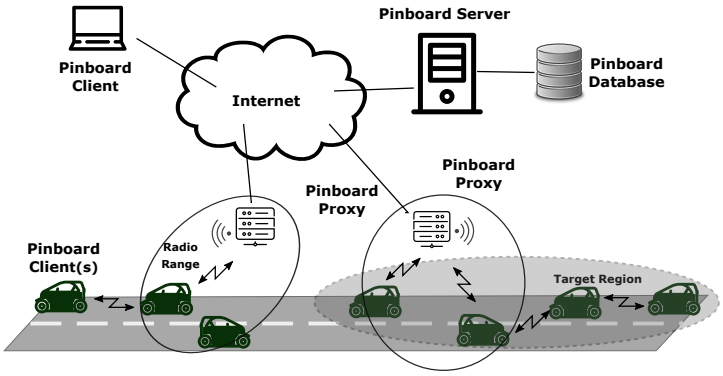

Figure 1.3: FleetNet multi-tier based application

The basic operating principle is that every node (car) has a router that is connected to the application machine via Ethernet IEEE 802.11b protocols and all routing information is stored in the FleetNet routing header. It also employs the beacon-based position-based routing protocol GPSR, with two options for acquiring the destination node address, either extracted from the Reactive Location Service (RLS) [27], or from the incoming header packet. The physical wireless connectivity is implemented by connecting both radio systems to passive external omni-directional antennae mounted on the roof of the car with different antennae for 802.11 a and b [26]. Detailed operations of the scheme, like the position encoding and forwarding, the distance calculation algorithms, and physical position definition and encoding are detailed in [28]. The outcome of the FleetNet project was the Location-Based PinBoard Application (LBPA), whose architecture is illustrated in Fig. 1.3 [29]. A passing vehicle receives periodic broadcasts of messages, and depending on its location in relation to the validity position of the message, it is either displayed or stored and forwarded to neighbouring nodes. [29] further outlines the four core components making up LBPA, i.e., the *PinboardClient*, the *PinboardServer*, the *PinboardProxy*, and the *PinboardDatabase*. Each *pinboard* client must know its current position using GPS and must avail this information to the application for use to compare with the current position and destination position. The destination or target area can be specified in the messages either as a rectangle (GeoRectangle), a circle (GeoCircle) or a point (GeoPoint).

MANET Communications

The ALGS is a multi-tier GA system, i.e., it provides seamless geographic addressing over multi-tier inter-network allowing both long-range and short range low-latency communications among nodes in mutual proximity as illustrated in Fig. 1.4. Packets are permitted to flow across either tier individually, or concurrently, depending on availability of the tiers [30]. The ad-hoc wireless tier uses WiFi devices in ad-hoc mode (802.11 IBSS Mode), the long-range tier uses a cellular data link, i.e., Long Term Evolution (LTE) to connect the nodes to a georouter located in the Internet [31]. To do so, the scheme employs the Centre Distance Priority (CD-P) heuristics for network discovery and learning, and geographical addressing [32, 33]. Recall that in geographic addressing packets are addressed to all devices within a given physical space. In ALGS, this physical space is specified as a circle, defined by the latitude and longitude of its center point, and its radius in meters. The scheme enables an inherent relay capability, i.e., a node that has access to both tiers will automatically provide a link between nodes that may have reach to it but not to either of the other

tiers. The ALGS is provided as a shared platform, as such various geocasting based applications can be run on it. Some of the applications already running on it include: an Internet of Drones application, a map assisted navigation application, and gaming applications as outlined in [31, 34, 35, 36] respectively.

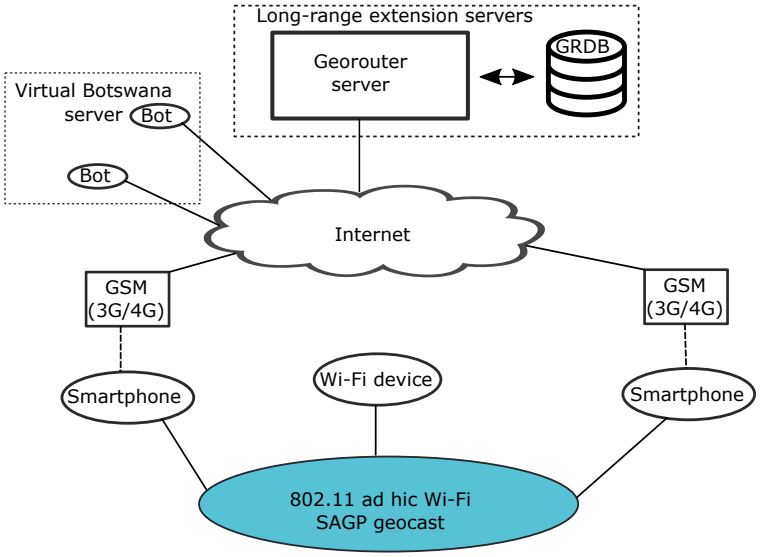

Figure 1.4: ALGS Architecture

1.2 Objectives of the PhD

Geocasting data relies mostly on dedicated routing protocols that operate ensuring a trade-off between network flooding, latency, overhead, packet delivery, location accuracy... Some of the routing approaches lead to privacy issues as the nodes located within the ZOR may require to share their position either with their neighbors or with the infrastructure. By employing global-flooding, topology-free geographical routing protocols may respect end-user privacy at the expense of performance but requires nodes to be able to locate themselves. However, nodes with limited computing capabilities or limited energy, such as encountered in Internet-of-Things (IoT) for instance, may not be able to do so. Furthermore, Global Navigation Satellite System (GNSS)-based positioning suffers anyway from poor accuracy in indoor environments. In this case, other positioning techniques needs to be specifically implemented using an infrastructure with fixed (or at known locations) access points and positioning estimations based on metrics such as Angle-of-Arrival [37, 38, 39, 40, 41] or Time-Difference-of-Arrival [42, 39, 43, 44]. While these approaches may offer solutions for accurate indoor positioning, they are also resource-consuming and are therefore not to be considered with all types of nodes.

To address these identified issues, we investigate in this PhD an alternative geocasting solution at the physical layer. By introducing spatial selectivity in the data broadcasting at the last mile wireless access, we propose a solution for privacy issues while being not too demanding on the node's capabilities and relaxing constraints on routing protocol.

The approach is to add directional capabilities to enable base stations to wirelessly broadcast data to specific locations, thereby performing geocasting. The concept is illustrated in Fig. 1.5a where a directional transmission is achieved by means

of power focusing thanks to an antenna array. The base station can therefore transmits appropriate data to related locations by creating an appropriate number of beams. This scheme suffers however from a fundamental limitation related to classical antenna array theory: the aperture size (i.e., the antenna array size) has to be large in order to create narrow beams, that is, to focus the radiated power within a limited-size area. To overcome this limitation, we introduce the concept of SDF. The idea, illustrated in Fig. 1.5b, is to process the data in order to be decodable only at predetermined locations. We will show in this thesis that this scheme is spatially more selective than focusing the power and therefore overcomes to some extent the limitation due to the inversely proportional relationship between beam and aperture size.

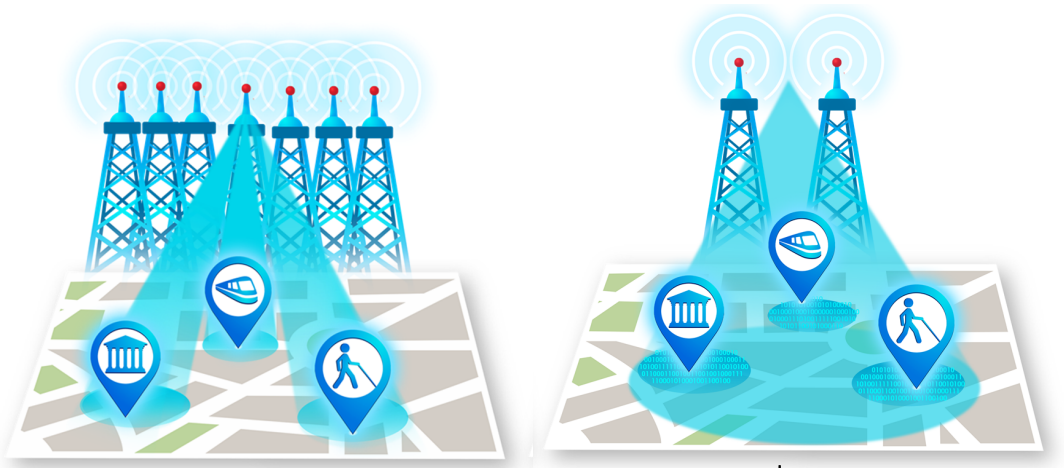

(a) (b)

Figure 1.5: (a) power focusing VS (b) data focusing antenna array schemes

1.3 Thesis outline

This thesis is organised as follows.

Chapter 2 reviews the different techniques that enable directional capabilities in base stations. The focus is on techniques that employ antenna arrays since they offer a flexible mean to generate beams in any directions. As such, this chapter first introduces the necessary background on antenna array theory to illustrate the fundamental limitation of power focusing. It then reviews the state of art of two main spatial focusing techniques that exploit multiple antenna systems to achieve directional properties, i.e., beamforming and DM. The single antenna compatible technique, TR is also discussed. Finally the main limitations of the power focusing approaches is summarized in the conclusion.

Chapter 3 introduces the proposed direct sequence spread spectrum-based SDF technique outlining the general framework of the SDF system. It then reviews the concepts of orthogonal signalling which is the technique at the core of SDF. Specifically the different approaches to orthogonal signalling are reviewed, and with the aid of analytical expressions, the benefits accrued when orthogonal signals are privileged over non-coded ones are described. The chapter then delves into concept of

spread spectrum modulation, covering aspects of pseudo-random codes classification and generation, with a focus on orthogonal codes and the underlying correlation properties. This leads to the discussion on the principles of DSSS-SDF. The DSSS-SDF transceiver architecture, choice of spreading codes, and operation over LOS channel models are discussed. Analytical derivations are implemented to give physical insights regarding the operation principle as well as to validate numerical simulations used for the performance analysis. Finally, a concept that introduces quadrature components to DSSS-SDF is discussed. IQ resources provide an additional degree of freedom to the DSSS-SDF scheme, further enhancing the performance by enabling SDF-dedicated channel estimation and equalization. For all the cases covered above multiple simulations are carried out, first, in order to identify the mechanisms behind the angular directional properties and second, to study the robustness of the scheme, compared to classical power focusing techniques.

Chapter 4 looks at the robustness of the scheme in multipath environments. To do so, first the general multipath resolution and mitigation abilities of typical direct sequence spread spectrum communication systems are discussed. Subsequently a numerical analysis of the proposed DSSS-SDF-IQ scheme is implemented over a general multipath environment to give insights into how the scheme behaves in such an environment. We then discuss the general characterization of wireless channels using ray tracing techniques, here the focus is on the radio channel parameters that describe the channel response, the idea is to have insights into how the channel may impact the SDF signal propagating through it. The channel models of interest in this work are the 2-ray ground-reflected channel, 4-ray urban canyon, and 6-ray urban canyon. We also investigate the influence of space-time geometrical channel models on SDF, with a specific focus on the GBSBM. For all the cases mentioned above, the respective channels are modelled, simulations are carried out and conclusions drawn based on the acquired results.

Finally, a general conclusion is drawn at the end of this manuscript and perspectives to this PhD are given as research directions for future works.

Chapter 2

Spatial Focusing approaches: State of the art

To add directional capabilities to base stations in order to perform geocasting at the physical layer, different techniques can be considered. Most of them considers the ability for the transmitter to focus its radiated power toward the region of interest (i.e., the ZOR). This is typically done by leveraging the spatial degrees of freedom offered by multiple antenna systems using an appropriate precoding. Other precoding techniques such as Time Reversal (TR) can also achieve power focusing to some extent using a single antenna as a transmitter.

This chapter reviews the different techniques that can give directional capabilities to base stations. Since many of them use antenna arrays, we first introduce the necessary background on antenna array theory to illustrate the fundamental limitation of power focusing. Then a state-of-the-art of two main approaches to exploit multiple antenna system to achieve directional properties is drawn. In particular beamforming and Directional Modulation (DM) techniques are detailed. The single-antenna-compatible technique, namely TR, is also discussed. Finally, the main limitations of such approaches are summarized.

2.1 Antenna Array Theory

In multiple antenna systems, a fixed number of antenna elements are arranged along a given lattice (usually 1D-linear or 2D-rectangular) thereby forming an array. The signals radiated from the individual elements add up together in the channel and if they are identical and coherent, create an interference pattern known as the array radiation pattern. An example of such array is presented in Fig. 2.1.

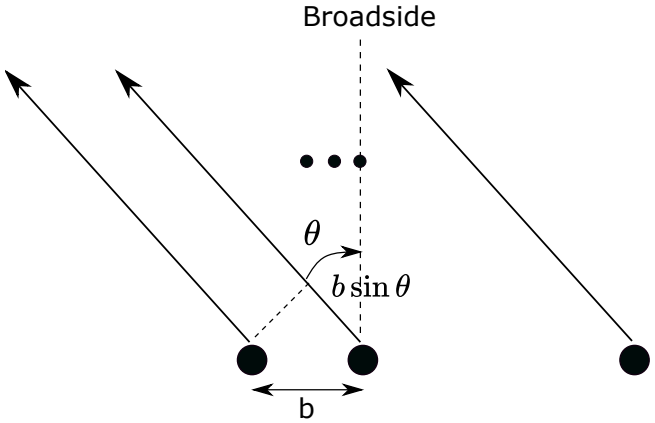

Figure 2.1: linear array

b is the inter-element spacing, which is typically equal to $\frac{\lambda}{2}$, where λ is the free-space wavelength at the carrier frequency. Under paraxial approximation, the phase difference between two waves radiated by adjacent elements toward a given direction angle θ is $\psi = kb\sin(\theta) + \alpha$ where $k = \frac{2\pi}{\lambda}$ is the free-space wavenumber and α is is the phase difference between signals at the antenna input ports. Assuming all array elements are fed by the same narrowband signal, the waves radiated by each element experience constructive and destructive interference that lead to the well-known Array Factor (AF) given by [45]:

$$AF(\theta) = \frac{\sin\left(\frac{N}{2}\psi(\theta)\right)}{\sin\left(\frac{\psi(\theta)}{2}\right)} \tag{2.1}$$

where N is the number of antennas in the array and is also the maximum value of the AF function.

Furthermore, assuming antenna elements to exhibit the same radiation pattern, the array gain is determined by the multiplication of the gain due to individual elements with the AF:

$$G_{\text{array}}(\theta) = G_{\text{element}}(\theta) \times AF(\theta) \tag{2.2}$$

Operating with an antenna array enables achieving a gain of $NG_{\text{element}}(\theta_0)$ in the direction of interest θ_0, e.g., the ZOR. The AF maximum gain is obtained when $\psi(\theta_0) = 0$. The direction for which this condition is true can be adjusted by acting on the variable α, that is by phase shifting the input signals at each antenna element in a narrowband scenario. The normalized AF as a function of θ for different array sizes is illustrated in Fig. 2.2 for $b = \frac{\lambda}{2}$ and $\alpha = 0$.

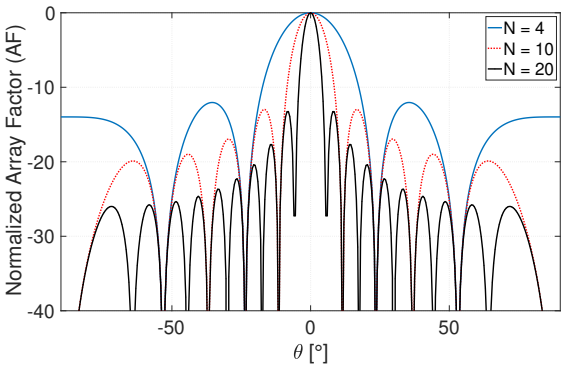

Figure 2.2: Normalized array factor for different number of antenna elements N

The potential of angular selectivity for goecasting appears clearly: the radiated power depends on the angle θ and the antenna array can therefore radiates power toward the ZOR direction only. Consequently, only an angular region is addressed by such array, which is the goal we are seeking in geocasting. Increasing the number of antenna elements in the array enables to target smaller angular size ZOR. Furthermore, by controlling the phase shift α, the ZOR direction can be chosen and modified. Finally, as seen in the next section, if one use digital or hybrid digital-analog beamformers (i.e., array feeding structure), a single base station can address multiple ZOR, each of them receiving its own unique content.

The size of the beam radiated by the array is typically characterized by the Half Power Beamwidth (HPBW) metric. The half-power angles can be calculated by the

following approximation [45]:

$$\theta_{3dB}^{\pm} \approx cos^{-1}\left[\frac{\lambda}{2\pi b}\left(-\alpha \pm \frac{2.782}{N}\right)\right] \tag{2.3}$$

and the HPBW of the array can therefore be obtained by:

$$\Delta\theta = \theta_{3dB}^{+} - \theta_{3dB}^{-} \tag{2.4}$$

Using (2.3) and (2.4), the influence of the number of antennas N on the HPBW can be observed as shown in Fig. 2.3. Naturally, the larger N, the narrower the beam. It is also observed that for tilting angles away from broadside, the HPBW, thereby the angular accuracy, decreases.

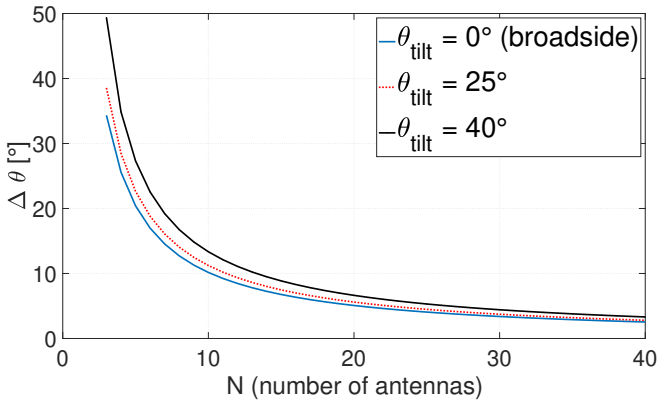

Figure 2.3: 3dB-beamwidth of the array factor for different number of antenna elements N and different tilt angles

The inversely proportional dependence between N and the HPBW highlights the fundamental limitation of power focusing with antenna arrays to perform geocasting. To target an accurate area in a geocasting process, i.e., a small-size ZOR, the radiated beam needs to be narrow, which in turn implies a large number of antenna elements. With a typical distance between elements of a half-wavelength, the array size may become very large. As an example, for a base station to illuminate a 10-meter area located 200 meters away, a beam of 2.9° is required. To achieve this order of magnitude, a classical antenna array would need an aperture of 18λ, which represents about 6 meters at 900 MHz. Overcoming this limitation where the radiating system needs to be very large to preform geocasting in a small angular region is one of this thesis objective.

2.2 Beamforming

Beamforming is a signal processing technique used in sensor arrays for directional signal transmission or reception. Directivity is achieved by combining array elements such that signals at given angles experience constructive interference while others experience destructive interference. Due to the principle of reciprocity, beamforming can be employed at both the transmitting and receiving ends in order to achieve spatial selectivity. Compared to omni-directional antennas, the reception or transmission directivity attained is also referred to as receive/transmit gain (or loss). A key take away in the definition given above is the role of interference in enabling

the direction/reception of energy to/from a desired direction. Given the fact that wireless communication systems are characterized by limited transmit power, it is evident that beamforming, i.e., pointing the transmit energy toward an actual receiver, or listening carefully in the direction of a transmitter as to reject noise coming from other directions, is a useful system property.

2.2.1 Linear array

Let us consider a base station using an antenna array communicating with a single antenna user such as show in Fig. 2.4, where $\mathbf{h} = (h_{11}, h_{12}, ...h_{1N})^T$ is the propagation channel. Beamforming processing consists in finding the precoding (at TX) or decoding (at RX) vector $\mathbf{w}$ than maximizes a certain metric, such as the SNR. For instance, in matched beamforming algorithm at TX or, conversely, Maximum Ratio Combining (MRC) at RX, the weighting vector $\mathbf{w}$ is simply the conjugate of the channel, i.e., $\mathbf{w} = \mathbf{h}^*$.

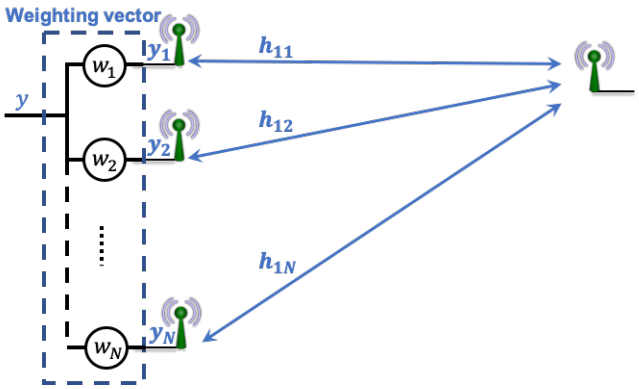

Figure 2.4: Beamforming

To illustrate how such processing operates, a LOS scenario is firstly assumed, where a single plane wave impinges on a uniformly spaced linear array (ULA) as shown in Fig. 2.5. The wave-front experiences slightly different path lengths corresponding to the positions of the various elements, and consequently different phase shifts. Under paraxial approximation (i.e., far-field), the path length difference between two successive elements is given by $l = b\sin(\theta)$, where b and θ are respectively the inter-element spacing and angle of arrival (AoA) relative to the broadside. The corresponding phase shifts across consecutive elements is given by $\phi = 2\pi l/\lambda = 2\pi b\sin(\theta)/\lambda$, where λ represents the wavelength. This result can also be presented in terms of the delay differences of the consecutive elements as $\tau = l/c$, where c is the speed of propagation of light. From Fig. 2.5, and making narrowband assumptions ($W \ll f_c$, where W is the bandwidth of the signal and f_c is the carrier frequency), the impinging signals can be expressed as $u_p^k(t) = \mathrm{Re}(u(t+\tau)e^{jk\phi}e^{j2\pi f_c t})$ where $u(t)$ is the complex envelope of the incoming signal, assumed to be of bandwidth W and $k = 0,\ 1,\ ...,\ N-1$, is the antenna index. The time shift τ has two effects on the complex envelope: a time shift of the baseband waveform u, and a phase rotation ϕ due to the carrier. In narrowband scenarios, the time shift of the baseband waveform envelope is negligible [46][47].

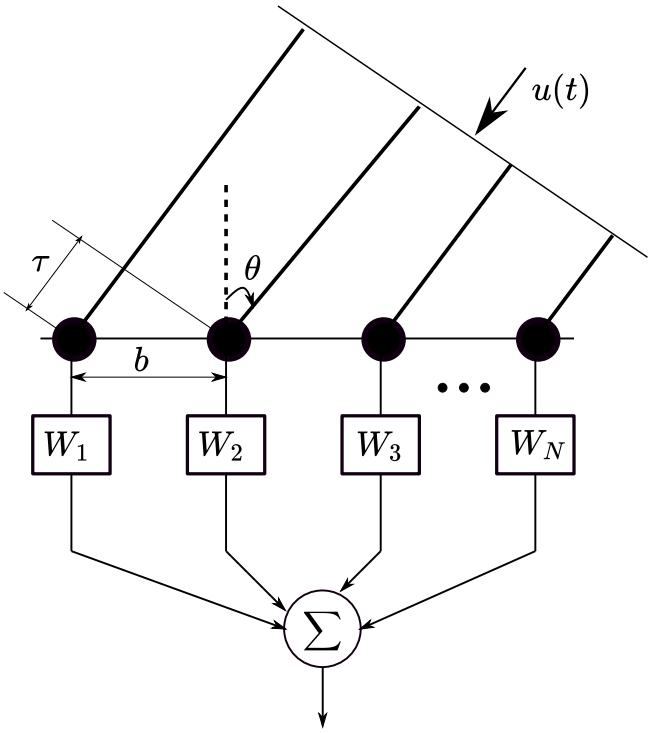

Figure 2.5: Beamformer under paraxial approximation

Consequently, we can define the array response vector **a** for a particular Angle of Arrival (AoA) as:

$$\mathbf{a} = (1, e^{j\phi}, e^{j2\phi}, ..., e^{j(N-1)\phi})^T \tag{2.5}$$

The array response vector $\mathbf{a}(\theta)$ can be made explicitly dependent on the AoA θ in the case of ULA thanks to the $\phi(\theta) = 2\pi b \sin\theta/\lambda$ relationship. The linear spatial phase increase (across elements) corresponds to the linear phase increase across time for a sine signal. $\phi(\theta)$ is therefore referred to as the spatial frequency corresponding to AoA θ and the set of array responses $\mathbf{a}(\theta), \theta \in [-\pi, \pi]$ with varying AoA is termed the array manifold.

The knowledge of the array response for a given AoA, enables us to maximize the received power or the transmitted power for respective receive or transmit antenna array in that direction using a spatial matched filter or spatial correlator. If the first antenna element receives a complex baseband waveform (after down conversion and sampling) $s[n]$ from AoA θ, then in vector notation we can write

$$y[n] = \mathbf{a}(\theta)s[n] + w[n] \tag{2.6}$$

where $y[n] = (y_1[n], ..., y_N[n])^T$, $w[n] = (w_1[n], ..., w_N[n])^T$, and $\mathbf{a}(\theta)$ is the array response corresponding θ. Ideally we want to maximize SNR, to do so, the spatial processing will correlate against the noiseless template $\mathbf{a}(\theta)$. In essence, we wish to compute the decision statistics

$$Z[n] = \langle \mathbf{y}[n], \mathbf{a}(\theta) \rangle = \mathbf{a}^H(\theta)\mathbf{y}[n] \tag{2.7}$$

The above correlation between the spatial signal and the array response represents the actual beamforming process. The desired signals contribution $Z[n]$ is $||\mathbf{a}(\theta)||^2 s[n] = Ns[n]$. In this case the signal amplitude and signal power are respectively scaled by factors N and N^2 and the variance of the noise contribution to the decision statistic

is amplified by a factor of N. As such, the SNR is also amplified by a factor of N considering receive beamforming resulting in a beamforming gain [48].

Receive beamforming gathers energy coming from a given direction. Transmit beamforming on the other hand directs energy in a given direction. To do so, given a linear transmit antenna array, sending the time domain samples $s[n]$ involves sending spatial vector $s[n]\mathbf{a}^H(\theta)$. Given that the spatial channel to the receiver is $\mathbf{a}(\theta)$, the signal received is given by $s[n]\mathbf{a}^H(\theta)\mathbf{a}(\theta) = Ns[n]$. Evidently, the received amplitude scales as N, and the received power as N^2. The noise at the receiver is not impacted by transmit beamforming gain, as such, a N antenna transmit beamforming results in a N^2 SNR gain compared to a single antenna system. However, for fair comparison, if the total power radiated by the array is fixed, that is if the power of the signal to be transmitted is split over the N antennas of the array, the actual array gain leads to an SNR improvement by an N factor .

In a LOS scenario and under far-field consideration, beamforming performance can be well predicted by the antenna array theory as detailed in the previous section, and is therefore facing the same limitation regarding the inversely proportional relationship between the aperture size and the beamwidth.

2.2.2 Beamforming System Architectures

Beamforming architectures are classified into three categories: analog beamforming, digital beamforming, and hybrid beamforming architectures.

Analog beamforming

This architecture is also known as phased arrays in the field of radar and antennas. It uses attenuators and phase shifters as part of the analog RF circuit where a single data stream is divided into separate paths. The advantage of this method is that it only requires a single digital and RF chain. The disadvantage is that a single data stream can be transmitted at a time with a given weighting vector. Fig. 2.6 illustrates a basic architecture of an analog beamforming transmitter, it is made up of a single RF chain and several phase shifters feeding an antenna array.

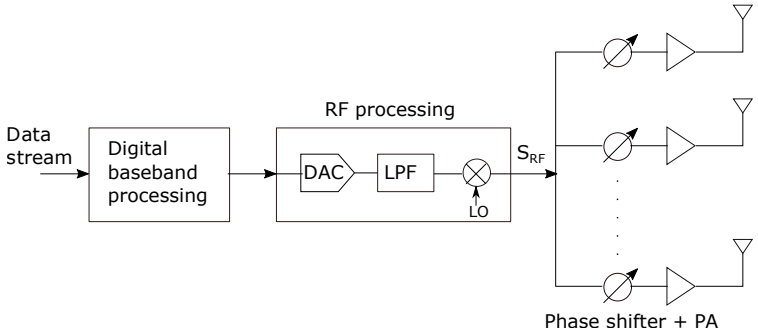

Figure 2.6: Analog beamforming architecture [49]

Analog beamforming can be carried out at either the RF or intermediate frequency level [50]. The weighting vector $\mathbf{w}$ is achieved by varying the amplitude and phase of the signals being fed into the antenna array elements.

Digital Beamforming

Digital beamforming usually use as many RF chains as the number of antenna elements present. Beamforming is performed in the baseband where the amplitude and

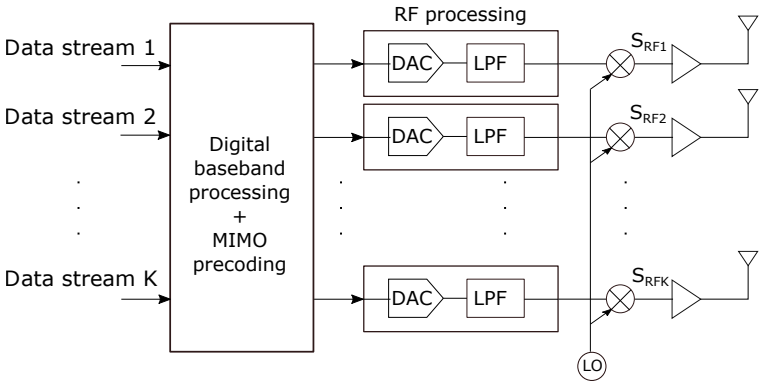

Figure 2.7: Digital beam-forming architecture [51]

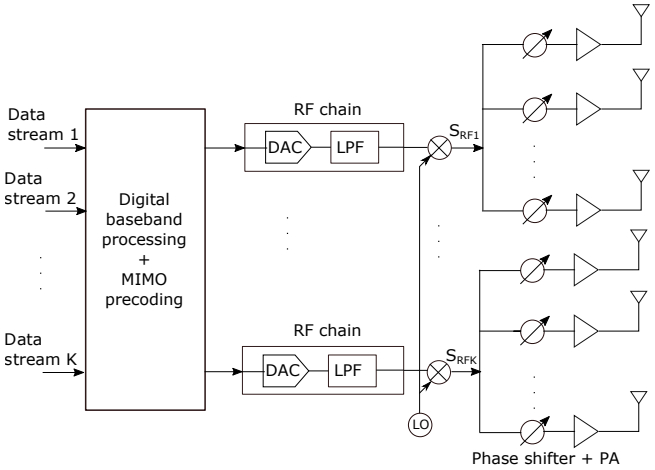

Figure 2.8: Hybrid beamforming architecture [51]

phase weighting are applied. This is typically the preferred approach at sub 6 GHz frequencies as the the RF chain components are comparatively inexpensive and it offers greater flexibility for the signal processing. Fig. 2.7 illustrates the high-level digital beamforming transmitter architecture with multiple RF chains [49]. Using this architecture, a large number of data streams can be sent with unique weighting vectors, depending on the number of antennas and the propagation channel. This enables addressing multiple users or location with different data sharing the same resources, i.e., Spatial Division Multiplexing (SDM) and/or increasing the data rate of a communication by multiplexing the data to be transmitted over several orthogonal channels, i.e., Spatial Multiplexing (SM), if the user is also equipped with multiple antennas. Digital beamforming can also benefit from the array gain if the N RF chains are coherent.

Hybrid Beamforming

Hybrid beamforming is a trade-off between digital and analog beamforming architectures. Similar to digital approaches, this allows for flexibility in the processing (with the possibility to address multiple users and/or do SM) while reducing the overall cost and power consumption of the array thanks to the use of analog beamformers [52]. The idea is to have less digital and RF chains than the number of antenna elements. It is characterized by separate analog beamforming unit connected to a sub-set of antennas for each data stream. This approach is preferred

in the millimeter-wave domain where the number of antenna elements in the array is very large and the hardware power consumption too. Analog beamforming unit losses due to phase shifters can be mitigated by replacing the adaptive phase shifters with a selective beamformer such as a Butler matrix. Fig. 2.8 shows a typical hybrid beamforming transmitter architecture. The pre-coding is divided between the analog and digital domains. In this example, $K << N$ data streams can benefit from a unique weighting vector $\mathbf{w}$. Signals at the output of each RF chain are sent over a sub-array and can experience an array gain of N/K. The number K of data streams is equal or less than the number of RF chains, depending on the considered precoding algorithm.

2.2.3 Beamforming in Geocasting

In the literature, beamforming has been considered in geocasting applications in the area of vehicular communication, a typical case is in the car-to-X project mentioned in chapter 1. The introduction of beamforming enhanced the application of geocasting both in the cases of multi-hop implementation, i.e., when vehicles need to forward messages to other vehicles, and in the Infrastructure to vehicle communication (I2V), i.e., when road side units (RSU) need to communicate to vehicles. For simplicity and in line with our work, the following discussion will only consider the typical I2V implementation where the RSU sends information to the vehicle nodes.

It was observed in the car-to-X project that using quasi-omnidirectional antennas made the geocasting scheme vulnerable to interference and lead to loss of power with respect to the position of the targeted receiver. To mitigate against the above, multiple schemes [53, 54, 55], were initially proposed to attain directivity. In [56], C2X beamforming is proposed to secure the communication, enable user privacy, and congestion control, all carried out at the physical layer. To do so, the scheme employed radiation pattern control mechanisms that allowed nodes to focus transmitted power in a desired direction through adaptive beamforming, this enabled the base stations to improve both signal reception and rejection of unwanted signals [57]. The approach ensures that the data being exchanged is guarded and the medium on which an attacker can operate is restricted [58]. To do so, a unique X-Y (two crossed) antenna structure capable of carrying out both broadside and endfire transmission was designed to comply with the minimum antenna requirements for the C2X communication defined in [59].

At minimum, the requirements set that transmitted packets at any instant had a geographical validity as a function of receiver position with respect to the base station. The assumption here being that directing the radiation pattern based on its geographical validity limits the reach of an attacker by excluding its position from the transmission path. It was also a requirement that in cases of Denial-of-Service attack, where it is an attacker that is transmitting, the antenna system had to implement null steering in the direction of the attacker/jammer, again the assumption was that in most cases the attacking system will be located on the road side. The design flow and algorithms used to implement phasing, element biasing, or transmission power was determined based on given scenarios, like attacker position and message type, at any given instant as described in [58].

Antenna Model Specification

The linear secure C2X beamforming two-crossed antenna array with variable antenna number, distance, and adjustable phasing is shown in Fig. 2.9, [57, 60, 61].

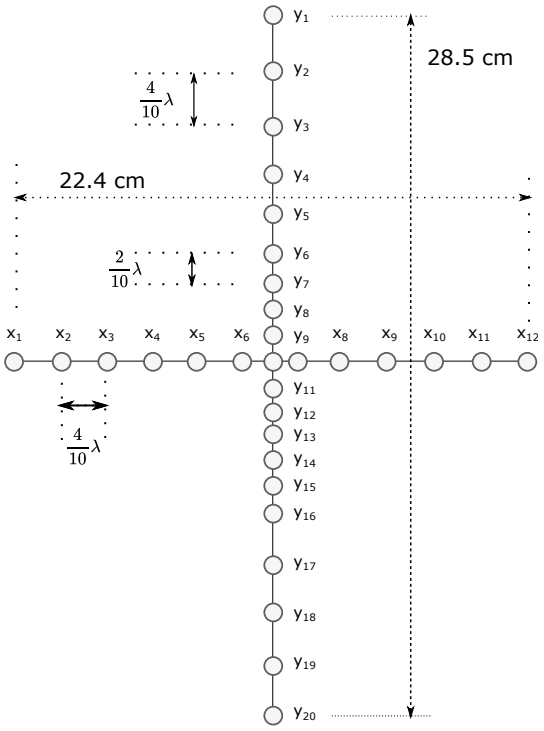

Figure 2.9: Two crossed antenna arrays [58]

It consists of two orthogonal antenna arrays which are steered independently from each other so as to attain a wide variety of distinct transmission patterns. This model ensured the C2X communication requirement of high flexibility in the direction of the main beam towards the targeted nodes, at the same time keeping the undesired side lobes to a bare minimum.

This model allowed for the unique manipulation on each array (X-Y) of: array type, number of elements of each array (N_x, N_y), element separation in each array (dx, dy), phase shift in each array (α_x, α_y), and transmission power (P_x, p_y). The antenna parameters identified above are set based on the scenario properties given the outlined communication situation, the actual state of the traffic including geographical positions of all the nodes within the specified communication range $600 - 1000$m, and the actual road characteristic such as bends and road widths. Details about the manipulation of these properties and element configurations to achieve secure transmission and reception in this system are fleshed in [58]. To satisfy all the proposed use cases, the antenna architecture as depicted in Fig. 2.9 was equipped with a total 12 and 20 antennas in the X and Y arrays respectively. The 20 antennas in the Y-array are never all used at the same time under any given use case, the number 20 was set to cater for the different inter-element distances required for different use cases. For the RSU case under our study, only antenna elements X_2 to X_{10} are active. This is sufficient for set functionalities that include: Green Light Optimal Speed Advisory; Remote Diagnostics; Drive-through Payment; and Vehicle Computer Program Updates. In all the use cases, the beam depends on the receiver position.

Fig. 2.10 illustrates a typical RSU based use case. Probe Vehicle Data is sent every time the vehicle passes a RSU. Three scenarios are observed: To the left, vehicle approaching, $(\alpha = 0 \rightarrow \alpha = 140)$; Middle case, vehicle facing RSU, $(\alpha = 140)$; and to the right, vehicle moving away from RSU, $(\alpha = 140 \rightarrow \alpha = 0)$, in this case α denoted the phase shift [62]. Steering the beam based on the effective driving behavior of the vehicle is achieved by calculating the relative angle between both nodes, this

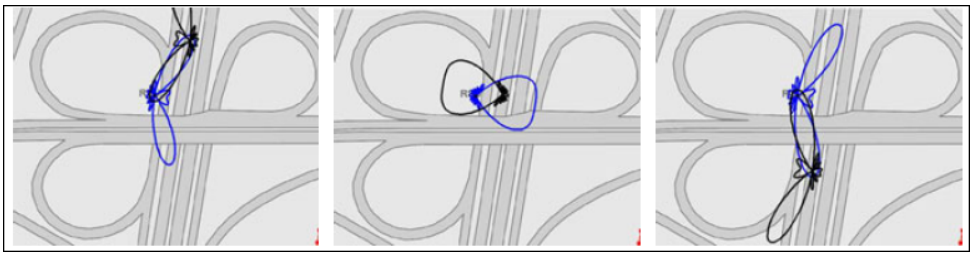

Figure 2.10: Mutual position-based beamforming for RSU communication [62]

value is then transferred to an electrical phase shift of the feeding signal. Attained beamforming enhances directivity and also impedes potential eavesdropping.

Beamforming Algorithm: Secure Transmission

In C2X beamforming, selection and steering of the beams is carried out at the lower system abstraction layers of the architecture. This section briefly describes a typical beamforming algorithm whenever a Decentralized Environment Notification Message (DENM) is to be transmitted. The DENM is initially passed from the application layer for subsequent transmission. This messages header is analyzed by a beamforming component of the MAC layer, so as to determine the communication scenario linked to it. Assuming the originator field determines that the message is for broadcasting, antenna elements x_6 and x_7 will be biased for a near omnidirectional pattern, here suggesting that the message is to be received by all nodes around the transmitting node. In a scenario where it is only required to forward the given message, then an endfire pattern is created. To do so, specific elements of the Y-antenna array are biased with the appropriate electronic phase shift (here 207°). Simultaneously, the power level of the feeding signal can be varied based on the required communication range. There is no rule of thumb as to the relationship of power in dB with possible range, say in meters, as this scheme is expected to operate in diverse environments which always experience different channels.

Specific to C2X beamforming, probe Vehicle Data is sent every time the vehicle passes a RSU. In that case, the position-dependent pattern to produce quite narrow beams towards the receiver node. Assuming non stationary vehicles, the process of steering the beam relative to the dynamic positions of the vehicle and related geometric positioning between the two nodes is calculated and transferred to an electrical phase shift of the feeding signal. Indeed Mutual beamforming between nodes results in significantly improved directivity, at the same time isolating potential eavesdropping of the exchanged messages.

2.2.4 Conclusion on beamforming

Using beamforming to illuminate a ZOR appears to be an efficient way to perform geocasting at the physical layer even though the angular accuracy might be limited if the array size is not large enough. However, ensuring geocasting only by means of power focusing, such as achieved by beamforming, might suffers from limited reliability. Indeed, a user within a ZOR is able to retrieve the data only if the SNR is sufficiently large, with respect to a given communication scheme. However, the SNR does not depend only on the radiated power density imposed by the array pattern and the channel, but also on the user hardware. For instance, the SNR depends

on the gain of the Low Noise Amplifier (LNA) that the user benefits from. Consequently, depending on the performance of the user hardware, the area within which the SNR is sufficiently large to retrieve the data may change. Intuitively, the larger the LNA gain, the larger the ZOR. Having a ZOR whose area has a stringent dependency on the received SNR, thereby on the user receiver, is not very convenient. An alternative approach to performing only power focusing is to precode the data at a symbol level and to introduce intended interference to the data outside the ZOR. This will prevent any possibilities to retrieve the data outside the ZOR, even if the SNR is still large. This goal is shared by physical layer security techniques and can be achieved thanks to directional modulations as detailed in the next section.

2.3 Directional Modulation

A critical consideration in the design of modern communication techniques is security, more so for wireless communication that by nature do broadcast/transmit information through space, as such, the transmitted data lack physical boundary compared to that provided by wired communication. This makes wirelessly transmitted data susceptible to interception. As security is key in all communication, be it wired or wireless, the traditional approach to enforcing it is by employing cryptography [63]. However, cryptography is not a cure all in security, this is evident from the fact that with increased computational resources encryption algorithms get compromised.

One way to mitigate against such possible compromises is to implement security at the very basic point level of communication, i.e., at the physical layer [64]. To do so encryption has to be implemented at the physical layer, this can be achieved by generation of keys at the physical layer by exploiting the randomness at the physical layer, e.g., electromagnetic propagation in a reciprocal multipath environment, instead of using mathematical means [65]. Indeed, to do this, one must probe for the channel state information, and based on this information, perform signal preprocessing. This approach is dependent on the properties of the given wireless channel like multipath and temporal variations, making it unsuitable for channel invariant communication environment.

An alternative and less complex, i.e., keyless, approach that can be used in any wireless channel scenarios is directional modulation [66, 67]. DM is a key-less security technique for securing wireless communications at the physical layer. To do so, the DM transmitter employs beamforming for directing digitally modulated data signals towards a secure pre-defined spatial direction, preserving the constellation pattern in this direction while simultaneously distorting the constellation patterns of the same signals along all the unsecured communication paths. This is typically done by projecting artificial noise (AN) in these unwanted directions [68]. Fig. 2.11 illustrates typical constellation patterns for a DM system using quadrature phase-shift keying (QPSK). It is observed that the constellation format is preserved in the direction θ_o, i.e., towards the legitimate receiver, and scrambled in all other directions, i.e., towards eavesdroppers. To better understand the DM scheme, we consider the operation in a LOS environment of a conventional transmit array assuming that all the antenna elements are actively excited. In this case, information data is normally digitally modulated at baseband, precoded, up-converted, and finally radiated by the antenna elements. Given a linear beamformer that is made adaptive at the channel fading rate, its complex gain G_n for each antenna n can be regarded as a constant with respect to the modulation rate which in most cases is much faster than

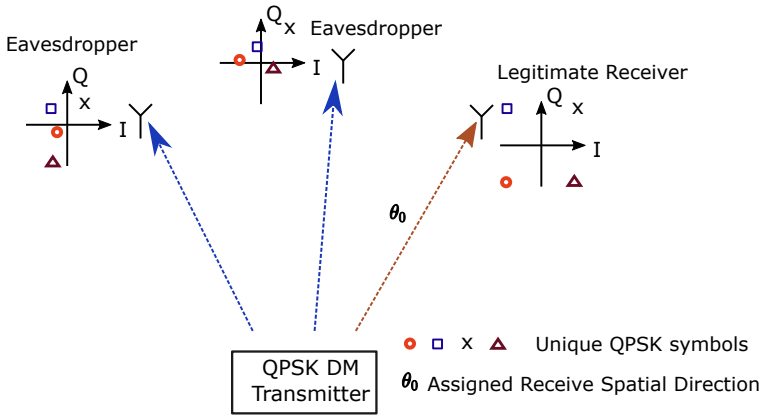

Figure 2.11: Illustration of the properties of a QPSK DM system. [69]

the channel fading rate. In such a case, the far-field electric field E_m is just a scaled version of $\mathbf{D}_m$, the mth symbol of the modulated data, in all directions (2.8) and thus the modulation format (constellation patterns) in IQ space is preserved in all spatial directions [70]. Such radiated field, under narrowband scenario can be expressed as:

$$\mathbf{E}_m(\theta) = \sum_{n=1}^{N} \mathbf{D}_m \cdot \mathbf{G}_n^* \cdot e^{j\pi\left(n-\frac{N+1}{2}\right)\cos\theta} = \mathbf{D}_m \sum_{n=1}^{N} \cdot \mathbf{G}_n^* \cdot e^{j\pi\left(n-\frac{N+1}{2}\right)\cos\theta} \tag{2.8}$$

where $(\cdot)^*$ denotes complex conjugation, and the inter-element spacing is $\lambda/2$. Evidently, the output $\mathbf{E}_m(\theta)$ is dependent on the transmitted symbol $\mathbf{D}_m$.

For DM systems, the direction-dependent signal format transmission is enabled by varying $\mathbf{G}_m$ in (2.8) at the modulation rate during data transmission, i.e., symbol-level precoding. This introduces an additional degree of freedom as shown in (2.9). The updated $\mathbf{G}_m$ is denoted as $\mathbf{G}_{mn}$ which together with $\mathbf{D}_m$ are updated at the symbol rate in a DM scheme. An optimization can be then conducted to find the appropriate weights $\mathbf{G}_{mn}$ to transmit the symbols toward a desired direction θ_0 without distortion and benefiting from some array gain while scrambling the constellation in other directions.

$$\mathbf{E}_m(\theta) = \sum_{n=1}^{N} (\mathbf{D}_m \cdot \mathbf{G}_{mn}^*) \cdot e^{j\pi\left(n-\frac{N+1}{2}\right)\cos\theta} \tag{2.9}$$

$(\mathbf{D}_m \cdot \mathbf{G}_{mn}^*)^*$ can be considered as the complex gain G'_{mn} of a baseband information data controlled beamforming network. This approach to DM can be visualized as the RF carrier f_c being fed into beamforming network as shown in Fig. 2.12. It is the analog DM scheme that forms the basis of multiple DM structures including [71, 72, 73, 74, 75, 76, 66, 67, 77, 78, 79].

As indicated above most analog DM techniques employ the generic phase shifter architecture discussed, however in [80], a different approach is taken. It proposes a dual-beam directional modulation (DM) technique for physical-layer secure communication. This approach exploits the in-phase and quadrature (IQ) baseband signals to excite two different antennas in contrast to classical transmitter where they are used to excite the same antenna.

As such the constellation points of the transmit signal preserve their positions as in classical digital modulation signal in the pre-defined directions, however, towards the unwanted directions their phases are scrambled given that the transmit signal is

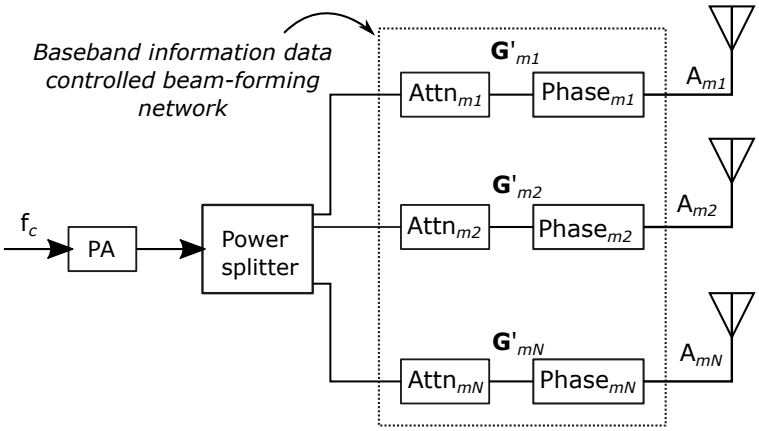

Figure 2.12: Generic analog active DM transmitter architecture [69].

modulated in a dual manner at the baseband and the antenna level. Fig. 2.13 illustrates this approach. It shows the principle of dual-beam DM technique, where the

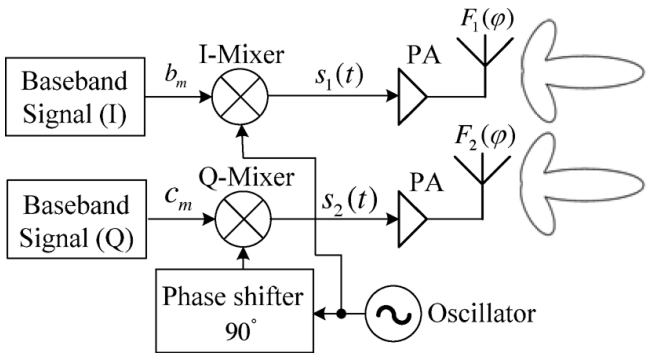

Figure 2.13: Block diagram of the dual-beam DM signal transmitter. [80]

signals $S_1(t) = b_m \sin \omega t$ and $S_2(t) = c_m \cos \omega t$ feed two distinct antenna elements, thus driving two unique beams, $F_1(\varphi)$ and $F_2(\varphi)$ respectively. $b_m \in \{-1\ 1\}$ and $c_m \in \{-1\ 1\}$ represent the I and Q data information, ω is the angular frequency and φ denotes the receiver angle [80]. Unlike other DM approaches that employ phase shifters, this approach manipulates the radiation pattern for physical-layer secure communication, to do so, only needs to design two transmit beams, which utilizes the orthogonal property of IQ baseband modulation signal, as such it avoids the design of complex transmitters to effect scattering properties of classical DM schemes. The orthogonality between I and Q components is preserved only toward the direction of the legitimate user, preventing any eavesdropper outside that direction to retrieve the data. This DM technique, unlike most others, does not benefit from the array gain as the signals transmitted by the two antenna are not correlated.

DM can also be implemented in the digital domain as proposed in [68, 81, 82]. It was shown in Fig. 2.11 that DM transmitter sends its information to the desired user such that eavesdroppers cannot correctly decode it. This indeed is achieved by exploiting the directivity characteristic of antenna arrays together with beamforming, and finally a projection of artificial noise (AN). In essence, the DM transmitter transmits the confidential message to the desired direction and interferes with the eavesdroppers by projecting artificial noise in the unwanted directions to secure information in the wanted region. To increase the efficiency of the scheme described

above, a smart transceiver is proposed in [82], it is shown in Fig. 2.14. The novelty of this approach lies in the introduction of machine learning to DM techniques, this enables to implement precise estimation of the Direction of Arrival (DOA) that is subsequently used to design the pre-coding vector and the injected artificial noise (i.e., random signal) that lies in the null-space of the intended user. So this artificial noise does not distort the data at the intended location but everywhere else.

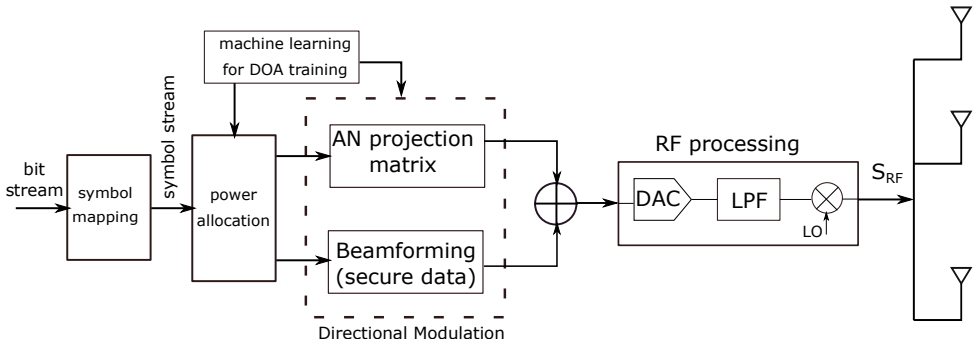

Figure 2.14: Schematic of a smart DM transmitter [82]

The machine learning algorithm employed in this case is the Bayesian learning (BL) based approach that enables the enhancement of the DOA measurement precision at the DM transmitter using a completely digital structure. The way it works is that the structure initially operates as a receiver, collecting a number of snapshots of the channel state information which are then applied to the Root-MUSIC method to obtain the training data set.

High-resolution DOA measurement and the attendant high-precise DOA error density estimation are critical for DM directivity implementation in this case. In [83, 84], it is outlined that efficient DOA measurement leads to performance improvement given that expected information and AN can be accurately transmitted to the desired direction and eavesdropping direction, respectively.

One critical aspect of DM is power allocation as discussed in [85] where it is proposed a power allocation strategy for maximizing secrecy rate of DM based on the given beamforming vector of the information to be transmitted, AN projection matrix, and total power constraint. To do so, they used the Lagrange multiplier method to derive the analytic expression of the proposed power allocation (PA) strategy. The gains due to the proposed scheme are compared with the classical null-space projection (NSP) beamforming scheme based on its closed form expression of optimal PA strategy. It is stated in [85] that the proposed power allocation scheme exhibits a percentage gain of over 60% in secrecy rate, compared to typical power allocation parameters. As regards SNR, it was observed that an increase in PA factor from 0 to 1 also increases attainable secrecy rate in low SNR regions. It was equally observed that the optimal PA factor enlarges, tending towards 1, with an increase in number of antennas, in the medium and high SNR regions.

Fig. 2.15 depicts the actual schematic of the proposed power allocation based DM scheme. It represents a scenario where Alice is equipped with three antennas whereas Bob and Eve only possess one each. The scheme assumed presence of LOS path in all scenarios thus the transmitted baseband signal is represented as [85]:

$$\mathbf{s} = \sqrt{\beta P_s}\mathbf{v}_b x + \sqrt{(1-\beta)P_s}\mathbf{P}_{AN}\mathbf{z} \tag{2.10}$$

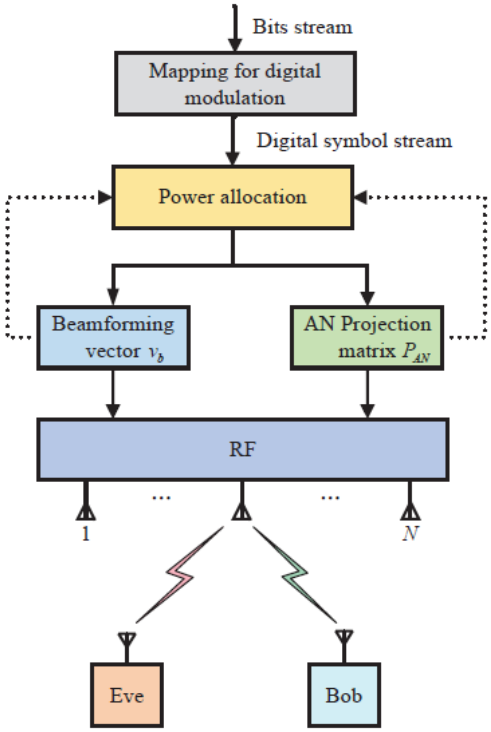

Figure 2.15: Schematic diagram of the proposed power allocation based directional modulation system [85]

where P_s is the total transmission power, β and $(1-\beta)$ represent the power allocation parameters of the information to be transmitted and the artificial noise respectively. $\mathbf{v}_b \in \mathbb{C}^{Nx1}$ represents the tranmit beamfroming vector for controlling the data to be transmitted to the pre-defined direction, $\mathbf{P}_{AN} \in \mathbb{C}^{NxN}$ is the projection matrix that directs artificial noise to the unwanted direction, where $v_b^H v_b = 1$ and $\mathrm{Tr}[\mathbf{P}_{AN}\mathbf{P}_{AN}^H] = 1$. In (2.10), x is the message to be transmitted that has to attain $E\{x^H x\} = 1$ and $\mathbf{z} \in \mathbb{C}^{Nx1}$ denotes the artificial noise vector with complex Gaussian distribution. The details of the implemented are out of scope for this work but are well outlined in [85].

2.3.1 Metrics for analysing DM Systems perfomance

Multiple proposition have been made for the acceptable metric upon which to analyze DM performance. One such metric is the normalized error rate adopted in [73, 77]. However this approach did not account for magnitude and phase reference of detected constellation patterns were defined. Also having not considered channel noise and coding approach, this metric is not able to account for differences in performance given scenarios where: A constellation symbol is constrained within its optimal compartment decoding, say different locations with a QPSK quadrant; A constellation falls into a different compartment all together. With this omission, a DM systems 'error rate' is thus challenging to use for systematic analysis.

In [86] an error-vector-magnitude-like figure of merit, that defines the capability of constellation patter distortion in DM systems is defined. This scheme faces the same challenges of lack of channel noise and coding strategy consideration. In addition, it was noted that its computation does generate distinct values for static and dynamic systems because they employ different constellation patterns.

In [80], i.e., the dual beam beam directional modulation earlier mentioned, it is the bit error rate (BER) that is employed to analyse the performance of the QPSK DM system proposed. The closed-form QPSK BER lower bound equation for static DM scheme evaluation was proposed as the metric of choice for [67, 66].

In [87] it was demonstrated that BER computed from closed from equations or transmitted data streams together with secrecy rate was adequate metrics for evaluating static DM systems. Secrecy rate being a metric already in wide use in the information theory and specifically the cryptography field. It was equally demonstrated that for dynamic DM systems that experience zero-mean Gaussian distributed orthogonal interference, EVM-like metrics, BER, and secrecy rate exhibited similar results that could as well be inter-converted.

2.3.2 Conclusions on Directional Modulation

While DM can address the issue faced by beamforming of having a ZOR size that depends upon the received SNR, and hence upon the user hardware and conditions, it however does not overcome the limitation introduced by the inversely proportional relationship between array aperture size and beamwidth. Indeed, its focusing performance, i.e., its angular selectivity, highly depends of the environment, and for most DM techniques in a LOS case, are not better than beamforming.

2.4 Time reversal

Time reversal is a two-stage technique employed to spatially focus signal via a rich scattering environment [88]. The stages involved are: channel estimation and precoded data transmission. In the channel estimation stage, the transmitter sends a short pilot signal through the rich scattering channel, thus, enabling the transmitter to obtain knowledge of the channel impulse response to the intended RX. Various approaches to channel estimation can be implemented. In all cases, the channel state information (CSI) is determined by the implementation specifics, e.g., the quantization noise, the additive noise during the process, the repetition rate, and the rate of change of the channel. In the second stage, the actual data transmission, the transmitter sends the signal filtered via a time reversal filter whose response is similar to the estimated channel albeit reversed in time, i.e., the last part recorded is transmitted first. These transmitted signals are characterized by a sharp spatial focus and tight temporal compression at the source location. The characteristics mentioned above were demonstrated via laboratory experiments as shown in [89]. This technique can be used with single-antenna as well as multiple-antenna transmitters. Achieving focusing capabilities with a single-antenna system is attractive as it drastically decreases the complexity of the transmitter.

Initially much of experimentation with TR was focused on applying it for underwater communication systems as outlined in [90, 91, 92, 93]. In recent times however, the TR principle has been applied to electromagnetic waves at radio frequencies with an initial proof of viability demonstrated in [94]. The spatial focusing properties of TR for narrow-band system in the electromagnetic waves domain was also illustrated in [95]. In [96] and [97], it was demonstrated that it is possible to minimize channel delay spread from the post-processing of wide band fixed wireless access channel measurements using either time reversal or classical weighting schemes, a result which was reproduced in [98]. In addition to spatial focusing on the targeted location, which is a desirable property in view of the low probability of

intercept (LPI) in the communication by receivers located at the unwanted location, TR also exhibits statistical robustness indicating that the spatial focusing properties are observed consistently over the fading statistics of the channel [99].

More recently, the injection of artificial noise to a time-reversal precoder has been investigated in order to further enhance the secrecy of communications [100, 101, 102, 103, 104]. The artificial noise, lying in the null-space of the intended receiver, does not distort the received symbols at the intended position but everywhere else. This approach can help improving geocasting in a similar way than DM can improve beamforming to geocast data toward ZOR whose size does not depend too much on the SNR, and therefore on the receiver capabilities (LNA gain ,noise floor...).

2.4.1 Conclusions on Time Reversal

Using TR to perform geocasting exhibits some major drawbacks. When using a single-antenna transmitter, the focusing gain depends on the multipath richness of the propagation channel environment. In a pure LOS environment, no gain is achieved. Furthermore, in rich multipath environments, the size of the area where a focusing gain can be achieved depends on the environment and cannot be controlled. Finally, whether single- or multiple-antenna transmitters, the focusing gain obtained with time-reversal precoder is achieved only when the transmitter knows the exact CSI, which is contradictory with the idea of geocasting data while respecting user privacy.

2.5 Conclusion

This chapter reviewed physical solutions that enable the wireless geocasting of information to specific spatial locations, namely, beamforming, Directional Modulation (DM), and Time Reversal (TR). Regardless the technique, the problem is to find a way for a base station to perform wireless transmission of data that can only be decoded within desired areas. To do so at the physical layer, base stations have to exhibit spatial focusing capabilities.

Beamforming is a signal processing technique used together with phased array antennas to focus signal energy towards a pre-determined direction or location, in our case this could be the direction of the predefined geographical address, i.e., the ZOR. Research on beamforming and phased arrays has been ongoing over decades now [105, 2, 106, 107, 108]. As we have seen in previous sections, beamforming suffers certain inherent limitations. The main one being that to attain narrower beamwidth of the radiation pattern, it is required to increase the aperture size of the used antenna array. DM and TR do not improve this relationship in LOS environments and in a controlable way.

Consequently, to overcome these limitations, we introduce Spatial Data Focusing (SDF). In SDF, it is the transmitted data that is focused rather than the transmitted power. The idea is to process the data in order to be decodable only at a pre-determined area. This thesis seeks to demonstrate that focusing only the data is spatially more selective than classical power focusing, at the expense of loosing the antenna array gain. The required transceiver systems will therefore require minimal infrastructure as only a limited number of transmitting antennas will be necessary in order to achieve enhanced angular selectivity. Chapter 3 introduces the concept of SDF using a spread spectrum technique in LOS environments while Chapter 4 assesses the robustness of the proposed approach in the presence of multipaths.

Chapter 3

Spatial Data Focusing (SDF)

Introduction

We have recently proposed Spatial Data Focusing (SDF) as an alternative candidate to classical beamforming in geocasting schemes [3]. In SDF, it is the data to be transmitted that is focused, i.e., tagged to a specific spatial location. To do so, data to be transmitted are processed in such a manner that they can only be decoded at a predefined location. SDF can be contrasted to classical power focusing approaches where focusing is carried out by directing energy (radiation patterns) towards a given direction. Therefore, in SDF, beamwidth refers to the region within which the transmitted data can be correctly decoded, i.e., the angular region where the BER is low enough, as opposed to the classical definition of half-power beamwidth in power focusing techniques. In terms of implementation, SDF is similar to the DM techniques covered in Section 2.3. However, DM typically involves an optimization to scramble constellations outside the main beam while simultaneously ensuring a given array factor exploiting coherent addition of radiated waves to achieve power focusing. SDF does completely release the power focusing constraint which enables achieving narrower geocast areas at the expense of the array gain, as we show in this chapter and in our preliminary investigations [3, 109, 110, 111, 112, 113]. Furthermore, the SDF precoding does not involve any optimization but a multidimensional mapping, and is therefore less demanding in terms of computing resources. We investigate in this chapter a new dedicated SDF precoding based on spread-spectrum multidimensional mapping in order to achieve a more robust SDF scheme in multipath environments [114, 115].

This chapter is organised as follows: Section 3.1 outlines a general overview of the SDF system; Section 3.2 reviews the different approaches to orthogonal signaling and describes with the aid of analytical expressions the benefits accrued when orthogonal signals are privileged over non-coded ones. Section 3.3 discusses the concept of spread spectrum modulation, covering aspects of pseudo-random codes classification and generation, with a focus on orthogonal codes and the underlying correlation properties. Section 3.4 introduces the principles of Direct Sequence Spread Spectrum - Spatial Data Focusing (DSSS-SDF). It discusses the DSSS-SDF transceiver architecture, choice of spreading codes, and its operation over LOS channel models. Analytical derivations are implemented to give physical insights regarding the operation principle as well as to validate numerical simulations used for the performance analysis. Section 3.5 introduces quadrature components to DSSS-SDF. IQ resources provide an additional degree of freedom to the DSSS-SDF scheme, further enhancing the performance by enabling SDF-dedicated channel estimation and equalization.

3.1 Spatial Data Focusing framework

Fig. 3.1 illustrates the framework of the SDF system. It depicts SDF as a Multiple-

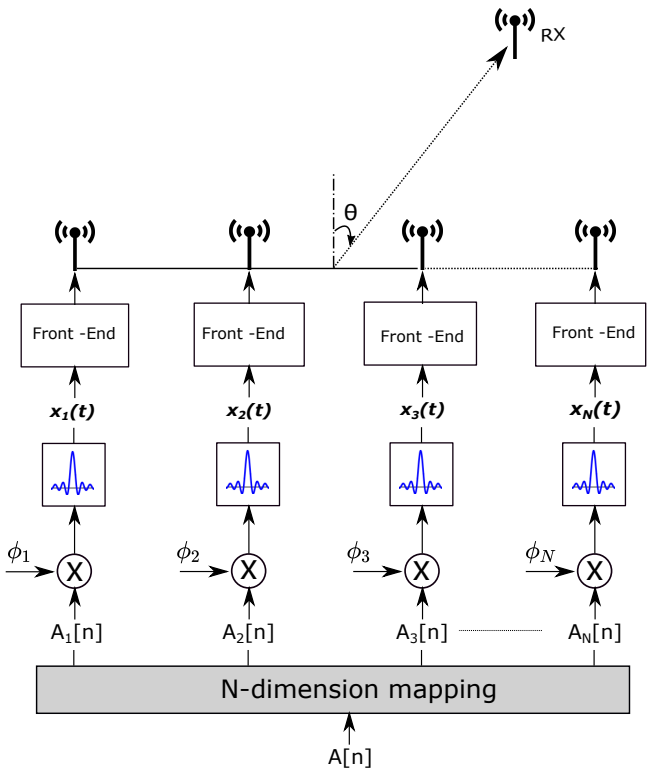

Figure 3.1: Spatial Data Focusing (SDF) scheme using N dimensions and N antennas antennas

Input Single-Output (MISO) scheme consisting of a multiple-antenna Base Station (BS) and a single-antenna user. The BS includes an N-dimensional mapper and N chains, each one including, an orthogonal signaling block, a pulse shaping filter, a front-end, and finally an antenna. The symbols to be transmitted, $A[n]$, with n the symbol index, are mapped onto an N-dimension symbol space leading to a vector representation of the symbols to be transmitted: $\mathbf{A}[n] = (A_1[n], A_2[n], ..., A_N[n])$. The orthogonality of the symbol space is physically ensured by the use of a set of N orthogonal functions $\Phi_1(t), \Phi_2(t), ..., \Phi_N(t)$ used in a spreading process prior to pulse shaping. The output signals of the pulse shaping filter, $x_1(t), x_2(t), ..., x_N(t)$, are subsequently fed into unique front-ends and radiated by unique elements of the antenna array for transmission. The user receives the composite signal made up of the sum of the transmitted signal from the different array elements and performs a dedicated symbol estimation. The received signal can be therefore expressed in baseband as:

$$r = \mathbf{hx} + n \tag{3.1}$$

with $\mathbf{h} = (h_1, h_2, ..., h_N)$, the MISO channel and n, the noise at the receiver. In this architecture, the transmitted signals $x_1(t), x_2(t), ..., x_N(t)$ are not correlated between each others and therefore the average interference pattern, i.e., the array factor, does not exhibit any preferential angular direction of propagation. As such, no power focusing gain is achieved. The radiation pattern of the array is consequently similar to the single element one.

While SDF looses the benefit of the array gain, it takes advantage of the orthogonality of the signal's dimensions to perform a dedicated channel estimation and equalization. Indeed, as explained in following sections, by using a single dimension, i.e., a single channel, as a reference for estimation, equalization, and synchronization, high angular selectivity can be achieved on the received estimated signal. So the performance of the SDF system relies on the orthogonal signaling scheme at the transmitter. In [3] and [109], SDF is implemented with time domain orthogonal pulses. This work on the other hand, proposes SDF implementation using spread spectrum modulation to generate the orthogonal signal basis using spreading codes. The goal being that in addition to the robust orthogonal signaling, the system will equally benefit from the inherent spread spectrum advantages like cross-talk elimination, reduced effect of multipath fading, low probability of detection, and low probability of interference/jamming. Successful deployment of the Direct Sequence Spread Spectrum - Spatial Data Focusing (DSSS-SDF) scheme is pegged on appropriate choice of orthogonal spreading sequences and efficient transceiver design.

3.2 Orthogonal Signaling

3.2.1 Review

Orthogonal signaling is at the core of the SDF system. The concept of orthogonal signals describes a set of signals whose inner product is zero, and is given as:

$$\sum_{q=0}^{L_c-1} x[q]y[q] = 0 \tag{3.2}$$

where L_c is the sequence length. Equation (3.2) is quite similar to classical correlation equation save for the absence of the normalizing factor $1/L_c$. In essence signals that are orthogonal are uncorrelated, as such, standard correlation equations could be used to test for orthogonality. The key characteristics of orthogonal signals is that, on combining multiple orthogonal signals, they do not interact with each other within the composite signal. It is still possible to manipulate each signal with no specific regard to the remaining signals in the summation. Two or more signals can be orthogonal to all other members in the family. Such families of orthogonal signals are referred to as orthogonal sets, and their formation is reviewed in Section 3.2.2. Orthogonal signaling is largely a coding technique, therefore, to evaluate its benefits, its performance may be compared with that of 'non-coded' schemes, i.e., direct from source binary bit streams. These two cases are illustrated as binary transmission modes in Fig. 3.2.

Fig. 3.2a represents a typical signal pair in a direct source binary bit stream signal transmission. Assuming the bits are transmitted as optimal antipodal bit pairs, each bit with applied energy E_b, given a block of m consecutive bits, it is observed that any bit patterns is possible, including those that differ by just a single bit. The minimum squared distance between different m-bit block signals is thus equal to the squared distance between the single-bit antipodal signals (i.e., the case where 2 symbols differ by just a single bit), and is given as, $d^2_{min,u} = 4E_b$, where u stands for 'uncoded'. Fig. 3.2b on the other hand depicts a typical orthogonal coding case with the m-bit blocks transmitted as orthogonal signals of energy mE_b, with each bit still having energy E_b. Orthogonal coding is characterized by equidistant signals regardless the considered symbols, thus, the squared distance between them can be expressed as $d^2_{min,ort} = 2mE_b$. Comparing the coded with the non-coded case, it is evident that

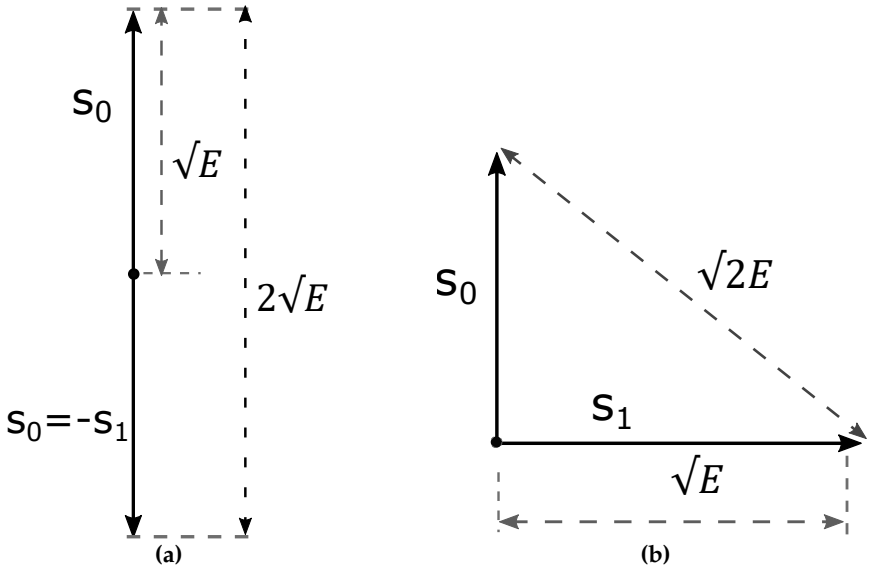

Figure 3.2: Signal pairs in binary transmission modes. (a). Direct source bit streaming. (b) Orthogonal coding

to get identical minimum distances, the non-coded bit stream transmission requires an energy gain $G_a = m/2$ times higher than that of orthogonal signaling. G_a, the asymptotic orthogonal coding gain, is thus sufficient measure of the advantages of orthogonal coding as SNR tends to infinity. Under high SNR regime, the error probability can be approximated by the union bound as [116]:

$$P_e \sim \frac{n_{min}}{M} Q\left(\sqrt{\frac{d^2_{min}}{2N_o}}\right) \qquad \text{for} \qquad \frac{d^2_{min}}{2N_o} \gg 1 \tag{3.3}$$

where $n_{min} = M(M-1)$, i.e., the number of signals with minimum Euclidean distances from a transmitted one, M is the constellation size, and N_0 is the noise spectral density. In (3.3), it is clear that the minimum Euclidean distance determines the error probability irrespective of the M-ary transmission environment. By replacing the minimum squared distances given earlier for the un-coded and coded cases, namely, $d^2_{min,u} = 4E_b$ and $d^2_{min,ort} = 2mE_b$ respectively, we obtain the probability of error performance as a function of SNR in Fig. 3.3. The black curve shows the probability of wrong reception of a non-coded block and the blue curve for the coded block. $m = 6$ bits are used per block with $M = 2^m$ orthogonal signals. It is thus observed that the coded case naturally outperforms the un-coded case as the error probability is lower for a given SNR. In the range of Pe from 10^{-2} to 10^{-6} actual gain G of orthogonal signaling increases from 3.5 to 4.2 dB. As (3.3) is valid for high SNR only, an exact for error probability of coherent reception of M orthogonal signals is also considered as given by [117]:

$$P_{e,ort} = 1 - \int_{-\infty}^{\infty} \exp\left[-\frac{(x - q_b\sqrt{m})^2}{2}\right] \Phi^{M-1}(x)\mathrm{d}x \tag{3.4}$$

where $q_b = \sqrt{2E_b/N_o}$ is the SNR per bit and $\Phi(x) = 1 - Q(x)$ is the error function. Results obtained with (3.4) are plotted in red in Fig. 3.3 and converge well to the union bound expression at high SNR regime.

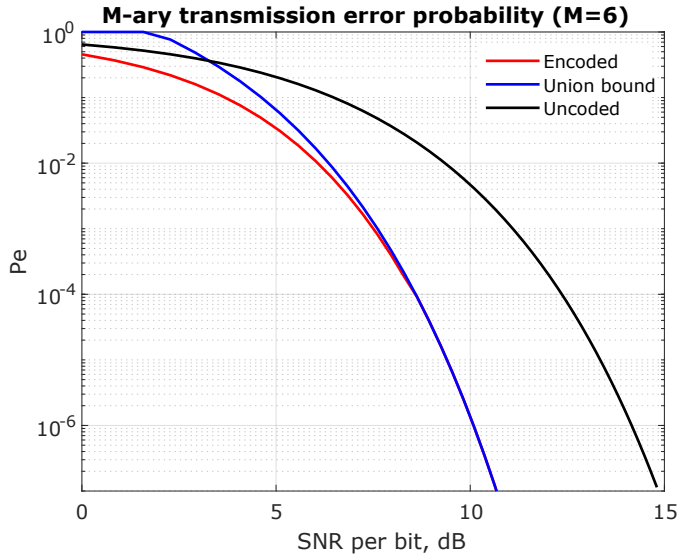

Figure 3.3: Binary transmission modes

3.2.2 Orthogonal signaling design approaches

This section looks at the various approaches employed in exploiting signal resources to realise orthogonal signal sets. The three methods reviewed are time-shift coding, frequency shift coding, and spread spectrum orthogonal coding.

Time-shift coding

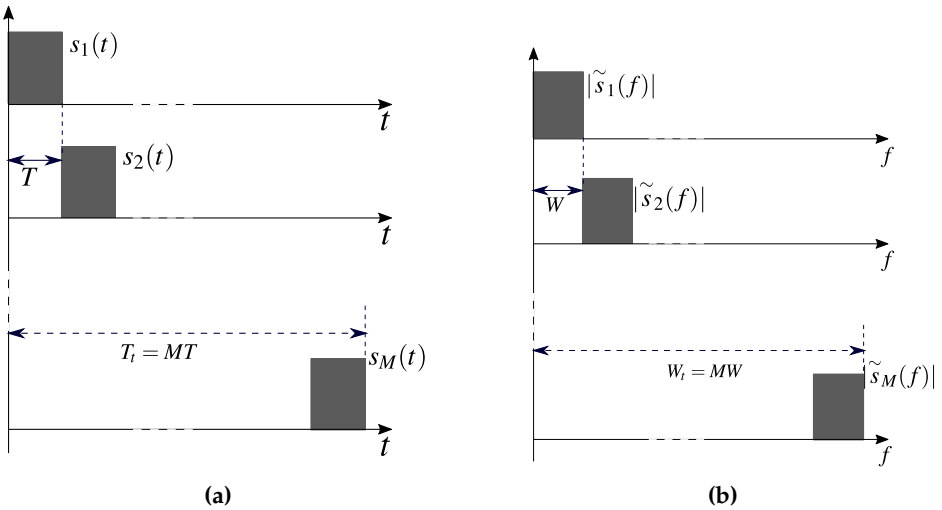

Figure 3.4: Orthogonal signals (a). Time-shift coded (b).Frequency-shift coded [116]

Fig. 3.4a represents orthogonal signals set occupying a time period T_t. Each signal has a duration $T = T_t/M$ and is time shifted by time T. $M = T_t/T$, is the maximum number of signals that can be contained within a given time resource. Orthogonality in this case is realized due to the fact that the inner product of the time-shifted signals is zero. Each signal occupies a bandwidth $W = 1/T$, they can thus all occupy the same bandwidth without violation of orthogonality: $W = W_t$. This approach to signal orthogonality is quite simple to implement, however, it suffers the

limitation that any potential fluctuations of the signal time positions is detrimental for orthogonality, this may lead to quite complex synchronization requirements. Although secure safety margins between signals can be introduced to minimize this limitation, this has to be traded off with spectral efficiency.

Frequency-shift coding

Frequency-shift coding is an alternative approach for achieving signal orthogonality. It is directly related to time-shift coding by time–frequency duality, i.e., the dot products of signals $u(t)$, $v(t)$ and that of their spectra $\tilde{u}(f)$, $\tilde{v}(f)$ coincide as:

$$(\mathbf{u}, \mathbf{v}) = \int_{-\infty}^{\infty} u(t)v(t)\mathrm{d}t = \int_{-\infty}^{\infty} \tilde{\mathbf{u}}(f)\tilde{\mathbf{v}}^*(f)\mathrm{d}f = (\tilde{\mathbf{u}}, \tilde{\mathbf{v}}) \tag{3.5}$$

This allows the use of similar concepts discussed in time-shifting coding to be used in frequency-shift coding. As shown in Fig. 3.4b, the signals do overlap in time ($T = T_t$) each with a bandwidth $W = 1/T_t$. The total number of orthogonal signals attainable with this approach is given as $M = W_t/W = W_t T_t$, which is basically the total available signal space.

Spread spectrum orthogonal coding

Resource fragmentation as discussed in the time and frequency shift orthogonal coding is limited by an increasing M, i.e., as M increases the resource fragmentation quickly becomes unsustainable, in such cases spread spectrum orthogonal signaling maybe preferred as it allows all signals to share the entirety of the time-frequency resource with no distributions or slicing required. To realise M signals of L_c consecutive chips, each having the same rectangular shape and duration T_c, let the chip polarities of the kth signal (assume BPSK transmission) be manipulated by a code sequence of binary symbols $C_{k,q} = \pm 1$, where $k = 1, 2, ..., M$ and the chip index number $q = 0, 1, ..., L_c - 1$. This signal can be represented in baseband as:

$$s_k(t) = \sum_{q=0}^{L_c-1} C_{k,q}\, p(t - qT_c) \tag{3.6}$$

where $p(t)$ represents rectangular chips of duration T_c. The inner product of the kth and lth signals can be given as:

$$(s_k, s_l) = \sum_{q=0}^{L_c-1} \sum_{j=0}^{L_c-1} C_{k,q} C_{l,j} \int_0^T p(t - qT_c)p(t - jT_c)\mathrm{d}t \tag{3.7}$$

The integral in (3.7) is the cross correlation of two chips time-shifted to each other by $(q - j)T_c$. When $q \neq j$, this cross-correlation outputs zero because the chips in the integral do not overlap in time. Thus:

$$\int_0^T p(t - qT_c)p(t - jT_c)\mathrm{d}t = E_0 \delta_{qj} \tag{3.8}$$

where E_0 is the chip energy. Substituting (3.8) in (3.6) we get:

$$(s_k, s_l) = E_0 \sum_{q=0}^{L_c-1} C_{k,q} C_{l,q} = E_0(\mathbf{C}_k, \mathbf{C}_l) \tag{3.9}$$

Equation (3.9) relates the inner product of the signals (3.6) with that of L_c-dimensional vectors of the corresponding spreading sequences $\mathbf{C}_k = (C_{k,0}, C_{k,1}, ..., C_{k,L_c-1})$. Evidently, M orthogonal code sequences do generate a set of M orthogonal signals via (3.6). Fig.3.5 illustrates the resource allocation in orthogonal spread-spectrum signaling. It depicts the absence of classical resource distribution, instead the signals overlap both in time and frequency domains.

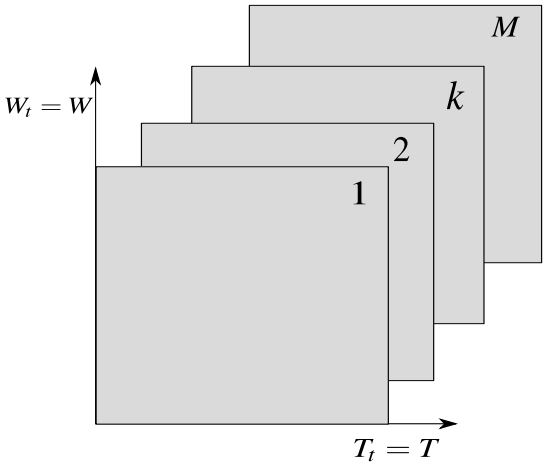

Figure 3.5: Resource allocation in orthogonal spread-spectrum signaling [116]

Each signal has a bandwidth $W = 1/T_c$, and the symbol duration is $T = L_c T_c$ thus producing $WT = L_c = W_t T_t$. Clearly, orthogonality is now due to an appropriate signal modulation, as opposed to either time interval or spectral fragmentation.

3.3 Spread Spectrum Modulation

Spread spectrum is an RF communication system in which the baseband signal bandwidth is intentionally spread over a larger bandwidth by injecting a higher frequency signal. As a direct consequence, energy used in transmitting the signal is spread over a wider bandwidth, and may appear as noise [118] [63], as it was initially proposed for military applications due its inherent low probability of detection and interception properties. It also benefits from multipath rejection capabilities, making this technology equally interesting in classical civilian wireless systems, specifically in schemes that require multiple access capabilities, like in the second and third generation of mobile phone standards (e.g., IS-95 in 2G, CDMA2000 in 3G). The two common approaches to spread spectrum modulation are: *direct sequence* and *frequency hopping*. The work in this thesis is based on DSSS modulation, where the data signal $d(t)$, with symbols of duration T, is multiplied by a pseudo-random sequence (code) $c(t)$ composed of L_c coefficient $c_q \in \pm 1$ and thus L_c symbols referred to as chips. This process leads to expanding the bandwidth since $T_c = T/L_c$, where T_c is the chip duration. The 3 dB bandwidth W_c of $c(t)$ is approximately L_c times that of $d(t)$, i.e., $W_c = L_c W$, and $d(t) \times c(t) = d(f) * c(f)$, this process is illustrated in Fig. 3.6 where the first plot represents the data signal $d(t)$, the second one represents the spreading sequence $c(t)$, and the last one represents the spread sequence $d(t)c(t)$. The ratio of the signal bandwidth after spreading to that of the original signal bandwidth, i.e., the spreading factor, is given as $SF = W_c/W \approx L_c$, SF determines the extent of both interference and multipath rejection at the receiver [116].

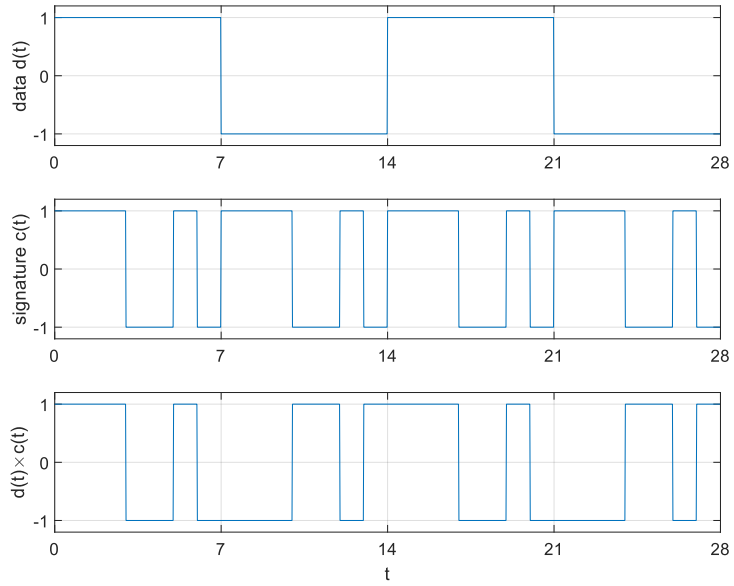

Figure 3.6: From top to bottom: Data, code, and spread signal

3.3.1 Classification of spreading codes

Spreading codes can be generally classified as: real or complex codes, orthogonal or non-orthogonal codes, and analog or digital codes.

Orthogonal vs. non-orthogonal codes

Orthogonal codes are characterized by pairwise cross-correlation function that return zero. They find application in schemes where it is required to transmit multiple data streams simultaneously over the same frequency band. This characteristic is enabled by the availability of synchronization mechanisms able to align the codes in time. The number of possible simultaneous transmissions is determined by the cross-correlation properties of the given orthogonal codes [63, 118].

Non-orthogonal codes, also referred to as quasi-orthogonal codes, are primarily optimised for bandwidth expansion, and their pair-wise cross-correlation function is low but does not rigorously return zero. They may also be employed for simultaneous data transmission, however separate modalities must be put in place to distinguish the different channels [119]. A typical case would be to use quasi-orthogonal codes (e.g., PN sequences) for bandwidth expansion and orthogonal codes (e.g., Walsh sequences) for channel separation in the same system.

Real vs. complex codes

As the name suggests, real codes are solely composed of real components viz; $\mathbf{C}(t) = [c_1(t), c_2(t), ..., c_{L_c}(t)]$. Complex codes on the other hand can be defined as, $\mathbf{C}(t) = [c_1^I(t) + jc_2^Q(t), ..., c_{L_c}^I(t) + jc_{L_c}^Q(t)]$, where $c_i^I(t)$ and $c_i^Q(t)$ are the real and imaginary component sequences respectively. Complex codes can either be derived from a family of constant-envelope root-of-unity filtered complex spreading sequences [120], or be selected as two distinct but equal length code sequences. Conventionally complex codes are transmitted over quadrature carriers to separate the real and imaginary components. $\mathbf{C}(t)$ can be used to spread one or two real data streams. They may

also be used to implement a multi-dimensional modulation architecture, however, this is determined by the correlation properties of $c_i^I(t)$ and $jc_i^Q(t)$ [121].

Analog vs. digital codes

Analog spreading codes are finite-length code sequences whose chips are extracted from a continuous stream of values, examples would be the Huffman and analog chaotic sequences [122] [123]. Digital spreading codes on the other hand are codes that are parts of a well defined finite-size alphabet.

3.3.2 Pseudo-Noise (PN)

Pseudo-random sequences are *noise-like* deterministic bit sequences consisting of $+1$ and -1, they are also referred to as Pseudo-Noise (PN) signal and can viewed as signature codes that need to be known by both the transmitter and receiver as to facilitate efficient decoding of transmitted information. They do exhibit the following noise-like properties [124]: (1) Balance, PN sequence of length $L_c = 2^n - 1$ contains 2^{n-1} ones and $2^{n-1} - 1$ zeros; (2) Runs, for any PN sequence, $1/2$ of the runs have length 1, $1/4$ have length 2, $1/8$ have length 3, $1/16$ have length 4, e.t.c, and for all the cases, the number of runs of 0's is equal to the number of runs of 1's. In this case a run is defined as a string of continuous values; (3) Good auto-correlation and cross-correlation properties.

The choice of spreading codes in this work is critical in regard to capacity to mitigate against both multipath and inter-channel interference, as such, it is required that: The generated code sequences must be periodic with a constant length; they must be easy to differentiate from their time-shifted versions; and finally they must be easy to distinguish form other code sequences. The first and the second requirements are important with respect to potential multipath effects due to the considered propagation environment, whereas the third one takes care of instances of multi-access capability in communication systems. For the first and the second requirement, the measurement of the level of distinction of the codes is carried out by an autocorrelation and cross-correlation functions respectively. The autocorrelation function measures the level of distinction, and it is expressed as:

$$R_{xx}(t) = \frac{1}{T}\int_0^T X(t)X(t+\tau)d\tau \tag{3.10}$$

The cross-correlation function on the other hand, determines the extent of correlation between different codes sequences, say, $X(t)$ and $Y(t)$. It is expressed as:

$$R_{xy}(t) = \frac{1}{T}\int_0^T X(t)Y(t+\tau)d\tau \tag{3.11}$$

The two functions summarized above are used to evaluate the spreading codes.

The next section discusses the techniques use for generating spreading sequences used in this work. It also briefly describes some other codes families that have not been necessarily used in this work.

Code Generation by Linear Feedback Shift Registers

Multiple approaches to code sequence generation do exist. In this work, we focus on the generation using Linear Feedback Shift Registers (LFSR). A shift register is

a type of digital circuit made of multiple cells, each doubling as a storage unit that, under the control of a clock pulse, shifts its contents to its output while reading new content from its input. In typical LFSR configurations, the input of a given cell m, is a function of the output of cell $m-1$, and the output of the last cell determines the desired code sequence. Fig. 3.7 depicts a linear binary shift register, that can generate codes from the polynomial $g(x) = x^5 + x^2 + 1$. The configuration of a m-section LFSR can be described by a binary generator polynomial of degree m as:

$$g(X) = g_1 x^m + g_{m-1} x^{m-1} + g_{m-2} x^{m-2} + \cdots + g_1 x^1 + 1 \quad (g_i \in 0, 1) \tag{3.12}$$

A typical case is depicted in Fig. 3.7, whose polynomial is given as, $g(x) = x^5 + x^2 + 1$, with initialization $g_0 = g_2 = 1$, and $g_m = 0$, such shift registers are sufficient for generating spreading sequences.

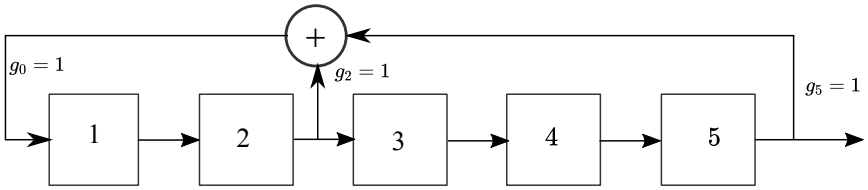

Figure 3.7: Linear feedback shift register

M-Sequence generation

M-sequences can be generated using single linear shift register. The 'M' in M-sequence stands for 'maximal' as they are sequences with a maximum possible period, ($L_c = 2^m - 1$) that can be generated by a m-stage binary LFSR. They are generated using primitive degree m generator polynomials, and are characterized by inherent shift-and-add, balance, and run-length properties [125] [126] [127]. The periodic autocorrelation function of M-sequences is given by,

$$R_{xx}(t) = \begin{cases} 1 & \text{for } n = Mod\ L_c \\ -\dfrac{1}{L_c} & \text{otherwise} \end{cases}$$

Depending on the desired use case, the number of registers, the initial value, and taps can be implemented on the chosen polynomial. A good example is shown in Fig. 3.8 where 3 registers, with initial values as 111, and feedback tap positions in the first and third taps, represented by polynomial $g(x) = x^3 + x + 1$ is shown.

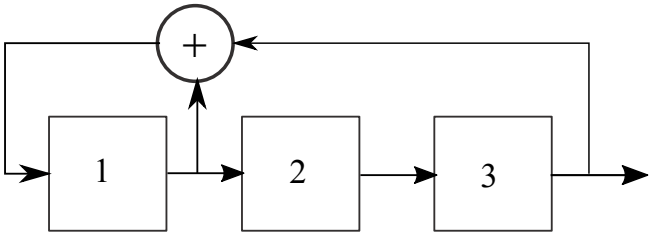

Figure 3.8: 3-stage linear feedback shift register

Based on M-sequences, other spreading codes can be generated.

Gold sequences

These are codes generated by the modulo-2 operation of preferred pair equal length m-sequences [128]. Specifically, from a pair of preferred sequences, Gold sequences are generated by the modulo-2 sum of the first with shifted versions of the second. Given a period of $L_c = 2^m - 1$, there are L_c possible circular shifts. It is thus possible to generate L_c Gold sequences given a pair of m-sequences of length L_c [124, 129]. This approach is depicted in Fig. 3.9. Gold codes exhibit inferior auto-correlation properties compared to m-sequences. Indeed, in the generated Gold code family, only the initial preferred pair are m-sequences, the derivatives are not. Unlike m-sequences that have two level autocorrelation values, Gold codes have three level valued autocorrelation spectrum. They are preferable when the priority of the communication system is security, given that their family size is significantly larger than that of PN codes.

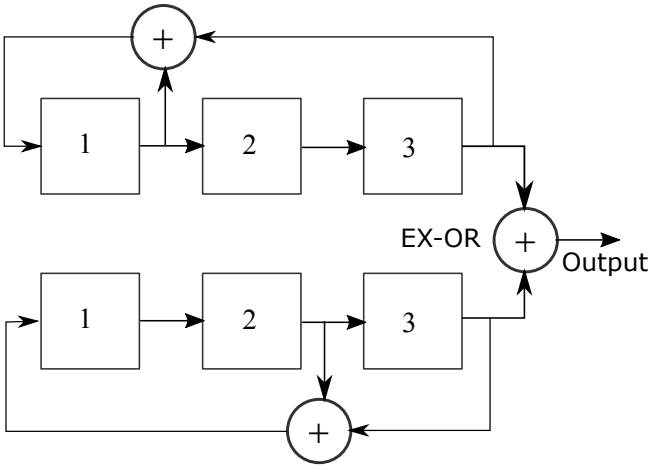

Figure 3.9: A 3- stage Gold sequence generator

Other PN sequences: There exists multiple other PN sequences in the literature, however they are out of scope for this work. They include: Gold-like PN sequences [130]; Barker sequences and Barker-like sequences [131, 132, 133, 134]; and Kasami sequences [130, 135].

3.3.3 Orthogonal codes

As earlier described in Section 3.3.1, two sequences are said to be orthogonal if the inner products between them is zero. In other words, if $c_i(\tau)$ and $c_j(\tau)$ are the i^{th} and j^{th} orthogonal members of a given code family, each of code length L_c, and τ_s as the chip duration, then the orthogonal property is expressed as:

$$R_c(\tau_s) = \sum_{k=0}^{L_c-1} c_i(k\tau_s)c_j(k\tau_s) = 0 \quad \forall\, i \neq j \tag{3.13}$$

Orthogonal codes used in this work include Walsh-Hadamard codes and orthogonal Gold codes, whose details are therefore given hereafter.

Walsh Hadarmard (WH) Codes

Walsh codes are generated by applying the Hadamard transform to an 1×1 dimensional zero matrix repeatedly [125, 136, 137]. The process can be summarised as:

starting with a seed of 0, then replicating it horizontally and vertically, and then complementing the 1 diagonally, in this way an orthogonal code (Matrix) is obtained. This process is to be continued with the newly generated block until the desired codes with the proper length are generated. Sequences generated in such a manner are referred as 'Walsh' codes [138].

$$\mathbf{H_1} = \begin{bmatrix} 0 \end{bmatrix}; \quad \mathbf{H_{2n}} = \begin{bmatrix} \mathbf{H_n} & \mathbf{H_n} \\ \mathbf{H_n} & \overline{\mathbf{H}}_\mathbf{n} \end{bmatrix} \tag{3.14}$$

The left matrix in 3.14 represents a Hadamard matrix, $\mathbf{H_n}$, where $n = 2^i$ and i is an integer. It is a symmetric square-shaped matrix whose columns or rows correspond to a Walsh code of length n. Each row being orthogonal to all the other rows.

Orthogonal Gold Codes

The Gold sequences discussed in section 3.3.3 have multiple distinct codes compared to the M-sequences. However, they experience certain shortcomings: the proportion of 0s to 1s is not always balanced; the cross-correlation value of Gold sequences is not always zero in a synchronized environment; and they have odd number codes lengths, thus a special clock is required for their generation. The limitations described above are mitigated by simply adding one chip to the Gold codes to balance the proportion of 0 to 1. Attaching a '0' to the original (quasi-orthogonal) Gold codes, generates a set of codes whose cross-correlation values are '0' at synchronous point, this new type of codes are referred to as orthogonal Gold codes.

A simple zero-padding of the output of Fig. 3.9 can be used to realise 2^m orthogonal codes. These codes do not exhibit any significant difference from Walsh codes in terms of their cross-correlation characteristics, however, their auto-correlation characteristics (ACC) are different. In essence, orthogonal Gold codes exhibit more optimal ACC than Walsh codes. This makes them desirable in applications where it is preferable to keep the auto-correlation values low as to prevent potential false registration of autocorrelation peaks [139]. In [140], a comparison of the two orthogonal approaches was carried out and it was observed that individual code-words of Orthogonal Gold codes perform more uniformly compared to corresponding code-words from Walsh code sets. It means that orthogonal Gold codes will indeed be preferable in practical cases where perfect orthogonality cannot be retained, e.g. over a transmission channel, this drops the requirement for a very tight synchronization scheme at the receiver. This characteristic equally comes in handy in consideration of immunity to multipath effects.

3.3.4 Correlation characteristics of spreading codes

The correlation characteristics of spreading codes are central to the spread spectrum communication signaling and in finality to the proposed SDF scheme. Spreading codes can be seen as the signatures shared by both transmitter and receiver, thus enabling the receiver to decode the transmitted spread signal. It is therefore evident that the properties of the transmitted spread signal is significantly influenced by the nature of the spreading codes used [117, 141]. Ideally the correlation function of identical codes from a given code family should output high correlation peaks whenever the code sequences in the incoming signal aligns with the one generated at the receiver. In addition, in low SNR scenario, the said peaks should be clearly higher than the peaks due to sidelobes correlation and noise, sidelobes correlation peaks being those generated due to code misalignment [63]. In the same

vein, cross-correlation values should be very low, ideally zero. Similarly, correlation between codes within a given codes family and their offsets in time must also be kept very low. This is important as spread spectrum signals need to share the same frequency band [63]. Correlation functions are classically classified as either periodic or aperiodic correlation. Given a spreading sequence with code length L_c , $C_q = [c_1, c_2, ..., c_{L_c}]$, its aperiodic auto-correlation function (AAF) can be represented as [116]:

$$R_{ac}(k) = \sum_{q=0}^{L_c-1} c_q c_{(q+k)} \tag{3.15}$$

where the shift parameter $k \in -L_c + 1 : L_c - 1$, and R_{ac} is zero out of these ranges, also, the shifted index $(q+k) \in (0 : L_c]$, given that $c_{(q+k)}$ is zero out this range. (3.15) represents a spreading code that is shifted to the right over itself as the dot product is calculated for each shift. The AAF function considers cases where the correlation is carried out over a single spreading sequence. In cases where auto-correlation is to be carried over a repeating code sequence, then the periodic auto-correlation function (PAF) is preferred, PAF is represented as:

$$R_{cc}(k) = \sum_{q=0}^{L_c-1} c_q c_{(q+k)\ mod\ L_c} \quad c_0 = c_{L_c} \tag{3.16}$$

The modulus operator removes the restriction on k such that when $(q+k)\ mod\ L_c = 0$, i.e., when chip c_0 is needed, it is substituted with c_{L_c}. This set up permanently keeps index value within $[1 : L_c]$ with respect to the spreading code definition $C = [c_1, c_2, ..., c_{L_c}]$. (3.16) can thus be simplified as a case of performing autocorrelation between a given spreading code and a long incoming stream of similar codes. This is exactly what happens in typical burst communication schemes where the transmitted signal has embedded within it multiple spreading codes.

3.3.5 Direct Sequence Spread Spectrum (DSSS)

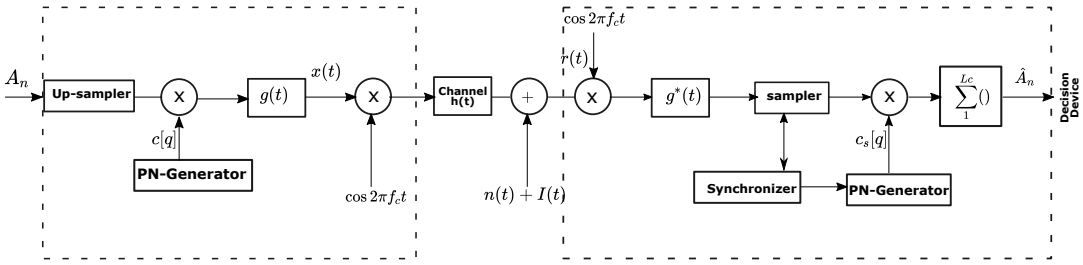

Figure 3.10: End-to-end DSSS system

Fig. 3.10 illustrates a typical end-to-end DSSS system. A_n is the symbol transmitted over the nth symbol duration. The data symbols A_n are first upsampled at the chip rate and then multiplied by the spreading codes $c[q]$. The obtained spread sequences are then filtered (i.e., pulse shaping) to form the base band signal $x(t) = \sum_n A_k g(t - nT)$, where $g(t)$ the shaping pulse, T is the symbol duration. The output of this process is then up-converted by multiplication by the carrier $\cos(2\pi f_c t)$ and transmitted via a channel $h(t)$. Depending on the nature of $h(t)$, it may introduce to the signal various form of interference $I(t)$, finally the system may also introduce additive noise $n(t)$ at the receiver. In transmission, a spreading

code delay is introduced. The received signal $r(t)$ is used to synchronize the codes generated at the receiver [142, 143].

At the receiver, $r(t)$ is down-converted, passed through a matched filter, sampled, and then despread by multiplying it with a synchronized version, $c_s[q]$, of the original spreading code $c[q]$. The output of the synchronizer depends on the propagation delay τ introduced by the channel. If the channel does not introduce multipath, then $\tau = \tau_{LOS}$. However, in the presence of multipath then the synchronizer will ideally synchronize either to the multipath component with the largest amplitude (usually the LOS path if present) or the first multipath component above a set threshold. Specifically, if $h(t) = \sum_i \alpha_i \delta(t - \tau_i)$, where α_i is the complex gain of the ith multipath component, then the synchronizer will lock to the strongest path i, setting $\tau = \tau_i$ [144]. The ith multipath component at delay τ_i is despread by multiplying it with the despread code $c(t - \tau_i)$. The multipath components falling in another channel tap (i.e., $\tau_i - \tau_{j,i\neq j} > T_c$) are not despread, and most of their energy is removed. This property is the basis of the multipath mitigation offered by spread spectrum communications. Upon despreading, the baseband signal goes to a decision device for further processing. For received signal estimation, classical DSSS receivers take a three pronged approach : down-conversion, despreading, and baseband demodulation.

3.4 Principle of DSSS based Spatial Data Focusing

In Spatial Data Focusing, the transmitter broadcasts information to a given location, irrespective of whether a receiver is located at that position at that instant. Consequently, the precoding cannot make use of any CSI knowledge, except naturally the angular direction of the ZOR. A receiver getting into that ZOR will decode the data whereas out of this zone, data cannot be decoded correctly. The data coding takes a two-pronged approach that includes mapping symbols onto an N-dimension symbol space and spreading them via appropriate spreading codes. This section introduces the basics of DSSS-SDF, looking at its general architectural overview with some focus on the question of choice of appropriate orthogonal spreading codes and symbol space mapping.

3.4.1 Transmission

Fig. 3.11 represents the architectural overview of the transmit section of the proposed scheme. It is largely divided into five blocks: N-dimensional symbol mapper,

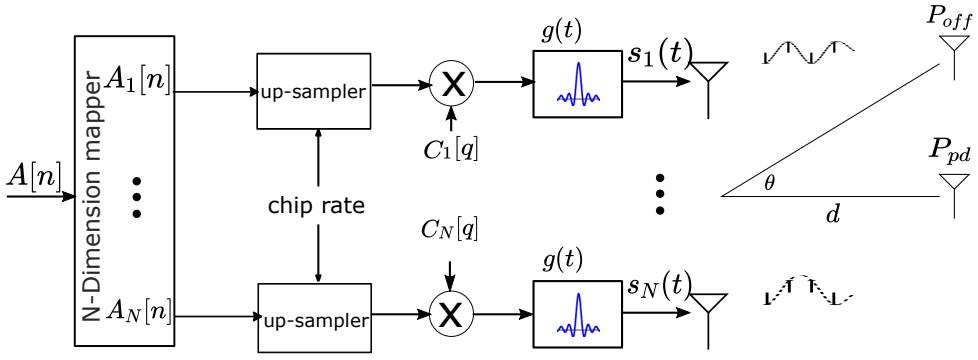

Figure 3.11: Principles of Spread Spectrum Spatial Data Focusing

spreading mechanism, pulse shaping, the antenna array, and the channel. Its operating principles is as follows. The incoming symbol stream $A[n]$ is mapped onto an N-dimensional symbol space. Each symbol projection on each dimension, i.e., each symbol coefficient, is then used to spread spectrum modulate a unique member of an N-dimensional orthogonal codes set, $\{\mathbf{C}_1, \mathbf{C}_2, ..., \mathbf{C}_N\}$. The outputs of the spreading process $\mathbf{A}_i^{up}\mathbf{C}_i$ are passed through pulse shaping filters $g(t)$, which are root raised cosine filters. The filters outputs, $s_i(t)$, are subsequently fed into unique elements of an N element antenna array. The N uncorrelated transmitted signals can be expressed as:

$$s_i(t) = \sum_{n=0}^{\infty} A_i[n] \sum_{q=0}^{L_c-1} C_i[q] g(t - nT - qT_c) \tag{3.17}$$

where n, is the symbol index, q, is the code's chip index, and $i = 1, 2, ..., N$, is the code/antenna index, T, L_c, and T_c are symbol duration, code length, and chip duration respectively. $A_i[n] \in \mathbb{Z}$ are the multi-dimensional symbol coefficients, and $\mathbf{C}_i[q] \in [1, -1]$ with $\langle \mathbf{C}_i[q], \mathbf{C}_j[q] \rangle \to 0$ for $i \neq j$.

3.4.2 Choice of spreading codes

Orthogonal signaling is a critical aspect of the SDF system. For the DSSS-SDF approach, orthogonal codes are actually the foundation of the multi-dimensional orthogonal signal basis used. Thus, to help in selecting orthogonal codes well-suited for SDF, the properties of various orthogonal code family sets are first investigated. To do so, this work focused on two orthogonal codes sets that exhibit different properties, namely, Walsh-Hadamard and Orthogonal Gold codes. In ideal cases, good autocorrelation function for orthogonal spreading sequences should be a delta function, and 0 for cross-correlation functions, in other words, autocorrelation function, $\rho(\tau) = \delta(\tau)$, and cross-correlation functions, $\rho_{i,j}(\tau) = 0$, $\forall\, i \neq j$, $\forall \tau$.

Walsh-Hadamard codes

Computer simulations are performed to characterize the correlation properties of Walsh codes. The solid red and dashed red plots in Fig. 3.12a illustrates the evaluation of their auto-correlation properties for codes made up of $L_c = 8$ and $L_C = 32$ chips (code length). It shows that Walsh codes do exhibit non-ideal auto-correlation properties for various code lengths, specifically in this case they have large auto-correlation for $\tau \neq 0$. ACF values for most of the side lobes are fairly significant compared to the peak ACF value. This kind of result is realised for over 50% of Walsh codes pairs examined, code length not withstanding. They are thus not good candidates for asynchronous transmission schemes for the reasons detailed below.

- The codes do not have a single, narrow auto-correlation peak. As a consequence code-synchronization becomes difficult, see Fig. 3.12a.
- The spreading is not very efficient as the energy is only spread over a small number of discrete frequency-components as shown in Fig. 3.14.
- Orthogonality is also significantly impacted by channel properties like multipath. In practical applications then, it will be required to implement more complicated equalization schemes to recover the transmitted information.

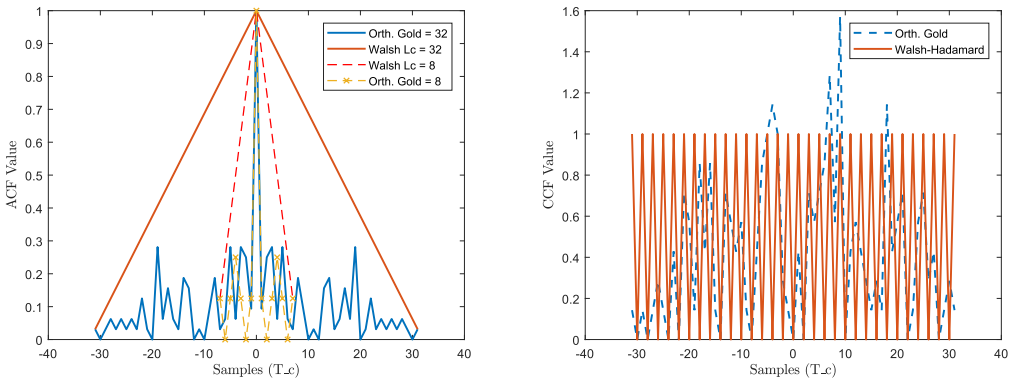

(a) **(b)**

Figure 3.12: (a) Auto-correlation functions, (b) Cross-correlation functions ($L_c = 32$), for both Walsh-Hadamard and Orthogonal Spreading sequences

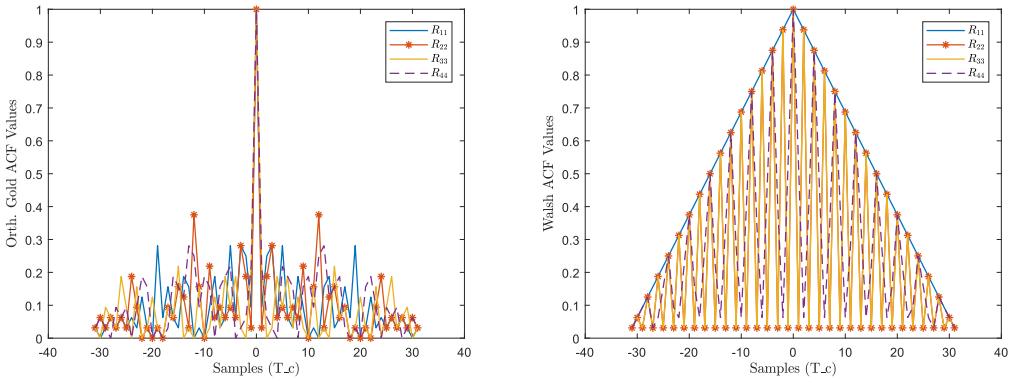

(a) **(b)**

Figure 3.13: Auto-Correlation functions between different codes within a given set of (a) Orthogonal Gold codes (b) Walsh with $L_c = 32$ chips

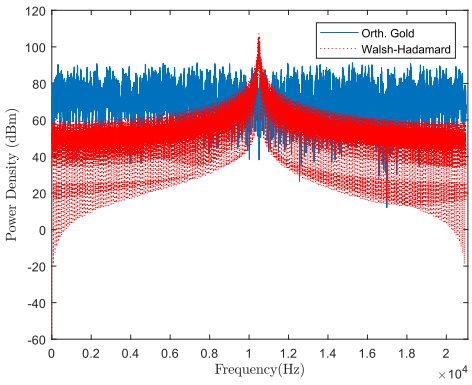

Figure 3.14: Frequency distribution of signal spread via Orth. Gold codes vs. Walsh codes with $L_c = 32$ chips over the 200 MHz signal bandwidth

Fig. 3.12b illustrates the cross-correlation results for Walsh codes (solid red plot) and orthogonal Gold codes (dashed blue plot) for code length $L_c = 32$. It is observed that both sequences do exhibit ideal cross-correlation properties with zero value at zero time shifts thus making them a good candidates for mitigating against inter-channel interference. However, all members of a given code set in Walsh codes do not exhibit uniform auto-correlation function (ACF) values for all shifts. This is observed in Fig. 3.13b where auto-correlation of the different members yield quite varying characteristics. These results mean that for orthogonality to be preserved at the receiver, Walsh codes have to be perfectly synchronized with each other.

Orthogonal Gold codes

Computer simulations are similarly used to evaluate the characteristics of orthogonal Gold codes. Fig. 3.13a illustrates the results obtained in evaluation of the auto-correlation properties. It is observed that the sidelobe levels, i.e., ACF values at non-zero time offsets, are much lower than the peak ACF values, i.e., at zero time shift. A difference of about 6dB. This kind of uniform characteristic was observed across all pairs of orthogonal Gold codes generated and evaluated, code length not withstanding. This characteristics makes orthogonal Gold codes a good candidate for asynchronous transmission applications. Indeed compared to Walsh codes, the orthogonal Gold codes exhibit superior auto-correlation properties. An evaluation of their CCF characteristics was also carried out and typical results illustrated in Fig. 3.12b. As was earlier stated, they do exhibit some characteristics similar to Walsh codes, specifically returning zero value at zero time shift. Again the above makes it a viable candidate for asynchronous transmission schemes. Finally, as shown in Fig. 3.12b, the spread in frequency is efficient even with only $L_c = 32$ chips: the power is uniformly distributed over the whole signal bandwidth.

Discussions

It was shown that orthogonal Gold codes exhibit superior properties than Walsh-Hadamard codes for asynchronous communications, code lengths L_c not withstanding. SDF can also benefit from these superior properties to achieve more robust geocasting, especially in multipath environments. However, the goal of SDF is to preserve the orthogonality of the multi-dimensional symbol space at the receiver, only in the ZOR direction. Anywhere else, the orthogonality of the received symbol space should be as degraded as possible. Consequently, operating with codes exhibiting near ideal properties could be beneficial. These hypothesises will be assessed while evaluating SDF performance in following sections.

3.4.3 Channel model

As an initial proof of concept and to assess SDF fundamental performance, the channel is firstly characterized by a free space LOS transmission model as illustrated in Fig. 3.15.

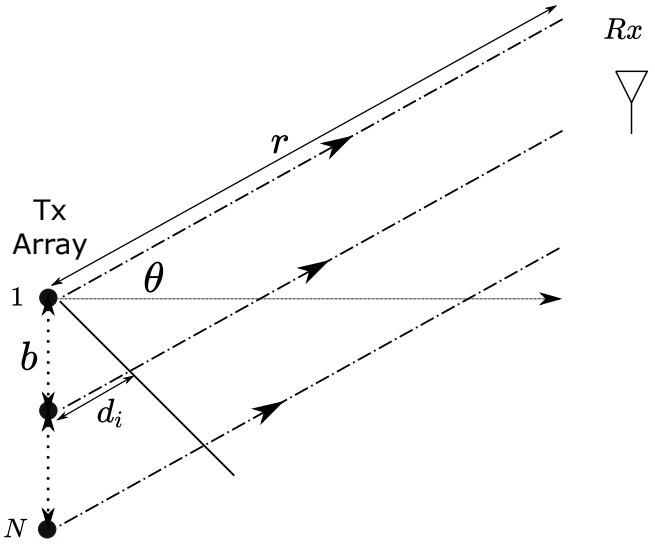

Figure 3.15: Line-of-sight (LOS) MISO channel architecture

b is the inter-element distance given as a factor of wavelength λ. Assuming far-field paraxial approximation, the channel impulse response $h_i(t)$ between the transmit and receive antennas is given as:

$$h_i(t) = \alpha_i \delta(t - \tau_i) e^{-j\omega\tau_i} \tag{3.18}$$

where α_i and $\tau_i = (r + d_i)/c$ are the respective wave attenuation constant and propagation delays between TX_i and RX, with r, the distance covered by the wave-front between the first antenna array element and the receiver, $d_i = (i-1)b\sin\theta$ with $i = 1, 2, ..., N$, is the antenna element index, and ω is the angular carrier frequency. Assuming $r \gg b$ leads to $\alpha_i = \alpha$. Without loss of generality, α is taken as equal to 1 in the following analysis. Consequently, the LOS channel model is re-written as:

$$h_i(t) = \delta(t - \tau_i) e^{-j\omega\tau_i} \tag{3.19}$$

3.4.4 Reception

The received signal, $r(t)$, can be expressed as the output of the MISO LOS channel such as:

$$r(t) = \sum_{i=1}^{N} (s_i * h_i)(t) + n(t) \tag{3.20}$$

where $n(t)$ is random Gaussian noise at the receiver. Substituting equations (3.17) and (3.19) into (3.20) leads to:

$$\begin{aligned} r(t) &= \sum_{i=1}^{N} e^{-j\omega\tau_i} \sum_{n=0}^{\infty} A_i[n] \int_{-\infty}^{\infty} \sum_{q=0}^{L_c-1} C_i[q] g(t - nT - qT_c - t') \delta(t' - \tau_i) dt' + n(t) \\ &= \sum_{i=1}^{N} e^{-j\omega\tau_i} \sum_{n=0}^{\infty} A_i[n] \sum_{q=0}^{L_c-1} C_i[q] g(t - nT - qT_c - \tau_i) + n(t) \end{aligned} \tag{3.21}$$

The received signal $r(t)$ passes through a matched filter-based receiver as illustrated in Fig. 3.16.

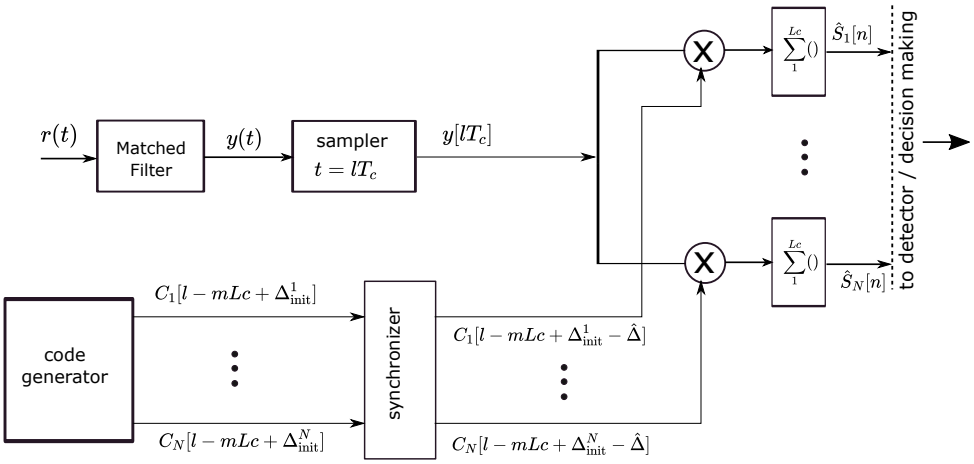

Figure 3.16: DSSS-SDF-IQ receiver architecture

The matched filter at the receiver is also a root raised cosine filter, yielding an output expressed as:

$$y(t) = r(t) * g^*(-t) = \int_{-\infty}^{\infty} r(t')g(t-t')dt'$$

Being symmetrical pulses, $g^*(-t) = g(t)$. Substituting for $r(t)$ from (3.21), $y(t)$ is further represented as:

$$y(t) = \sum_{i=1}^{N} e^{-j\omega\tau_i} \sum_{n=0}^{\infty} A_i[n] \int_{-\infty}^{\infty} \sum_{q=0}^{L_c-1} C_i[q]g(t-nT-qT_c-\tau_i+t')g(t')dt' + z(t) \tag{3.22}$$

where $z(t)$ is the noise after filtering. Since $g(t)$ is a root raised cosine filter, $f(t)$ is defined as the raised cosine filter, thus:

$$\int_{-\infty}^{\infty} g(t-t')g(t')dt' = f(t) \tag{3.23}$$

and (3.22) can then be written as:

$$y(t) = \sum_{i=1}^{N} e^{-j\omega\tau_i} \sum_{n=0}^{\infty} A_i[n] \sum_{q=0}^{L_c-1} C_i[q]f(t-nT-qT_c-\tau_i) + z(t) \tag{3.24}$$

$y(t)$ is then periodically sampled every lT_c:

$$y[lT_c] = \sum_{i=1}^{N} \cos(\omega\tau_i) \sum_{n=0}^{\infty} A_i[n] \sum_{q=0}^{Lc-1} C_i[q]f([l-q]T_c-nT-\tau_i) + z(lT_c) \tag{3.25}$$

where only the real part of $y(t)$ has been conserved as a first approach (amplitude modulation only with A_i assumed to be real) and $z(lT_c)$ is the corresponding sampled noise.

The periodically sampled matched filter output $y[lT_c]$ is then correlated with the

synchronised versions of the spreading codes generated at the receiver for despreading via an N-branch correlator. The known code sequences embedded in the incoming signal and those generated at the receiver are used as the reference signals in order to acquire the correct phase of the codes used to encode the signal at the transmitter [144]. Notably, in SDF all the synchronization is carried out relative to a pre-defined reference dimension. A set of candidate phase value hypothesis, $\tilde{\Delta}$, of the receiver generated de-spread codes are evaluated as, $\mathrm{P}(\tilde{\Delta}|y(lT_c))$, and the case when $\hat{\Delta} = \tilde{\Delta}$, where $\mathrm{P}(\tilde{\Delta}|y(lT_c))$ is maximum is chosen as the correct phase estimate. This is expressed as:

$$\mathrm{P}(\tilde{\Delta}|y(lT_c)) = \left| FT\left\{ \mathrm{Corr}\left(C_{ref}[q-\tilde{\Delta}], y(lT_c)\right) \right\} \right| \tag{3.26}$$

P is the power spectral density (PSD), FT stands for Fourier transform, and $C_{ref}[q]$ is the despread sequence generated at the receiver and corresponding to the reference dimension. This process can be visualized as an energy detector at the despreader output that measures the signal energy in a narrow bandwidth at a known frequency. In case the hypothesized phase matches the sequence in the received signal, the wide-band spread spectrum signal will be despread correctly to give a narrow band data signal. In this case, the receiver determines that phase synchronization has been attained. Conversely, if the hypothesized phase does not match the received signal, the de-spreader will give a wide band output and the Band Pass Filter will only be able to collect a small portion of the power of the de-spread signal. Based on this, the receiver decides this hypothesized phase is incorrect and other phases will be attempted. The temporal position in which code sequences are in-phase can then be expressed as

$$\hat{\Delta} = \mathrm{argmax}\ \mathrm{P}(\tilde{\Delta}|y(lT_c)) \tag{3.27}$$

The remaining out-of-phase positions between codes correspond to non-synchronized state. This approach capitalizes on the fact that the Fourier transform of an autocorrelation function outputs a power spectral density (PSD) function. The phase shift corresponding to the synchronization state is subsequently equally applied to all the family members of the receiver generated de-spread codes.

Assuming the clock recovery is also performed using the first branch, and remembering that r/c is the propagation delay between the first antenna and the receiver, and $\tau_i \approx r/c + \Delta\tau_i$, where $\Delta\tau_i = (i-1)\Delta\tau$ (and $\Delta\tau = b/c\sin\theta$) is the differential propagation delays with respect the the reference synchronization path, the despreading process outputs the estimates of the mth symbol space coefficients, $\hat{S}_j[m]$, given as:

$$\begin{aligned}\hat{S}_j[m] = \frac{1}{L_c}\sum_{i=1}^{N}\cos\left(\omega\left(i-1\right)\Delta\tau\right)\sum_{n=0}^{\infty}\Bigg\{A_i[n] \\ \sum_{l=mL_c}^{(m+1)L_c-1}\sum_{q=0}^{L_c-1}C_i[q]C_j[l-mL_c+\lfloor\Delta^i_{init}(\theta)-\hat{\Delta}(\theta)\rfloor]f(\psi)\Bigg\} \\ + z_j[m]\end{aligned} \tag{3.28}$$

where $\psi = (l-q)T_c - nT - (i-1)\Delta\tau$, $z_j[n]$ is the noise after despreading by the code $\mathbf{C_j}$, and $\lfloor x \rfloor$ is the floor function that outputs the greatest integer less than or

equal to x. $\hat{\Delta}$ is the code's delay estimated by the synchronizer and should ideally be equal to Δ_{init}^{ref}, where $ref = 1$ is the reference dimension, here the first one. Δ_{init}^{i} is the delay between the codes $\mathbf{C_i}$ generated at the receiver and each code $\mathbf{C_i}$ embedded in the composite signal that has undergone a propagation delay of τ_i. For the first dimension, and for a perfect synchronizer operation, SDF leads to $\lfloor \Delta_{init}^{1}(\theta) - \hat{\Delta}(\theta) \rfloor = 0 \; \forall \, \theta$, since this first dimension is taken as reference. However, $\forall i \neq 1$, the quantity $\lfloor \Delta_{init}^{i}(\theta) - \hat{\Delta}(\theta) \rfloor$ may be greater than 0 if $\Delta\tau_i \geq T_c$, which may occur for some values of θ if T_c is sufficiently small (wideband scenario), or b or N sufficiently large.

Equation (3.28) can be decomposed as follows:

$$\begin{aligned}
\hat{S}_j[m] = \frac{1}{L_c} \cos\left(\omega\,(j-1)\,\Delta\tau\right) \sum_{n=0}^{\infty} \Bigg\{ & A_j[n] \\
& \sum_{l=mL_c}^{(m+1)L_c-1} \sum_{q=0}^{L_c-1} C_j[q] C_j[l - mL_c + \lfloor \Delta_{init}^{i}(\theta) - \hat{\Delta}(\theta) \rfloor] f(\psi) \Bigg\} \\
+ \frac{1}{L_c} \sum_{\substack{i=1 \\ i \neq j}}^{N} \cos\left(\omega\,(i-1)\,\Delta\tau\right) \sum_{n=0}^{\infty} \Bigg\{ & A_i[n] \\
& \sum_{l=mL_c}^{(m+1)L_c-1} \sum_{q=0}^{L_c-1} C_i[q] C_j[l - mL_c + \lfloor \Delta_{init}^{i}(\theta) - \hat{\Delta}(\theta) \rfloor] f(\psi) \Bigg\} \\
+ z_j[m] &
\end{aligned} \tag{3.29}$$

The two first lines in (3.29) represent the projection of the jth dimension of the received symbol stream onto the jth dimension of the receiver's symbol space. The two last lines represent the projection of all other dimensions of the received symbol stream onto the jth dimension of the receiver's symbol space. In order to correctly estimate $A_j[n]$, these two last lines should vanish.

Rearranging the two first lines in (3.29) and recognizing that $T = L_c T_c$, one obtain:

$$\begin{aligned}
\hat{S}_j[m] = \frac{1}{L_c} \cos\left(\omega\,(j-1)\,\Delta\tau\right) \sum_{n=0}^{\infty} A_j[n] \Bigg\{ & \\
& \sum_{\substack{q=0 \\ l=q+mL_c}}^{L_c-1} C_j[q] C_j[q + \lfloor \Delta_{init}^{i}(\theta) - \hat{\Delta}(\theta) \rfloor] f([m-n]L_c T_c - \omega\,(j-1)\,\Delta\tau) \\
+ & \sum_{\substack{l=mL_c \\ l \neq q+mL_c}}^{(m+1)L_c-1} \sum_{q=0}^{L_c-1} C_j[q] C_j[l - mL_c + \lfloor \Delta_{init}^{i}(\theta) - \hat{\Delta}(\theta) \rfloor] f(\psi) \Bigg\} \\
+ \frac{1}{L_c} \sum_{\substack{i=1 \\ i \neq j}}^{N} \cos\left(\omega\,(i-1)\,\Delta\tau\right) \sum_{n=0}^{\infty} \Bigg\{ & A_i[n] \\
& \sum_{l=mL_c}^{(m+1)L_c-1} \sum_{q=0}^{L_c-1} C_i[q] C_j[l - mL_c + \lfloor \Delta_{init}^{i}(\theta) - \hat{\Delta}(\theta) \rfloor] f(\psi) \Bigg\} \\
+ z_j[m] &
\end{aligned} \tag{3.30}$$

Finally, remembering that the function $f(t)$ is even, one can extract the mth term from the first summation in (3.30) to obtain:

$$\begin{aligned}
\hat{S}_j[m] = \frac{1}{L_c}\cos\left(\omega\left(j-1\right)\Delta\tau\right)A_j[m]\Bigg\{ & \\
& \sum_{\substack{q=0 \\ l=q+mL_c}}^{L_c-1} C_j[q]C_j[q+\lfloor\Delta^i_{init}(\theta)-\hat{\Delta}(\theta)\rfloor]f(\omega\left(j-1\right)\Delta\tau) \\
& + \sum_{\substack{l=mL_c \\ l\neq q+mL_c}}^{(m+1)L_c-1}\sum_{q=0}^{L_c-1} C_j[q]C_j[l-mL_c+\lfloor\Delta^i_{init}(\theta)-\hat{\Delta}(\theta)\rfloor]f(\psi)\Bigg\} \\
& + \frac{1}{L_c}\cos\left(\omega\left(j-1\right)\Delta\tau\right)\sum_{\substack{n=0 \\ n\neq m}}^{\infty}A_j[n]\Bigg\{ \\
& \sum_{\substack{q=0 \\ l=q+mL_c}}^{L_c-1} C_j[q]C_j[q+\lfloor\Delta^i_{init}(\theta)-\hat{\Delta}(\theta)\rfloor]f([m-n]L_cT_c-\omega\left(j-1\right)\Delta\tau) \\
& + \sum_{\substack{l=mL_c \\ l\neq q+mL_c}}^{(m+1)L_c-1}\sum_{q=0}^{L_c-1} C_j[q]C_j[l-mL_c+\lfloor\Delta^i_{init}(\theta)-\hat{\Delta}(\theta)\rfloor]f(\psi)\Bigg\} \\
& + \frac{1}{L_c}\sum_{\substack{i=1 \\ i\neq j}}^{N}\cos\left(\omega\left(i-1\right)\Delta\tau\right)\sum_{n=0}^{\infty}\Bigg\{A_i[n] \\
& \sum_{l=mL_c}^{(m+1)L_c-1}\sum_{q=0}^{L_c-1} C_i[q]C_j[l-mL_c+\lfloor\Delta^i_{init}(\theta)-\hat{\Delta}(\theta)\rfloor]f(\psi)\Bigg\} \\
& + z_j[m]
\end{aligned} \tag{3.31}$$

where the third and sixth lines in (3.31) when $l \neq q + mL_c$ can be neglected since the function $f(t)$ decays rapidly. The fifth and the sixth lines in (3.31) represents the intersymbol interference within the dimension j. This fifth line can also be neglected when considering $f(t)$ fast decay.

Applying the same simplifications on the two last terms of (3.31) leads to:

$$\begin{aligned}
\hat{S}_j[m] = & \frac{1}{L_c}\cos\left(\omega\left(j-1\right)\Delta\tau\right)A_j[m] \\
& \sum_{\substack{q=0 \\ l=q+mL_c}}^{L_c-1} C_j[q]C_j[q+\lfloor\Delta^i_{init}(\theta)-\hat{\Delta}(\theta)\rfloor]f(\omega\left(j-1\right)\Delta\tau) \\
& + \frac{1}{L_c}\sum_{\substack{i=1 \\ i\neq j}}^{N}\cos\left(\omega\left(i-1\right)\Delta\tau\right)A_i[m] \\
& \sum_{\substack{q=0 \\ l=q+mL_c}}^{L_c-1} C_i[q]C_j[l-mL_c+\lfloor\Delta^i_{init}(\theta)-\hat{\Delta}(\theta)\rfloor]f(\omega\left(j-1\right)\Delta\tau) \\
& + z_j[m]
\end{aligned} \tag{3.32}$$

The two first lines involving an auto-correlation do represent the actual dimension j being projected on the jth dimension of the receiver's symbol space. The two next lines involving a cross-correlation term, represent the other dimensions of the incoming stream that possibly leak onto the jth dimension of the receiver's symbol space.

The result of these auto- and cross-correlation terms naturally depends on the delay $\lfloor \Delta^i_{init}(\theta) - \hat{\Delta}(\theta) \rfloor$ and the nature of the code used (i.e., whether it is sensitive or not to a delay as explained in section 3.4.2). However, in order to obtain more physical insights regarding SDF operation, let us assume $Tc \ll (N-1)\,\Delta\tau$. This is a reasonable assumption and corresponds to a narrowband scenario with a not-extremely large antenna array. In this case, and assuming the synchronizer performs perfectly, that is $\hat{\Delta} = \Delta^{ref}_{init}$, the quantity $\lfloor \Delta^i_{init}(\theta) - \Delta_{init} ref(\theta) \rfloor$ is equal to 0 for all dimensions. Remembering auto-correlation and cross-correlation properties of the codes as explained in section 3.4.2, equation (3.32) simplifies to:

$$\hat{S}_j[m] = A_j[m] \cos\left(\omega\,(j-1)\,\Delta\tau\right) f(\omega\,(j-1)\,\Delta\tau) + z_j[m] \tag{3.33}$$

Apart form the noise, the correct estimation of the coefficient $A_j[m]$ is modified by two factors. The first one, i.e., $\cos\left(\omega\,(j-1)\,\Delta\tau\right)$, is due to the carrier pahse rotation and the second one, i.e., $f(\omega\,(j-1)\,\Delta\tau)$ is due to the pulse shape. In the broadside direction, $\Delta\tau = 0$, and therefore:

$$\hat{S}_j[m] = A_j[m] \qquad \forall j \tag{3.34}$$

and the transmitted symbol is therefore well recovered at the receiver.

For other θ directions, $\tau \neq 0$, and therefore, only the symbol projection on the reference dimension, i.e., $j = 1$, will be correctly retrieved: $\hat{S}_1[m] = A_1[m]$ dimensions. The other coefficients are modified by a factor that depends on τ, hence on θ, and the correct symbol estimation may fail. This is the basis of the data focusing effect that is targeted in this thesis. It is to be noted that if the system is not narrowband, auto- and cross-correlation terms may be not negligible and can contribute to the SDF effect to some extent.

3.4.5 Simulations

In order to validate both the analytical and symbolic realizations of DSSS-SDF discussed in the previous sections, simulations are implemented on Matlab™ software. The goal here is to: Validate the analytical and symbolic realizations (proof of concept); Find out the mechanism(s) that are responsible for the directional behaviour of the data transmission, i.e., the BER is angle-dependent; Compare the DSSS-SDF approach with classical (true time delay) beamforming techniques; Finally draw conclusions based on results attained.

Simulations Specifications

Unless otherwise stated, the default specification for all the simulations in this part shall be as follows: A 4x1 MISO transceiver scheme operates over a free space LOS channel environment; The broadside of the antenna array is set as the predefined position; SNR = 13 dB; The acceptable uncoded BER threshold is set at 10^{-3}; Bandwidth = 200 MHz; Inter-element distance, $b = 0.8\lambda$; For all cases orthogonal Gold

codes are used; The pulse shaping is carried out using root raised cosine filter with a roll-off factor set to 0.22.

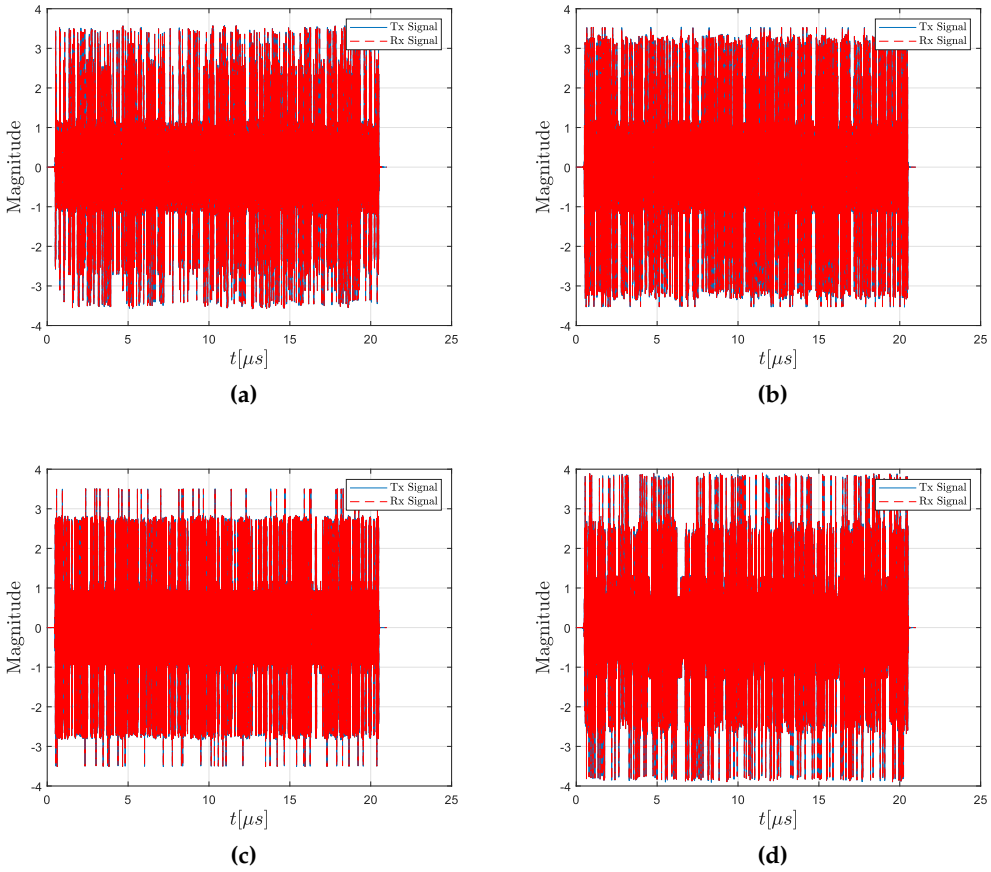

Figure 3.17: TX waveforms before spreading and RX waveforms after despreading when RX is at broadside ($\theta = 0°$)
(a) 1^{st} dimension, (b) 2^{nd} dimension, (c) 3^{rd} dimension, (d) 4^{th} dimension

Rx-Tx signal phase difference measurements

The ideal scheme covered in this section assumes perfectly synchronized scenario. As was earlier described, the SDF effect is due to a mismatch in propagation delay (phase mismatch at the receiver) of the signals corresponding to the various dimensions in the given SDF scheme. The time domain waveforms are first observed. TX waveforms before spreading and RX waveforms after despreading are shown in Figs. 3.17 and 3.18 when the receiver is located at the broadside (pre-defined location) and when it is displaced in an angular orientation 5° away from the predefined location respectively. In Fig. 3.17, the receiver is at broadside and it is observed that the received signals corresponding to all the dimensions, TX and RX waveforms are almost identical. For Fig. 3.18 on the other hand, it is evident that whereas the plot representing the first dimension, used as a reference, did not experienced any significant phase change, the subsequent ones did indeed exhibit considerable phase shift relative to the transmitted signal. The actual phase difference values are given in Table 3.1, from this we see that at broadside the corresponding phase differences are

approximately zero. On the the other hand, when the receiver shifts to the unwanted location, it is noted that the phase differences vary for all the dimensions.

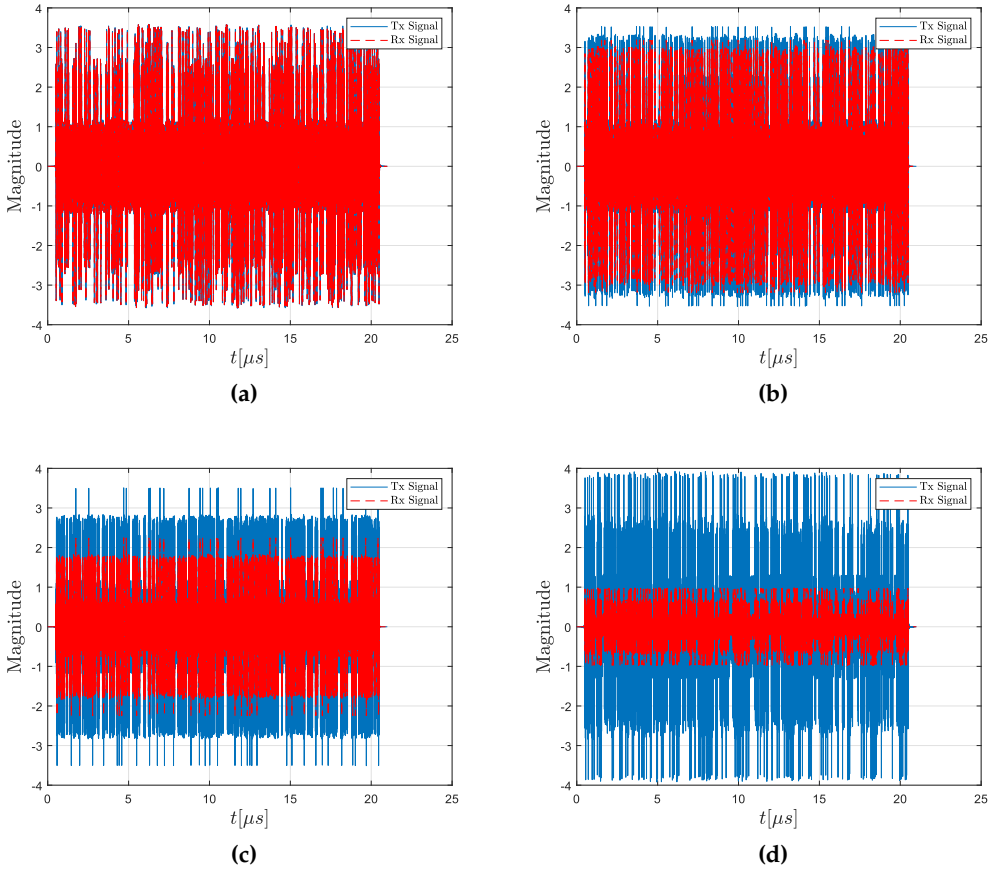

Figure 3.18: TX waveforms before spreading and RX waveforms after despreading when RX is at $\theta = 5°$
(a) 1^{st} dimension, (b) 2^{nd} dimension, (c) 3^{rd} dimension, (d) 4^{th} dimension

RX. angular displacement	Dimension	Phase Diff. (Rx $->$ Tx)[Deg]
0°	1	0°
	2	0.00395°
	3	0.00636°
	4	0°
5°	1	0°
	2	1.492°
	3	4.820°
	4	6.247°

Table 3.1: Table showing phase Rx and corresponding Tx signal phase differences for various Rx positions.

Mechanism responsible for the directional behaviour of the data transmission

In the analytical derivation resulting in equation (3.33), it is noted that two components $\cos(\omega\Delta\tau_i)$ and $f(\Delta\tau_i)$ are responsible for the realized spatial selectivity. The

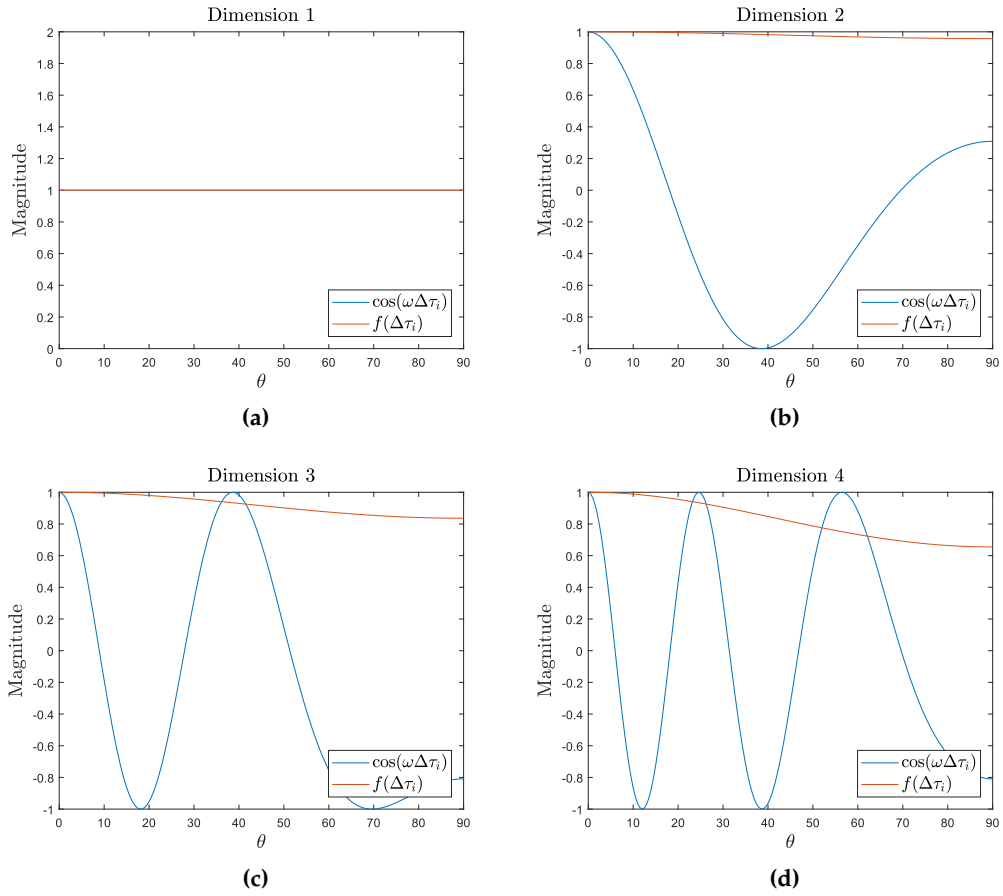

Figure 3.19: Plots showing the extent of contribution of the $\cos(\omega\Delta\tau_i)$ and $f(\Delta\tau_i)$ to the SDF effect

simulation in this section seeks to answer the question of, to what extent does each of the above identified components impact on selectivity. To do so the evolution of these terms with respect to changing receiver positions (θ°) are plotted in Fig. 3.19, in a scheme where synchronization is implemented with reference to the first dimension and $\Delta\tau_i$ is calculated for all dimensions from the equation earlier given, i.e., $\Delta\tau_i = \tau_i - \tau_{ref}$. It is thus evident that for the first dimension where $\Delta\tau_i = \tau_{ref}$, $\Delta\tau_i = 0$, and the two functions will always return a peak of 1 as shown in Fig. 3.19a, in this case they will have no effect on the resultant estimates and (3.33) will return the exact estimates of the transmitted symbols. Observing the two terms in the other dimensions where $\Delta\tau_i \neq \tau_{ref}$, it is seen that both the functions start to return diminishing magnitudes, evidently steeper for the $\cos(\omega\Delta\tau_i)$ and less so for $f(\Delta\tau_i)$ as is respectively shown by the blue and red curves of Figs. 3.19b to 3.19d. It is important to emphasize here that in SDF, all the estimated values corresponding to the different dimensions must be correctly estimated so as to be able to recover the original transmitted data. It is also evident from these plots that the larger the number of elements in the array the better the selectivity as shown by the increasing steepness of the slope further away from the reference dimension.

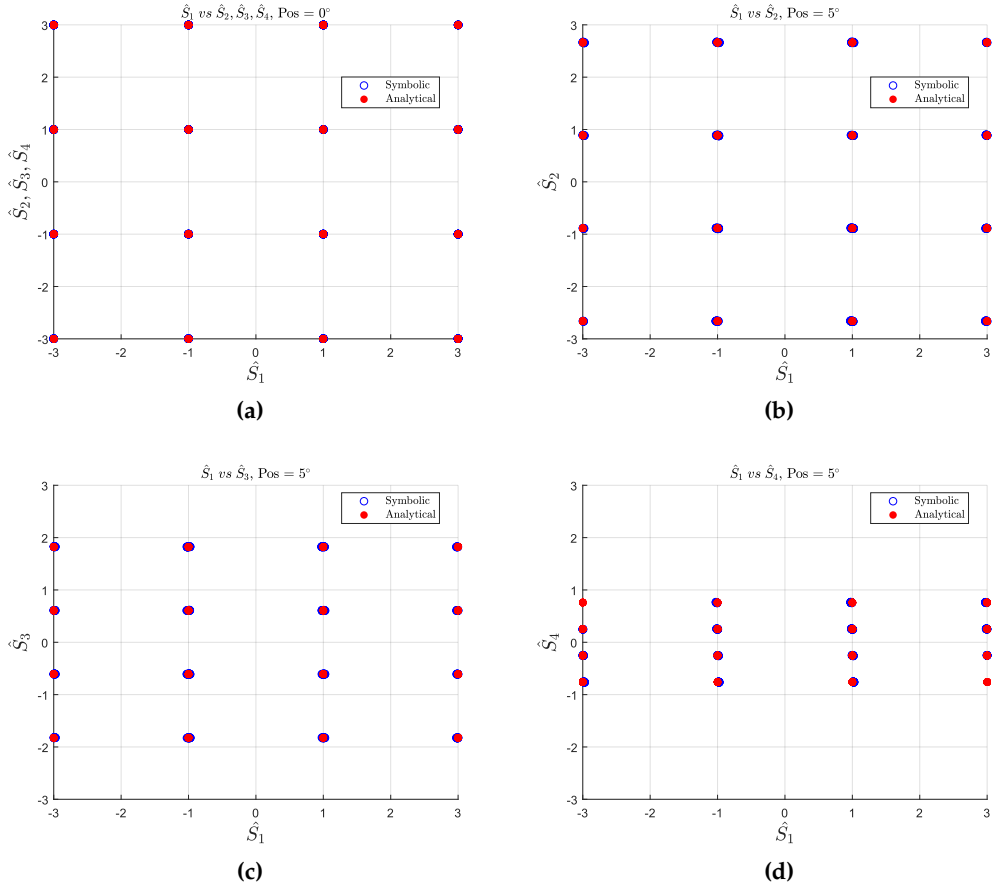

Figure 3.20: Scatter plots demonstrating the convergence of the symbolic and analytical SS-SDF realizations

Validation of the symbolic and analytical DSSS-SDF realizations

In this section, the proof of concept is validated by comparing constellation results obtained analytically with (3.33) and with numerical simulations. This is demonstrated in the scatter plots in Fig. 3.20. Specifically, Fig. 3.20a visualizes the constellation when the receiver is at broadside, in this case for S_1 against all the other dimensions, i.e., $S_2, S_3,$ and S_4. Figs. 3.20b to 3.20d on the other hand show the constellation when the receiver is displaced by 5°. For both the analytic and numerical results, we see an increasing reduction in magnitude of the non-reference dimension with an increase in inter-element distance in the antenna array relative to the reference element. This jeopardizes correctly estimating the symbols at RX for this direction.

Validation of Spatial Selectivity: A comparison of SDF with classical beamforming

SDF has been proposed as a candidate alternative to classical beamforming schemes in wireless geocasting applications. The simulations in this section compare the performance of the two approaches in terms of attainable spatial selectivity. For fair comparison, spread spectrum modulation is applied to both schemes, and comparisons implemented for various code lengths and SNR. Fig. 3.21 illustrates the TX beamforming scheme used for comparison, the receiver architecture being the same

for both schemes. The simulations assume an ideal scenario, as such, channel esti-

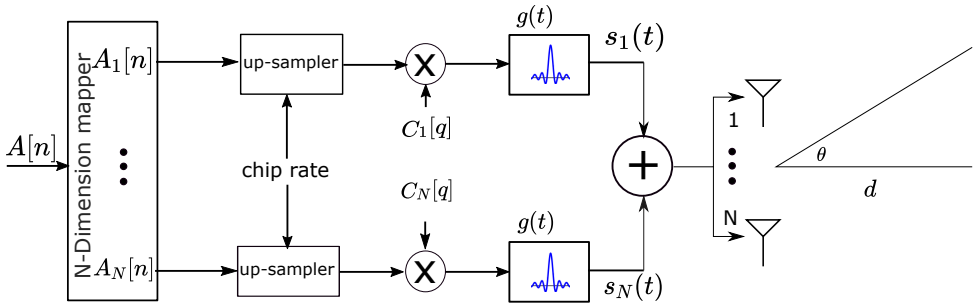

Figure 3.21: Schematic of the beamforming scheme used

mation and equalization have not been implemented here. Recall that in SDF, the beamwidth is defined as the region within which data can be decoded and not the classical half power beamwidth used in power focusing techniques. An arbitrary threshold of BER= 10^{-3} is considered to evaluate beamwidths. For fair comparison, the constellation powers are normalized to ensure that signal power does not change with the modulation scheme.

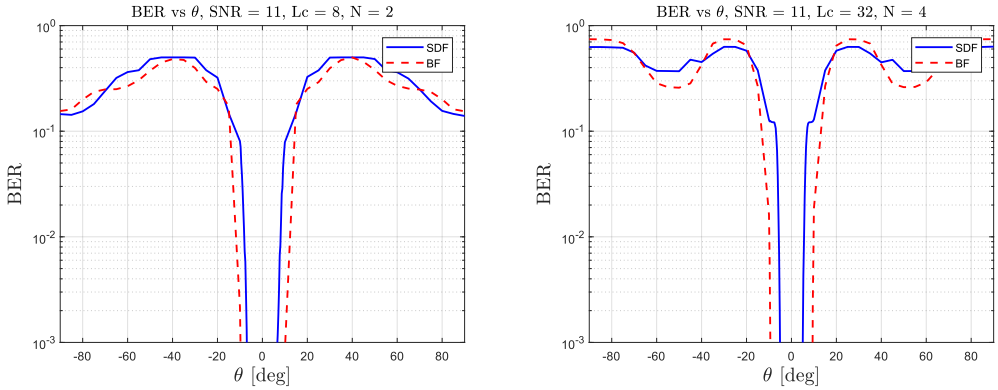

(a) **(b)**

Figure 3.22: Evolution of BER with changing angular position of the receiver

Fig. 3.22 illustrates a plot of BER vs. angular orientation of the receiver for the SDF (solid) and BF (dashed) for two different implementations. In both cases, SNR is set to 11. In the case of Fig. 3.22a, the number of antenna elements is set to 2 and code length set to 8 chips. It is observed that SDF attains better spatial selectivity at 13° than BF at 21°. In Fig. 3.22b on the other hand, the code length is set to 32 chips and number of antennas set to 4. In this case also, it is observed that SDF attains better spatial selectivity at a beamwidth of 10° against 18.8° for the equivalent beamfoming scheme. In other words, for both cases, SDF exhibits s slightly below 50% better spatial selectivity in this this ideal scenarios. This is thus evidence of the spatial selectivity ability of the proposed SDF scheme.

Influence of spreading sequences on the robustness of the scheme

In theory it is expected that the longer the length of the spreading sequencing the greater the impact it has on effective SNR at the receiver. In other words, with longer despreading codes, the despreading process does significantly reduce the noise at

the receiver thus improving the overall performance of this scheme. This is shown in the plots of Fig. 3.23, where it is observed that with a SNR of 7 dB, the SDF scheme does not attain the set BER threshold of 10^{-3}, however with an increase in code length for the same SNR the threshold is attained.

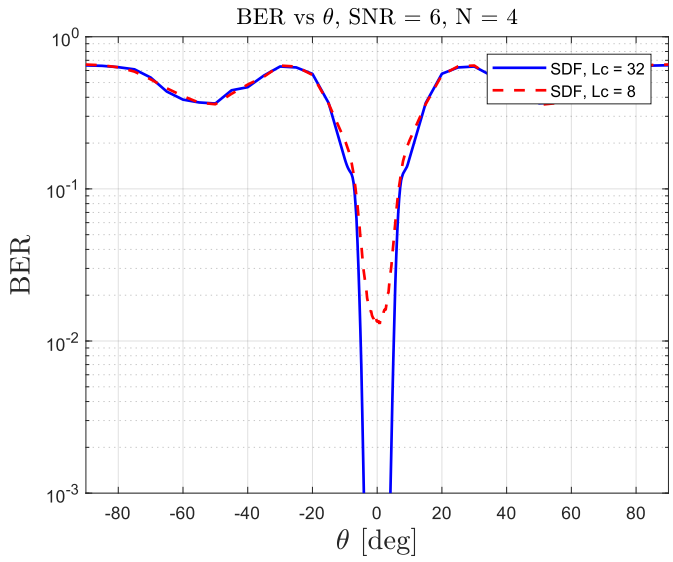

Figure 3.23: Effect of code on improving SS-SDF robustness

3.4.6 Remarks

This section discussed an ideal case of the proposed spread spectrum-based spatial data focusing technique. Simulations that demonstrate the proof of concept have been implemented in Matlab. A comparison between the proposed DSSS-SDF and classical beamforming i.e., delay and sum beamforming, is carried out. The result shows that SDF attains better spatial selectivity than classical beamfoming schemes. It is also shown that, for a pure LOS based scheme, spreading sequences significantly improve the overall performance of the by increasing the effective SNR at the receiver.

3.5 DSSS-based SDF with IQ resources in LOS

The previous section reviewed DSSS-SDF assuming perfect synchronized implementation, an ideal scenario that may not apply in practical cases. To investigate more practical cases, this section proposes the implementation of DSSS-SDF with an added degree of freedom, the IQ domain, DSSS-SDF-IQ. The introduction of quadrature components in the scheme enables efficient channel estimation and equalization at the receiver, resulting in more practical outcomes, which have also a strong influence on the SDF spatial selectivity.

3.5.1 Principal of IQSS-SDF

It was earlier outlined that in SDF, the symbols to be transmitted are mapped onto an N-dimension orthogonal symbol space prior to being separately transmitted as uncorrelated data streams over unique channels. In DSSS-SDF-IQ, the underlying orthogonal basis is realized by simultaneously exploiting orthogonal Gold codes

and quadrature components. Fig. 3.24 illustrates the architecture of the proposed

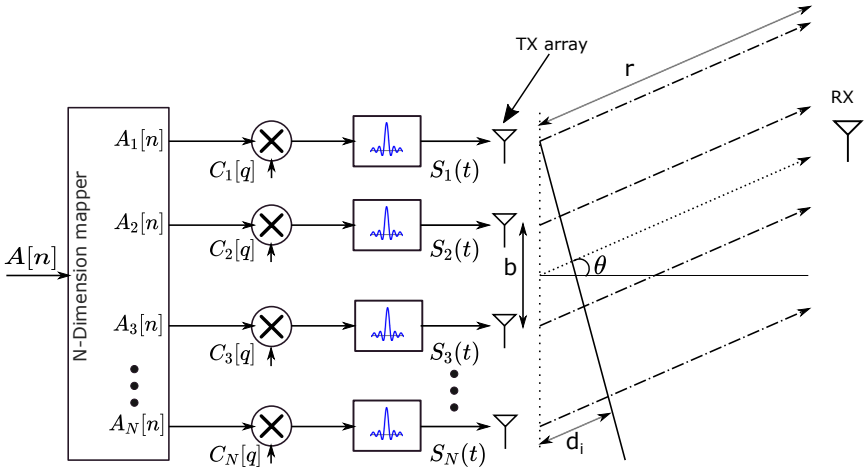

Figure 3.24: DSSS-SDF-IQ architecture

scheme. The incoming discrete symbols stream $A[n]$ is mapped onto a $2N$-dimension complex symbol space as $A_i[n] = A_{i,I}[n] + jA_{i,Q}[n]$. The complex coefficients $A_i[n]$ are then spread by unique members of the N-dimensional orthogonal Gold codes set, $\mathbf{C}_1[q], \mathbf{C}_2[q], ..., \mathbf{C}_N[q]$. The outputs of the spreading process, $A_i[n]\mathbf{C}_i$, are subsequently shaped using root raised cosine filters $g(t)$. The filter outputs $S_i(t)$ then feed into unique elements of an N-element antenna array, in essence, the antenna array elements transmit N uncorrelated/orthogonal complex signals which can be expressed as:

$$S_i(t) = \sum_{n=0}^{\infty} A_i[n] \sum_{q=0}^{L_c-1} C_i[q] g(t - nT - qT_c) \tag{3.35}$$

where T, L_c, and T_c are symbol duration, code length and chip duration respectively.

3.5.2 Matched filter based receiver

For the initial proof of concept, a Multiple Input Single Output (MISO) LOS channel model as illustrated in Fig. 3.24 is considered. The same assumptions than in section 3.4.3 are considered. The channel output, i.e., the received signal $r(t)$ is thus the summation of the convolution of the signals transmitted over the ith channel and their respective impulse responses:

$$r(t) = \sum_{i=1}^{N} S_i(t - \tau_i) e^{-j\omega\tau_i} + n(t) \tag{3.36}$$

where $n(t)$ is AWGN at the receiver.

The scheme implements a matched filter based receiver whose architecture is depicted in Fig 3.16, it features, the matched filter, sampling, synchronization and equalization, a code generator, parallel correlators, IQ demodulator, and the detection/decision blocks. $r(t)$ feeds into the matched filter whose output is thus expressed as $y(t) = r(t) * g^*(-t)$, $g(t)$ is a symmetrical function thus $g(t) = g^*(-t)$. Also, $g(t)$ is a root raised cosine filter, thus $g(t) * g^*(-t) = f(t)$, which is a raised

cosine filter. Considering this, the matched filter output can thus be expressed as:

$$y(t) = \sum_{n=0}^{\infty} \sum_{i=1}^{N} \left\{ A_i[n] e^{-j\omega\tau_i} \sum_{q=0}^{L_c-1} C_i[q] f(t - \tau_i - qT_c - nT) + z(t) \right\} \tag{3.37}$$

where $z(t)$ is the AWGN after filtering. (3.37) is sampled periodically every lT_c as:

$$y[lT_c] = \sum_{n=0}^{\infty} \sum_{i=1}^{N} \left\{ A_i[n] e^{-j\omega\tau_i} \sum_{q=0}^{L_c-1} C_i[q] f((l-q)T_c - \tau_i - nT) + z[lT_c] \right\} \tag{3.38}$$

where $z[lT_c]$ are noise samples.

Similarly to section 3.4.4, the despreading onto the jth code of the mth complex symbol can be expressed as:

$$\hat{S}_j[m] = \frac{1}{L_c} \sum_{i=1}^{N} e^{-j\omega\tau_i} \sum_{n=0}^{\infty} \left\{ A_i[n] \right. \tag{3.39}$$

$$\left. \sum_{l=mL_c+1}^{(m+1)L_c} \sum_{q=0}^{L_c-1} C_i[q] C_j[l - mL_c + \lfloor \Delta^i_{init}(\theta) - \hat{\Delta}(\theta) \rfloor] f(\psi) \right\}$$

$$+ z_j[m] \tag{3.40}$$

with $\psi = (l-q)T_c - nT - \tau_i$, $\tau_i = r/c + (i-1)\Delta\tau$, and $\Delta\tau = b/c \sin\theta$. Assuming a narrowband scenario where $\lfloor \Delta^i_{init}(\theta) - \hat{\Delta}(\theta) \rfloor = 0$, (3.40) can be simplified into:

$$\hat{S}_j[m] = A_j[m] e^{-j\omega\tau_j} f(\omega\,(j-1)\,\Delta\tau) + z_j[m] \tag{3.41}$$

Channel estimation and equalization

A pilot-assisted channel estimation and equalization is considered. In SDF, channel estimation is carried out in reference to a pre-defined reference dimension. Assuming that the incoming signal includes a known complex pilot sequence $A_{ref}[n]$ with $n = 1, ..., n_{pilot}$ where n_{pilot} is the number of symbols used in the pilot sequence. The reference channel can then be estimated using the least-square estimate averaged over the n_{pilot} pilot symbols as:

$$\hat{h}_{ref} = \frac{1}{n_{pilot}} \sum_{n=1}^{n_{pilot}} \frac{\hat{S}_{ref}[n]}{A_{ref}[n]} \tag{3.42}$$

In a LOS scenario and using the first antenna as the reference, as the noise is averaged out (when SNR and/or n_{pilot} get larger), the estimate tend to $\hat{h}_{ref} \to e^{-j\omega r/c}$.

The equalization of the received symbols is then performed using this unique estimate for all dimensions leading to:

$$\hat{S}^{EQ}_j[m] = \frac{\hat{S}_j[m]}{\hat{h}_{ref}} \approx A_j[m] e^{-j\omega(j-1)\Delta\tau} f(\omega\,(j-1)\,\Delta\tau) + z'_j[m] \tag{3.43}$$

where $z'_j[m]$ is the mth noise sample after channel equalization.

Like in the previous section, when $j = 1$, i.e., the reference antenna, the EQ symbol coefficient $\hat{S}_1^{EQ}[m]$ is a correct estimate of $A_1[m]$ if the noise is sufficiently low. When $j \neq 1$, the EQ estimate will be affected for θ directions leading to $\Delta\tau \neq 0$.

Unlike in the previous case where only an amplitude modulation was used, here, the coefficients $A_j[m]$ are complex and affected by a term $e^{-j\omega(j-1)\Delta\tau}$ of unitary magnitude which introduces a rotation in the complex plane of the coefficient $A_j[m]$. The second term $f(\omega\,(j-1)\,\Delta\tau)$ affects only the magnitude of the complex coefficient. The effect of (3.43) is illustrated in Figs. 3.25 and 3.26 where the received constellations are plotted for $L_c = 8$ and 32 respectively. The simulation specifications are: SNR set to 13 dB, $N = 2$ antenna arrays, thus a four dimension scheme with an inter-element spacing $b = 0.8\lambda$. It is observed that in both cases, at broadside, constellation patterns of the received symbol coefficients resemble that of the transmitted symbols as illustrated in Figs. 3.25a, 3.25c, 3.26a and 3.26c.

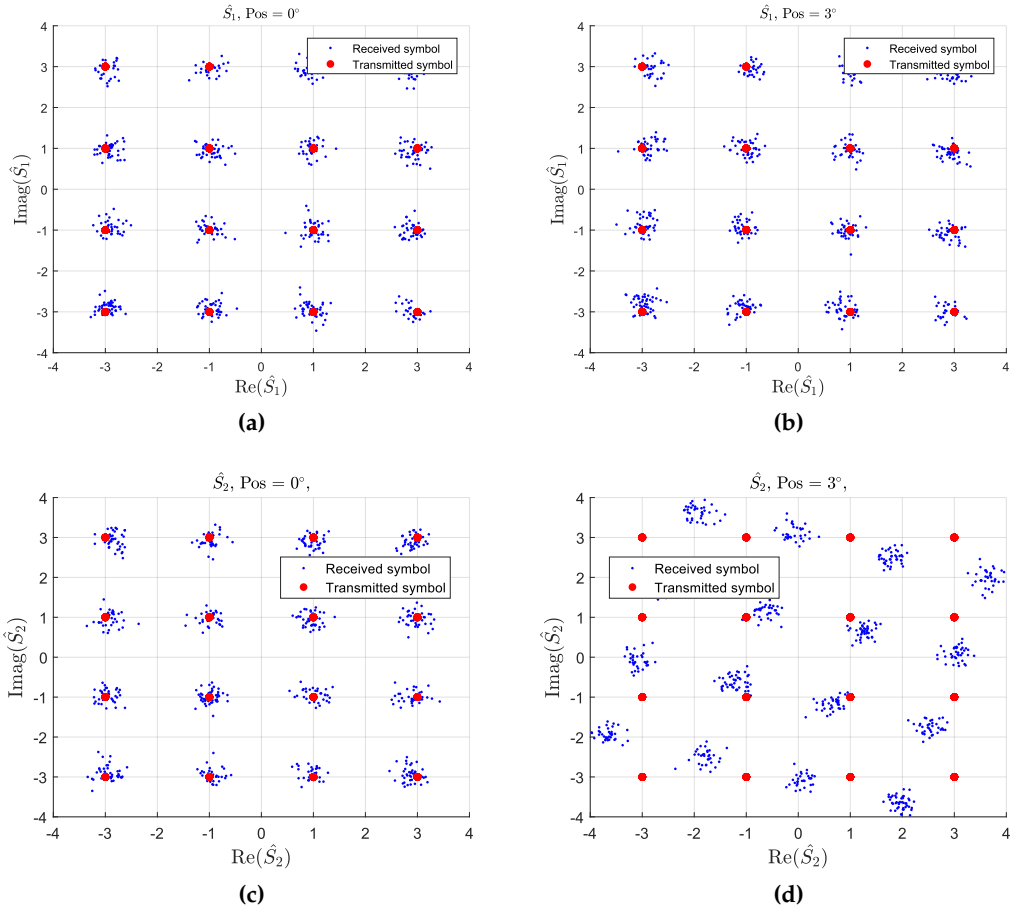

Figure 3.25: Scatter plots representing the received SDF symbol coefficients with $L_c = 8$ chips

Similarly, as the receiver displaces itself in an angular rotation away from the broadside, in this case at position 3°, the SDF effect is seen as complete distortion of symbols due to the rotated second dimension as shown in Figs. 3.25b and 3.26d . Recall that the SDF effect as earlier discussed is due to the scheme inducing increased BER in unwanted locations.

Another phenomenon that is validated by Figs. 3.25 and 3.26, is the effect of using spreading sequences with larger code lengths compared to those with shorter

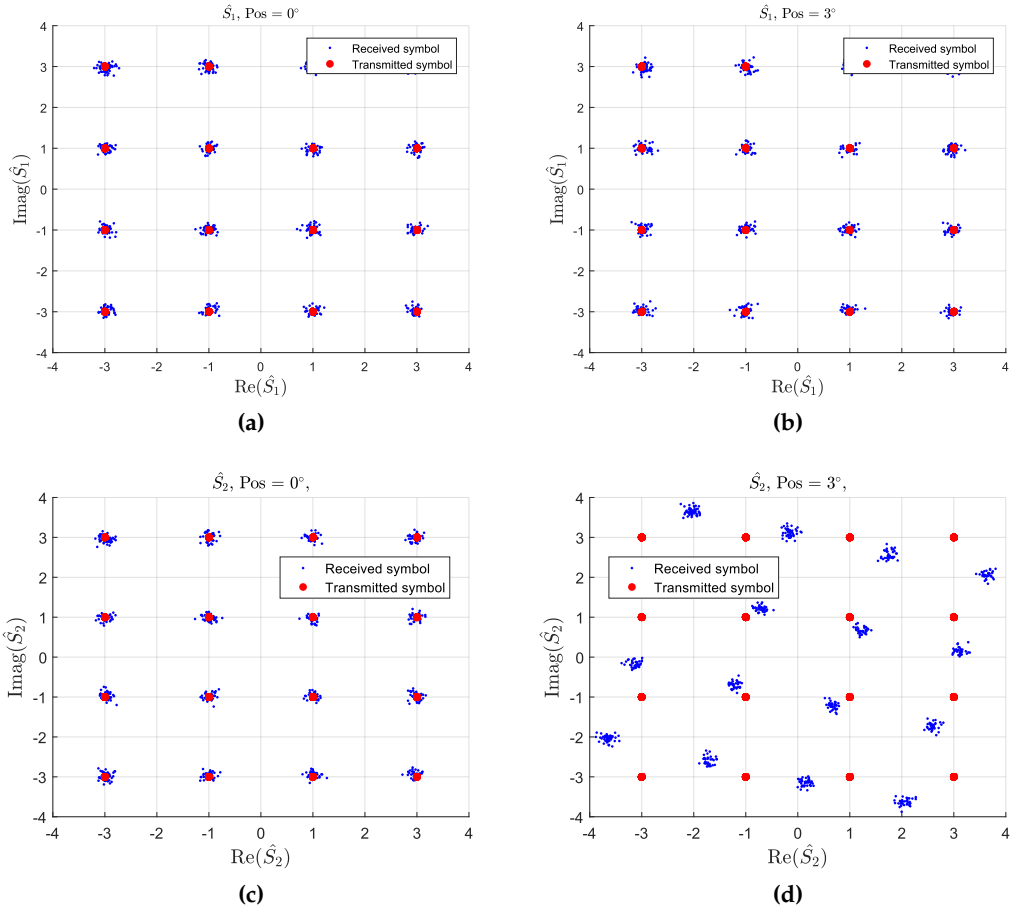

Figure 3.26: Scatter plots representing the received SDF symbol coefficients with $L_c = 32$ chips

lengths. We see actually that longer code lengths increase the effective SNR, significantly minimizing the effect of noise.

3.5.3 Simulations

Simulations are carried out to validate the discussion in the preceding section. For all the simulations orthogonal Gold spreading sequences are used. A rectangular mapping codes symbols with $k_{per\_dim} = 2$ bits per dimensions, which is similar in terms of performance with respect to noise to a classical 16-QAM scheme. For this simulations, unless otherwise stated, we shall retain orthogonal Gold code as the preferred spreading sequence, inter-element spacing $b = 0.8\lambda$, LOS transmission, roll-off factor of 0.22, carrier frequency of $1GHz$, and acceptable BER threshold of 10^{-3}. For the simulations, when L_c changes, unless stated otherwise, the overall bandwidth remain constant (i.e., no spread in frequency, T_c remains therefore constant), so the symbol rate decreases (i.e., spread in time). This approach enables studying performance with a constant chip duration T_c for different L_c. Indeed, as seen in the previous analytical derivations, when T_c gets smaller, additional terms can contribute in the estimation of the coefficients $A_i[n]$ due to non-zero cross-correlation products for instance. Having a control over T_c allows us to analyse the effect of those terms separately, and to remain in a narrow-band scenario whatever the value of L_c.

Role of Spreading sequences

We have already seen in Section 3.4.5 that the spreading codes significantly influence the effective SNR at the receiver, a similar scenario is assessed in Fig. 3.27. It shows the evolution of BER with changing receiver angular position for a 4x1 MISO scheme, SNR set to 6dB, and two code lengths $L_c = 8$ and 32, simulated for both SDF and BF. At this low SNR, it is observed that both SDF and BF do not attain the set BER threshold of 10^{-3}, however, on applying a longer length spreading sequence, they both attain the threshold. Evidently, this phenomenon is not unique to SDF, rather, it applies to all spread spectrum based communication schemes. Considering that in this plot a perfectly synchronized scenario is assumed, the result tells us that in this case, the longer code lengths actually increase the effective SNR at the receiver thanks to the despreading effect, which spreads out the noise significantly, thereby reducing its energy. With $L_c = 32$, the BER = 10^{-3} beamwidth is about 12.3° in BF and 1.3° in SDF, which shows that the proposed scheme does indeed exhibit superior angular selectivity.

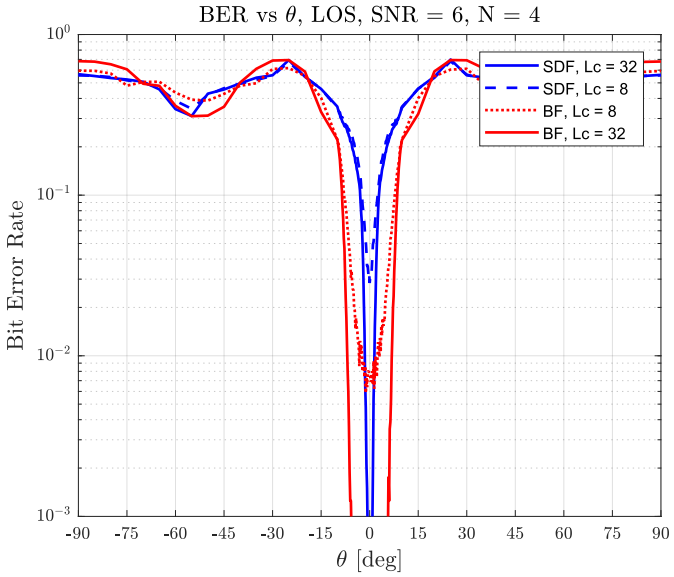

Figure 3.27: The effect of code length on SDF (in blue) and BF (in red)

Influence of the channel estimation on angular selectivity

To highlight the effect of the channel estimation and to see whether its accuracy has an influence on the performance, we compare the results with those obtained assuming a perfect channel estimation, i.e., $h_{ref} = e^{-j\omega r/c}$. The plot in Fig. 3.28a illustrates the evolution of BER vs. changing angular position of the receiver comparing the effect of channel estimation on the resultant beamwidth. The light blue solid plot represents the evolution when the number of pilots is $n_{pilots} = 16$, the navy blue dotted lines depict the case where a larger sized pilot is applied ($n_{pilots} = 512$), and finally the red dotted plot represents a case that assumes perfect channel estimation. It is observed that when $n_{pilots} = 16$, in some spurious positions within the illuminated beamwidth, the BER fluctuates a lot, especially at the edges of the beam. On the other hand, it is observed that when a large number of pilot symbols are applied, this spurious blind positions are eliminated. The plots in Fig. 3.28b show a zoomed-in version of Fig. 3.28a to better see this effect. Overall, the results based on the

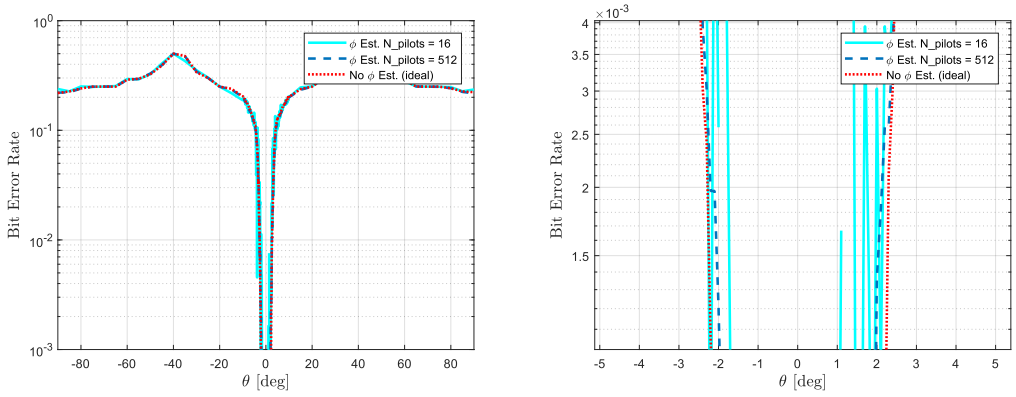

(a) **(b)**

Figure 3.28: BER vs θ with and without phase estimation: (a) With pilots $n_{pilots} = 16$ and 512, and the ideal channel estimation case; (b) Zoomed in version. When $b = 0.8\lambda$, $L_c = 8$, and SNR = 11 dB, $N = 2$

ideally-estimated and the 512-pilot-based-estimated channel exhibit beamwidths of 4.4° and 3.8° respectively.

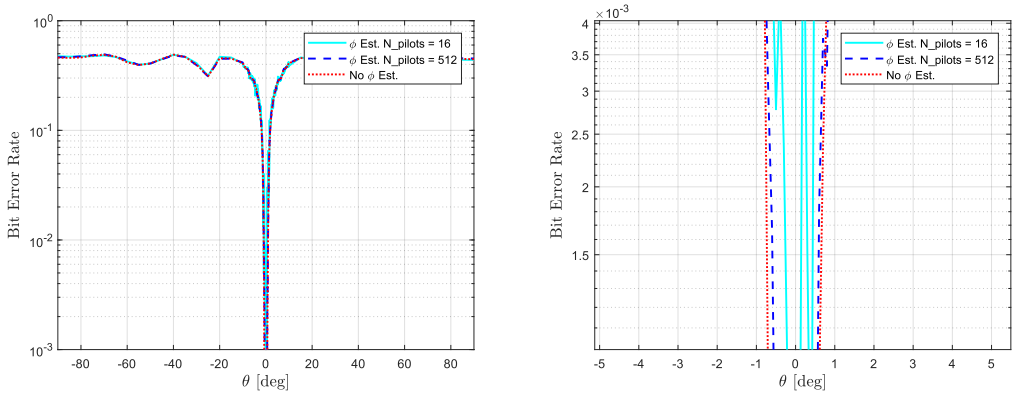

(a) **(b)**

Figure 3.29: Comparing BER vs θ with and without phase estimation for $n_{pilots} = 16$ and $n_{pilots} = 512$ and perfect channel estimation case; (a) Original plot; (b) Zoomed in plot; When $b = 0.8\lambda$, $L_c = 8$, and SNR = 11 dB, N = 4

Similar curves are plotted in Fig. 3.29 for the case of $N = 4$ antenna elements at the receiver. It is observed that, as expected of any MIMO scheme, an increment in number of elements in the transmit array results enhanced spatial selectivity as seen here where the scheme attains beamwidths of about 1.2°. Regarding the effect of phase estimation, we see that in Fig. 3.29a, where the estimation employs $n_{pilots} = 16$ pilots, it is evident that the plot experience some fuzzy effects, observed as spurious blind spots within the illuminated area, whereas with with $n_{pilots} = 512$ pilots the BER beam is much more robust. The ideal channel estimation achieve a beamwidth of approximately 1.24° whereas the case with a large number of pilots attained 1.04°.

To better understand how the channel estimation influences the robustness of the SDF beam, Fig. 3.30 illustrates the influence of pilot symbols and length of spreading sequences on the estimated phase at the receiver. In both cases SNR is set to 11 dB,

and the number of antennas to $N = 2$. Fig. 3.30a illustrates the estimated phases at the receiver with changing user angular position. Specifically for this simulation the code length was set to a constant of 32 chips and investigation carried out for cases with number of pilots set to 16 and 512 bits respectively. The solid red plots represent the case of $n_{Pilots} = 512$ and the blue solid plots represent $n_{Pilots} = 16$. It is observed that with a larger number of pilot symbols, the variance of the estimated phase reduces and converge to the ideal, i.e., 0°, in this case. However, as it is evident, despite this superior performance, the phase estimate variance is already very low and so may not significantly impact the overall spatial selectivity of the SDF scheme.

Fig. 3.30b on the other hand illustrates the estimated phase with changing angular user for different code lengths, viz, 256 and 8 chips long respectively. The longer codes phase estimates are depicted by the solid blue plots whereas the shorter codes estimates are depicted by the dashed red plots. Just like the case for larger pilot symbols, it is observed that schemes employing longer code lengths, in this case 256 exhibit near ideal phase estimations when compared to those running shorter code lengths. Indeed, the pilots are also spread like the data and therefore also benefit from a higher effective SNR as the code length increases. The above case exposes the benefit of using longer code lengths. This phenomenon may be of greater impact in the case for multipath implementation which is investigated in the next chapter.

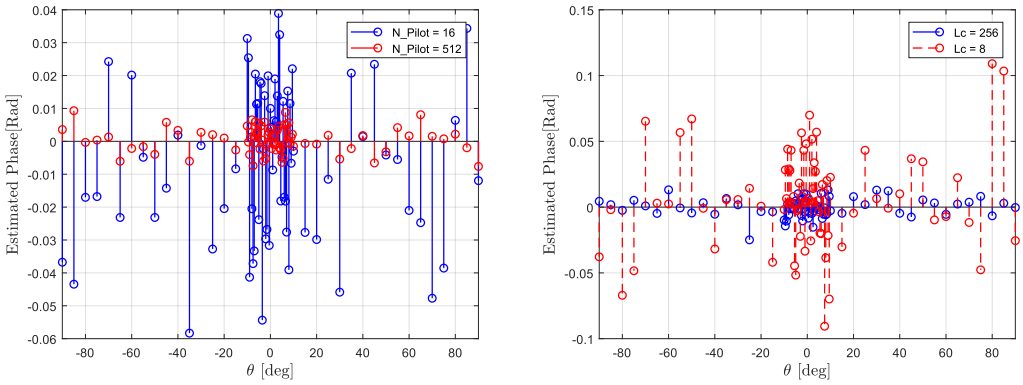

(a) **(b)**

Figure 3.30: Estimated channel phase as a function of θ. (a) Influence of number of pilot symbols, $N = 4$ (b) Influence of spreading sequence length, $N = 2$. SNR = 11 dB

Beamwidth as a function of N

Fig. 3.31 illustrates the variation of the BER$= 10^{-3}$-beamwidth with respect to number of antennas used (N), for both SDF and BF. It is observed that, and as is expected of any spatial focusing techniques, increasing the number of antenna elements in the array increases the spatial selectivity (thus narrower beams) of the corresponding scheme. As an example, with 2 antennas and $L_c = 8$, BF exhibits a beamwidth of 44° whereas SDF exhibits a beamwidth of 3.7°, clearly showing the superior behavior of SDF in terms of angular selectivity. Also, between $L_c = 8$ and $L_c = 32$, we can observe that the beamwidth widens a bit. When $N = 2$, a beamwidth widening of 43% is observed in BF and of 35% in SDF. When $N = 6$, this increase is of 37% and

25% in BF and SDF respectively. It is thus evident that, the SDF system is a bit more consistent than BF in terms of beamwidth with respect to L_c .

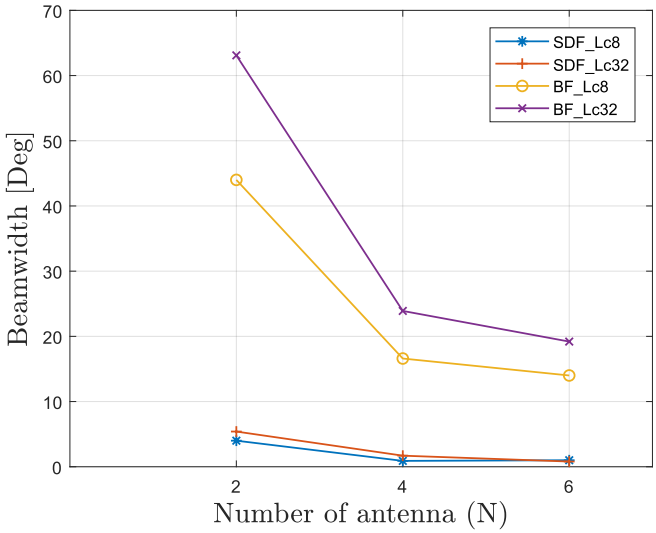

Figure 3.31: Evolution of the BER= 10^{-3}-beamwidth as a function of the number of antenna elements N when $b = 0.8\lambda$ and SNR = 11 dB

Table 3.2 shows the exact values corresponding the plots of Fig. 3.31. It clearly appears that SDF achieves beamwidths that are narrower by a factor 10 to 20 with respect to beamforming.

N	L_c	BF Beamwidth [°]	SDF Beamwidth [°]
2	8	44°	4°
	32	63.1°	5.4°
4	8	16.6°	0.9°
	32	23.9°	1.7°
6	8	14°	0.8°
	32	19.2°	1°

Table 3.2: Table showing a comparison of beamwidths for different N with respect to L_c

Effect of b (inter-element spacing)

Fig. 3.32 illustrates the effect of inter-element spacing in the tranmit antenna array. Two cases are plotted, $b = 1.5\lambda$ and $b = 0.8\lambda$ depicted by the red dashed and solid blue curves respectively. As expected wider spacing leads to improved spatial selectivity, as such, in this case the beamwidths attained are, 3.2° and 5.4° for 1.5λ and 0.8λ respectively. It is also observed that when $b = 1.5\lambda$, due to the periodicity of the exponential term in (3.40), we may experience spurious directions, i.e., unwanted directions experiencing low BER. However, the BER is not significantly low in those directions thanks to the $f(t)$ and the cross-correlation terms.

SDF operation robustness to noise

The robustness of the SDF scheme is demonstrated by the simulations illustrated in Fig. 3.33 where $N = 2$ and $L_c = 8$ (Fig. 3.33a) and $L_c = 64$ (Fig. 3.33b). It depicts

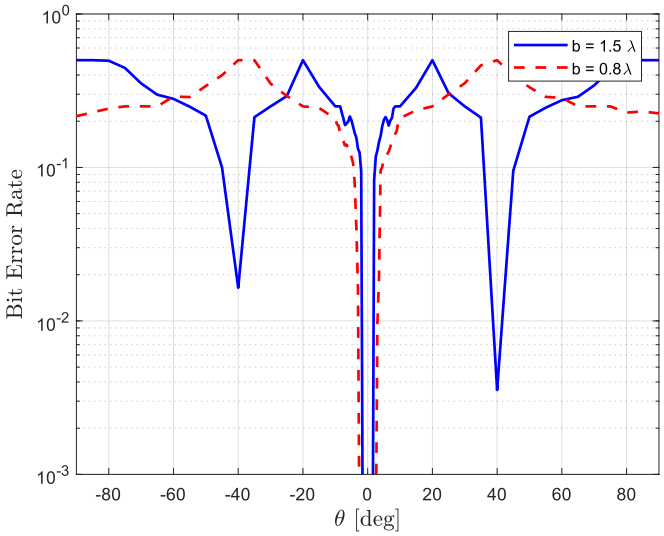

Figure 3.32: Effects of the inter-element spacing b on SDF spatial selectivity. $N = 2$, $L_c = 32$, and SNR = 11 dB

two plots each of SDF and beamforming with applied SNR of 10 and 20 dB. It is observed in such cases, that SDF exhibits greater consistency with change in SNR than beamforming schemes. Specifically, when $L_c = 8$ (Fig. 3.33a), at 10 dB, SDF and beamforming attained beamwidths of 3.2° and 36.8° respectively, whereas at 20 dB applied SNR, the two (SDF and BF) respectively attained beamwidths of 4.9° and 60.8°. Furthermore, for such SNR, the BF scheme exhibits spurious lobes and therefore, the BER is low not only in the broadside direction. Depending on the SNR, those spurious angular regions may or not attain a BER less than a certain threshold (here 10^{-3}). When L_c increases up to 64 , thereby increasing the effective SNR (Fig. 3.33b), BF achieves a beamwidth of 61.1° and 71.64°, while SDF achieves 5.5° and 6.4°, for SNR = 10 and 20 dB respectively. SDF exhibits here too more consistency in the beamwidth with respect to SNR. Furthermore, beamwidths exhibited by SDF appear to be more consistent with a change of code length.

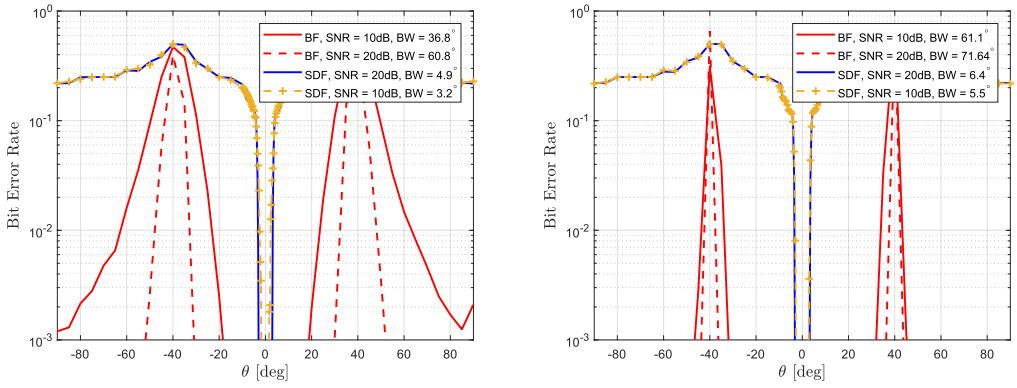

(a) Lc = 8 **(b)** Lc = 64

Figure 3.33: Robustness of SDF over BF with changing SNR and L_c, where $N = 2$

SDF Beamsteering

In previous simulations, the focus was on the main lobe array sensitivity which was fixed to the broadside. However, similarly to beamforming, it is possible to electronically steer the beam without physically moving the array. This ability in its basic form can be achieved by simply adding a delay stage to each of the array elements as shown in Fig. 3.34.

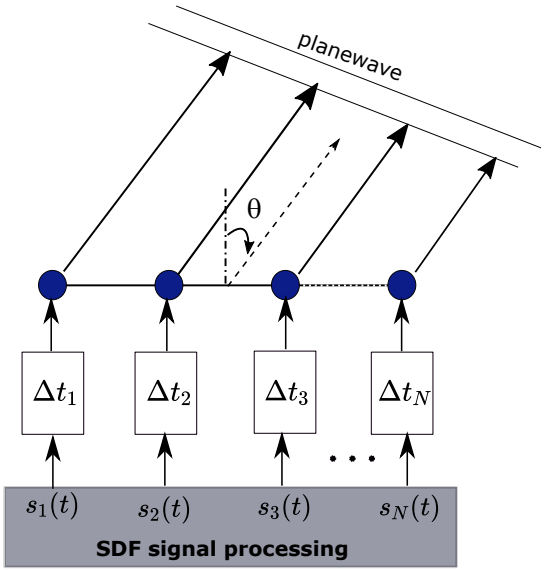

Figure 3.34: Array architecture for SDF beamstreeing

Fig. 3.35 illustrates the plots resulting from the simulation of beamsteering in the SDF implementation for selected angles $0°, -20°, -60°$ and $-80°$. The idea borrows directly from the concept of delay-and-sum beamforming, simply adding a delay to each antenna element such that the signals from a particular direction are aligned before they are summed. Controlling these variable delay lines allows us to steer the direction of the main lobe.

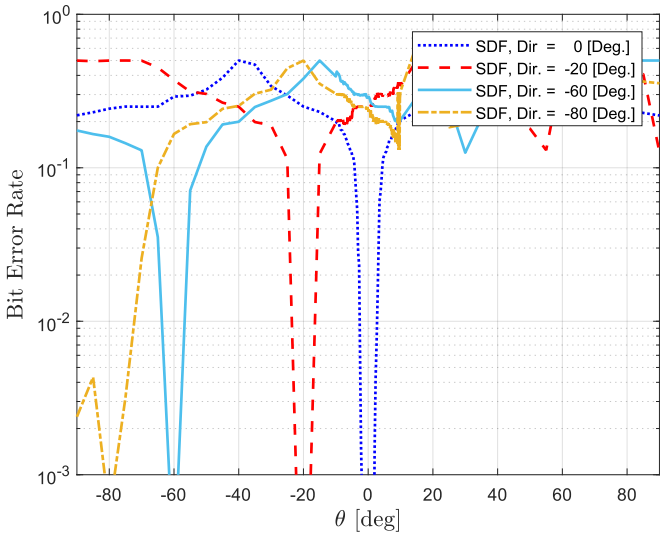

Figure 3.35: Beam steering capability of the proposed SDF scheme

3.6 Conclusion

This chapter introduced the concept of direct sequence spread spectrum based spatial data focusing. Its general framework is outlined, and analysis done in the real domain to both understand the mechanism behind the spatial selectivity ability of the proposed scheme, and for purposes of proof of concept. A general review of orthogonal signaling is also discussed, this being at the core of the SDF approach. Subsequently the DSSS-SDF approach that incorporated the IQ domain as an added degree of freedom was introduced. It is demonstrated that adding this degree of freedom enables efficient channel estimation and equalization at the receiver. The main feature is that SDF achieves much narrower beams than BF and that a number of antennas as low as 4 is sufficient to achieve beamwidths of about 1°. In both the real case and IQ-based scenario, simulations are carried out to demonstrate the robustness of the proposed scheme. In all the simulations in this section, a pure LOS scenario has been considered. Chapter 4 investigates the robustness and the performance of SDF in more realistic environments.

Chapter 4

Influence of multipath channels on DSSS-SDF-IQ

4.1 Introduction

In the previous section, the Direct Sequence Spread Spectrum - Spatial Data Focusing with IQ (DSSS-SDF-IQ) investigation assumed a free-space Line of Sight (LOS) propagation channel, an ideal scheme sufficient for purposes of proof of concept, however, it is not representative of practical propagation environments. To investigate the robustness of Spatial Data Focusing (SDF) under practical scenarios, the influence of multipath channels is considered in this section. Multipath can degrade radio frequency (RF) transmission by adding unwanted reflected and subsequently delayed signals to the direct path signal. Delayed signals have different phases than the LOS signal, thus, the overall multipath effect would either add constructively or destructively with the LOS signal producing a stronger, weaker or even diminishing total received signal. Multiple techniques exist that mitigate the distortion due to multipath, including equalization, multi-carrier modulation, and spread spectrum modulation. In this work, DSSS modulation is used. For a communication system to be able to combat the effects of multipath, it should have the ability to resolve the various multipath components (MPC).

This chapter investigates the influence of multipath channel environments on SDF and to an extension the robustness of the SDF scheme in such an environment. It is organized as follows: Section 4.2 discusses the general multipath resolution ability of typicall DSSS communication system. Section 4.3 carries out a numerical review of the proposed DSSS-SDF-IQ scheme as implemented over a general multipath environment. Section 4.4 discusses the characterization of wireless communication channels using ray tracing techniques with a specific focus on the radio-channel parameters that are used in this work to describe the channel response, e.g., K-factor, RMS delay spread, and power delay profiles. Section 4.5 introduces the aspects of DSSS-SDF-IQ over urban canyon channel model. Here, three channel models are investigated, they include, the 2-ray ground reflected model, 4-ray, and 6-ray urban canyon models. Finally Section 4.6 investigates the influence of space-time geometrical channel models on SDF, focusing on the GBSBM. Here we analyze the performance of SDF under small cell environments. This section will be concluded by remarks on the above stated studies.

4.2 Multipath resolution capacity of classical DSSS

The analysis in this section is limited to multipath channels due to specular reflections off a number of objects in the path of the propagating signal. The output of

specular multipath channels consists of the sum of multiple attenuated and time-delayed versions of the transmitted signal each arriving at the receiver without distortion. Classical DSSS modulation schemes mitigate against multipath by eliminating the unwanted multipath components (MPC) that would otherwise cause interference [145]. To illustrate the benefits of DSSS in multipath mitigation, a deterministic time-invariant linear-system model for a specular multipath channel is considered.

Given a transmitted signal $S(t)$, a spread-spectrum pulse consisting of L_c chips, a baseband equivalent model for the RF channel $h(t)$, and a matched filter $g(t)$ matched to the incoming spread signal at the receiver, it follows that $g(t) = S(T_a - t)$ for $-\infty < t < \infty$, with T_a as an arbitrary time chosen for sampling the matched filter output. The channel output of such a scheme is given as $r(t) = S(t) * h(t)$, and $r(t)$ feeds into the matched filter at the receiver. The matched filter output is thus given as $y(t) = S(T_a - t) * g(t) * h(t) = R * h(t)$, where $R = S(T_a - t) * g(t)$, for simplicity, letting $T_a = 0$ gives $g(t) = S(-t)$. R is thus an auto-correlation function, as we had already seen in (3.8), it can also be expressed as $R(t) = \int S(\tau)S(\tau - t)d\tau$, where $R(0) = \int S^2(\tau)$ is the energy in the spreading signal. R is determined by the chip waveform and the aperiodic auto-correlation function R_{ac} for the sequence C_q, i.e., $R_{ac}(q) = C_0C_q + C_1C_{q+1} + \cdots + C_{L_c-1-q}C_{L_c+1}$ for $0 \leq q \leq L_c - 1$, L_c is the spreading code length. $R_{ac}(q) = R_{ac}(-q)$ for $1 - L_c \leq q \leq -1$ and $R_{ac}(q) = 0$ for q outside the auto-correlation range. The scheme attains its peak at $R_{ac}(0)$, on the other hand, when $q \neq 0$, it starts to experience side lobes. Assuming rectangular chip wave-forms of duration T_c, then $R(qT_c) \approx R_{ac}(q)T_c \; \forall \; q$, if the side lobes are neglected, then R is just a triangular function centered at the origin with a base equal to $2T_c$, as such, $R(t)$ is zero out of the range $-T_c$ to T_c and $R(t) = R(0)[(T_c - |t|)/T_c]$ within the same interval, a classical auto-correlation function for a signal that consists of a sequence of rectangular pulses of duration T_c.

In a SISO baseband channel characterized by specular multipath consisting of K multipath components, the impulse response between is [145, 143]:

$$h(t) = \sum_{k=0}^{K-1} \alpha_k \delta(t - \tau_k) e^{-j\omega\tau_k} \tag{4.1}$$

where K is the number of multipaths, α_k is the gain associated with each multipath, τ_k is the time of arrival of each MPC. The complex exponential $e^{-j\omega\tau_k}$ accounts for the carrier phase rotation along the respective propagation path. Let us assume a $K-$path specular multipath channel, with corresponding differential time delays given as, τ_{ref}, $\tau_{ref} + \Delta$, $\tau_{ref} + 2\Delta$, ..., $\tau_{ref} + (K)\Delta$, where τ_{ref} is the time of arrival of the first MPC. Then the matched filter output $y(t) = (R * h)(t)$ can further be expressed as:

$$y(t) = \sum_{k=0}^{K-1} \alpha_k R(t - \tau_{ref} - k\Delta) e^{-j\omega\left(\tau_{ref} + k\Delta\right)} \tag{4.2}$$

Typical $y(t)$ outputs are depicted in Fig. 4.1, with a focus on two scenarios, i.e., $T_c \leq \Delta/2$ and $T_c > \Delta/2$. Where $T_c \leq \Delta/2$, Fig. 4.1a, sampling $y(t)$ at τ_{ref}, $\tau_{ref} + \Delta$, to $\tau_{ref} + (K^{MP})\Delta$, will result in K multipath components (MPC), further processing will be carried out by just selecting the strongest MPC, usually the LOS path if existing. If the system locks onto one multipath components (MPC), then all the rest will fall out of the correlation range and thus will be canceled out in the despreading process (depending on the auto-correlation properties of the code that is being used). In cases where $T_c > \Delta/2$, Fig. 4.1b, the MPCs will superimpose on each other,

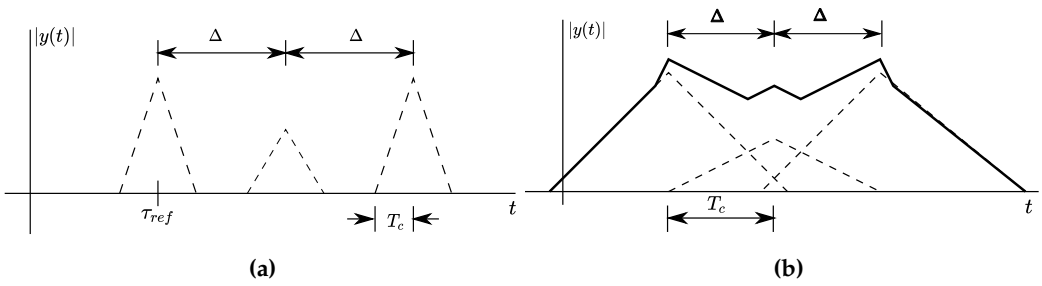

Figure 4.1: Matched filter output with chip durations: (a) larger than than half differential delays (b)less than half differential delays [145].

making it difficult to resolve the various multipath components (MPC) despite them being present in the composite signal. This effect occurs when a DSSS system employs low chip rates. Therefore, to attain multipath resolution, a DSSS system has to employ as high a chip rate as the system can permit, in other words, multipath systems set a lower bound on chip rate. In summary, in schemes where the signal correlation spread T_c is less than the minimum mutual delay of the successive multipath signals, i.e. $\Delta\tau_{k,\min} = \min_k\{\Delta\tau_k - \Delta\tau_{k-1}\} : T_c \leq \Delta\tau_{k,\min}$, multipath signals after the matched filter will not overlap, since they can be fully resolved in time and do not interfere with each other, otherwise they will overlap and thus become non-resolvable.

4.3 DSSS-SDF-IQ over multipath channels: A general case

In this section, we present the numerical analysis of the proposed Direct Sequence Spread Spectrum - Spatial Data Focusing with IQ (DSSS-SDF-IQ) scheme over a K-path multipath channel, the goal is to be able to visualize how the scheme is influenced by MPC. The Direct Sequence Spread Spectrum - Spatial Data Focusing with IQ (DSSS-SDF-IQ) signals used to feed the antenna array at the transmitter were given in (3.35) as:

$$S_i(t) = \sum_{n=0}^{\infty} A_i[n] \sum_{q=0}^{L_c-1} C_i[q] g(t - nT - qT_c) \tag{4.3}$$

Extending the impulse response of a K-MPC channel given in (4.1) to MISO channel, the received signal in a Direct Sequence Spread Spectrum - Spatial Data Focusing with IQ (DSSS-SDF-IQ) scheme is given by:

$$r_{MP}(t) = \sum_{i=1}^{N} \sum_{0}^{K-1} \left(S_i * h_{ik}\right)(t) = \sum_{i=1}^{N} \sum_{k=0}^{K-1} \alpha_{ik} S_i(t - \tau_{ik}) e^{-j\omega\tau_{ik}} + n(t) \tag{4.4}$$

where $z(t)$ is the additive white Gaussian noise. The channel output is fed into the matched filter at the receiver, the matched filter output is therefore given as, $y_{MP}(t) = r_{MP}(t) * g^*(-t)$, which when further worked out can be expressed as:

$$y_{MP}(t) = \sum_{i=1}^{N} \sum_{n=0}^{\infty} A_i[n] \sum_{k=0}^{K-1} \left\{ e^{-j\omega\tau_{ik}} \sum_{q=0}^{L_c-1} C_i[q] f(t - \tau_{ik} - nT - qT_c) \right\} + z(t) \tag{4.5}$$

Recall that $g(t)g^*(-t) = f(t)$, which is a raised cosine function. This matched-filter output is a sufficient statistic for synchronization and decoding, i.e., from it, we can estimate the signal synchronization parameters and investigate the presence or absence multipath components. We assume in the following that there exists a Line of Sight (LOS) path between the TX array and the receiver. Assuming the ith Line of Sight (LOS) path arrives the first one at the receiver with respect to all ikth other MPC, the index $k = 0$ therefore indicates a Line of Sight (LOS) path. Defining τ_{ref} as the time of arrival of the Line of Sight (LOS) component of the reference antenna within the TX array, here the first antenna (i.e., $i = 1$), then we can define $\tau_{ik} = \tau_{ref} - \Delta\tau_{ik}$ where $\Delta\tau_{ik}$ is the differential delay of the kth path between the ith TX antenna and the single-antenna receiver with respect to τ_{ref}. Thus, after sampling, (4.5) can now be expressed as:

$$\begin{aligned}\hat{y}_{MP}[lT_c] =& \sum_{i=1}^{N}\sum_{n=0}^{\infty} A_i[n] \sum_{k=0}^{K-1} \left\{ e^{-j\omega(\tau_{ref}+\Delta\tau_{ik})} \sum_{q=0}^{L_c-1} C_i[q] f(lT_c - \tau_{ref} - \Delta\tau_{ik} - nT - qT_c) \right\} \\ &+ z[lT_c] \end{aligned} \tag{4.6}$$

The despreading of $\hat{y}_{MP}[lT_c]$ onto the jth code at the receiver leads to:

$$\begin{aligned}\hat{S}_j[m] = \frac{1}{L_c} \sum_{i=1}^{N}\sum_{n=0}^{\infty} A_i[n] \sum_{k=0}^{K-1} \Bigg\{ & e^{-j\omega(\tau_{ref}-\Delta\tau_{ik})} \\ & \sum_{l=mL_c+1}^{(m+1)L_c} \sum_{q=0}^{L_c-1} C_i[q] C_j[l - mL_c + \lfloor \Delta_{init}^{ik}(\theta) - \hat{\Delta}(\theta) \rfloor] f(\psi) \Bigg\} \\ & + z_j[m] \end{aligned} \tag{4.7}$$

with $\psi = (l-q)T_c - nT - \tau_{ref} - \Delta\tau_{ik}$, $\tau_{ref} = r/c$, $\Delta\tau_{i0} = (i-1)\Delta\tau$, and $\Delta\tau = b/c \sin\theta$. Δ_{init}^{ik} is the delay between the codes $\mathbf{C_i}$ generated at the receiver and each code $\mathbf{C_i}$ embedded in the composite signal that has undergone a propagation delay of τ_{ik} over the kth MPC.

Assuming the synchronizer is able to lock on the Line of Sight (LOS) path ($k = 0$) from the reference antenna ($i = 1$), it leads to $\hat{\Delta} = \Delta_{init}^{10}(\theta)$. If we further assume a narrowband scenario with a not-extremely large antenna array, i.e., $Tc \ll (N-1)\Delta\tau$, we have $\lfloor \Delta_{init}^{i0}(\theta) - \hat{\Delta}(\theta) \rfloor = 0$ and the second line in (4.7) vanishes when $i \neq j$ for $k = 0$, i.e., for the Line of Sight (LOS) components. This leads to:

$$\begin{aligned}\hat{S}_j[m] =& A_j[m] e^{-j\omega(\tau_{ref}-\Delta\tau_{j0})} f(\omega(j-1)\Delta\tau) \\ &+ \frac{1}{L_c} \sum_{i=1}^{N}\sum_{n=0}^{\infty} A_i[n] \sum_{k=1}^{K-1} \Bigg\{ e^{-j\omega(\tau_{ref}-\Delta\tau_{ik})} \\ & \sum_{l=mL_c+1}^{(m+1)L_c} \sum_{q=0}^{L_c-1} C_i[q] C_j[l - mL_c + \lfloor \Delta_{init}^{ik}(\theta) - \hat{\Delta}(\theta) \rfloor] f((l-q)T_c - nT - \Delta\tau_{ik}) \Bigg\} \\ &+ z_j[m] \end{aligned} \tag{4.8}$$

The first line in (4.8) represents the SDF operation in a Line of Sight (LOS) environment while the two other lines represent the interference caused by MPC. Assuming the codes used exhibit good cross-correlation properties such as Gold codes with sufficiently long code length L_c (see section 3.4.2), the cross-correlation between

two codes is 0 even if they are time shifted between each other, i.e., $\langle C_i[q], C_j[q \pm \Delta] \rangle = 0 \; \forall \; \Delta$. (4.8) can be therefore simplified into:

$$\begin{aligned}\hat{S}_j[m] =& A_j[m] e^{-j\omega(\tau_{ref}-\Delta\tau_{j0})} f(\omega\,(j-1)\,\Delta\tau) \\ &+ \frac{1}{L_c} \sum_{n=0}^{\infty} A_j[n] \sum_{k=1}^{K-1} \Bigg\{ e^{-j\omega(\tau_{ref}-\Delta\tau_{jk})} \\ &\sum_{l=mL_c+1}^{(m+1)L_c} \sum_{q=0}^{L_c-1} C_j[q] C_j[l - mL_c + \lfloor \Delta^{jk}_{init}(\theta) - \hat{\Delta}(\theta) \rfloor] f((l-q)T_c - nT - \Delta\tau_{jk}) \Bigg\} \\ &+ z_j[m] \end{aligned} \tag{4.9}$$

remembering that $T = L_c T_c$.

Observing that $\lfloor \Delta^{jk}_{init}(\theta) - \hat{\Delta}(\theta) \rfloor \geq 0$ and assuming the maximum channel delay (the time of arrival of the last non-negligible path) is less than $L_c T_c$, (4.9) can be further simplified into:

$$\begin{aligned}\hat{S}_j[m] =& A_j[m] e^{-j\omega(\tau_{ref}-\Delta\tau_{j0})} f(\omega\,(j-1)\,\Delta\tau) \\ &+ \frac{1}{L_c} \sum_{n=0}^{\infty} A_j[n] \sum_{k=1}^{K-1} \Bigg\{ e^{-j\omega(\tau_{ref}-\Delta\tau_{jk})} \\ &\sum_{q=0}^{L_c-1} C_j[q] C_j[q + \lfloor \Delta^{jk}_{init}(\theta) - \hat{\Delta}(\theta) \rfloor] f([m-n]L_c T_c - \Delta\tau_{jk}) \Bigg\} \\ &+ z_j[m] \end{aligned} \tag{4.10}$$

Finally, taking into account the fast decay of the raised cosine pulse $f(t)$, the inter-symbol interference can be neglected:

$$\begin{aligned}\hat{S}_j[m] =& A_j[m] e^{-j\omega(\tau_{ref}-\Delta\tau_{j0})} f(\omega\,(j-1)\,\Delta\tau) \\ &+ \frac{1}{L_c} A_j[m] \sum_{k=1}^{K-1} \Bigg\{ e^{-j\omega(\tau_{ref}-\Delta\tau_{jk})} f(\Delta\tau_{jk}) \sum_{q=0}^{L_c-1} C_j[q] C_j[q + \lfloor \Delta^{jk}_{init}(\theta) - \hat{\Delta}(\theta) \rfloor] \Bigg\} \\ &+ z_j[m] \end{aligned} \tag{4.11}$$

The last summation term in the second line of (4.11) is the auto-correlation function denoted by $R_{ac}(\tau)$. (4.11) can therefore be written in a more compact form:

$$\begin{aligned}\hat{S}_j[m] =& A_j[m] e^{-j\omega(\tau_{ref}-\Delta\tau_{j0})} f(\omega\,(j-1)\,\Delta\tau) \\ &+ \frac{1}{L_c} A_j[m] \sum_{k=1}^{K-1} \Bigg\{ e^{-j\omega(\tau_{ref}-\Delta\tau_{jk})} f(\Delta\tau_{jk}) R_{ac}[\lfloor \Delta^{jk}_{init}(\theta) - \hat{\Delta}(\theta) \rfloor] \Bigg\} \\ &+ z_j[m] \end{aligned} \tag{4.12}$$

which is yet to be channel equalized.

The interference caused by MPC is determined by whether the auto-correlation in the second line of (4.12) vanishes or not. If the auto-correlation of the codes used is sharp enough, as soon as $\lfloor \Delta^{jk}_{init}(\theta) - \hat{\Delta}(\theta) \rfloor \neq 0$, the corresponding MPC vanishes. More specifically, we typically have for orthogonal Gold codes:

$$R_{ac}[\Delta] = \begin{cases} L_c & \text{for } \Delta = 0 \\ 1 & \text{elsewhere} \end{cases} \tag{4.13}$$

So for all MPC that leads to $\lfloor \Delta_{init}^{jk}(\theta) - \hat{\Delta}(\theta) \rfloor \neq 0$, the MPC term in (4.12) is attenuated by a factor L_c with respect to the Line of Sight (LOS) term and will therefore be negligible for long enough L_c. In essence longer length spreading sequences (or spreading factor) enable greater multipath mitigation. For an SDF operation similar to the LOS case occurs, it is required that T_c should be less than $\Delta\tau_{jk}$ for $k > 0$ (i.e., MPC).

Assuming the same channel estimation than in the previous chapter, that is:

$$\hat{h}_{ref} = \frac{1}{n_{pilot}} \sum_{n=1}^{n_{pilot}} \frac{\hat{S}_{ref}[n]}{A_{ref}[n]} \tag{4.14}$$

If $\lfloor \Delta_{init}^{jk}(\theta) - \hat{\Delta}(\theta) \rfloor = 0$ for $k > 0$ in (4.12), as the SNR and/or n_{pilot} get larger, the estimate tend to $\hat{h}_{ref} \to e^{-j\omega\tau_{ref}}$ similarly to the Line of Sight (LOS) case. So:

$$\hat{S}_j^{EQ}[m] = \frac{\hat{S}_j[m]}{\hat{h}_{ref}} \approx A_j[m] e^{-j\omega(j-1)\Delta\tau)} f(\omega\,(j-1)\,\Delta\tau) + z_j'[m] \tag{4.15}$$

However, if all MPC cannot be discriminated, i.e., $\lfloor \Delta_{init}^{jk}(\theta) - \hat{\Delta}(\theta) \rfloor \neq 0$ for some k, the channel estimate will face some errors and this will in turn jeopardise the correct decoding of the symbol coefficients $A_j[m]$ while performing the channel equalization $\hat{S}_j^{EQ}[m] = \hat{S}_j[m]/\hat{h}_{ref}$. In addition to the non-accurate channel equalization, the symbol estimation itself will also suffer from MPC interference introduced by the second term in (4.12).

From the above discussion it is evident that the use of spreading codes has very specific contributions towards increasing the robustness of the scheme: (1) The de-spreading process at the receiver does the exact opposite to noise signals, i.e., spreads it out, this has the ultimate effect of increasing the effective SNR at the receiver, boosting data recover ability; (2). Considering the correlation properties of a typical direct sequence spread spectrum scheme in a multipath environment with resolvable components, multipath mitigation is as simple as performing correlation with the correlator locked to a selected path, whereas power from this path will be fully collected, the MPC will simply be neglected as they fall out the auto-correlation spread. The ability of spreading codes to mitigate MPC depends on the chip duration T_c and the code parameters (e.g., L_c, auto-/cross-correlation properties) as well as on the channel behavior, and especially its delay spread. Therefore, a trade-off between bandwidth ($\approx 1/T_c$) and robustness to MPC should be observed to ensure sufficiently robust operation of the SDF scheme in a given propagation channel. Next sections assess the performance of the scheme under different propagation environments and introduce the channel models used for this assessment.

4.4 Characterizing wireless channel via Ray Tracing

The performance of wireless communication system is significantly influenced by the underlying radio channel properties. As such, to investigate the robustness of a given system, designers are called upon to use mathematical models to describe the channels. Modeling approaches can either be stochastic or site-specific. In the

case of stochastic modeling, the critical properties of wave propagation like multi-path fading, are represented by probability distributions. This approach to modeling, being largely generic, is preferred when characterizing unknown propagation environments.

Site-specific modeling on the other hand is preferred when the interest is on a specific environment, e.g., a known urban street, or a block of buildings, in such cases the channel investigations are 'site-specific', as such, site-specific channel response information will be required. To realize channel response information for site specific scenarios, the designers may carry out extensive measurements campaigns of channel responses for a massive population of transmit-receive paths and have this information stored in an accessible database for system simulations. This approach though, is limited by the number of transmitter - receiver paths that can be sampled, i.e., to acquire accurate data, quite a large number of such paths has to be sampled, a process that is labor intensive and costly.

An alternatively approach is to use environment simulators, basically computer programs that: (1) emulate the physical environment; and (2) use wave propagation physics to predict the radio signal produced at any receive point from any transmit point. Computer simulations are less precise in terms of channel description, however, this is traded off with the fact that they are less costly and can be employed on a very large scale and with minimal effort given well defined physical environments. Indeed, depending on the number and variability of artifacts in a communication channel, perfect emulation may not be possible, as such, for site-specific modeling, the goal is to predict the channel responses throughout areas that are statistically similar to actual ones.

Radio channel responses can be described via multiple channel parameters, in this work, focus will be placed on three: (1) Power delay profile; (2) Root mean square angle spread; (3) the Ricean K-factor, which together with power loss dictates the narrow band fading distribution; and (4) the RMS delay spread, σ_{rms}, which is a measure of the pulse dispersion of the channel.

4.4.1 Power delay profile (PDP)

The Power delay profile (PDP) illustrates the variation of the power of individual path as a function of the respective delay. For the simulations in this work, it is presented as power and delay variation along the receiver positions. Given that the employed ray tracing techniques in the simulations in this work are deterministic, power, and delays are some of the direct outputs from the channel models under investigation.

4.4.2 RMS angle spread

The angle spread realizations depict the dispersion of the received signal in the angular domain. Ideally, channels that exhibit wide angular spreads indicate large capacity whereas those that exhibit narrow angular spread indicate enhanced spatial selectivity [146]. There exists two approaches for realization of angle spreads: use of the Line of Sight (LOS) path as the reference to calculate the spreads and the circular wrapping technique [147]. In this work the former is used. Angular spread

is thus given as:

$$\sigma_\psi = \sqrt{\frac{\sum_{i=1}^{K-1} P_i \psi_i^2}{\sum_{i=1}^{K-1} P_i} - \left(\frac{\sum_{i=1}^{K} P_i \psi_i}{\sum_{i=1}^{K-1} P_i}\right)^2} \tag{4.16}$$

where P_i is the power and ψ is the AOA of the ith multipath component.

4.4.3 K-Factor

The K-factor can be defined as the ratio of the power in the strongest MPC, assumed to be here the line-of-sight (LOS) component, to the total power of the other MPC, assumed to be here the non-LOS (NLOS) components. It is a measure of the extent of fading on the link, where lower K means deeper fading. Various algorithms has been proposed to estimate the K factor, they include, the moment method, estimation from impulse responses, estimation from frequency responses (coherence method). In this work K-factor is estimated from the impulse responses. Indeed the channel impulse response represents the rays received at different delays. As such, the ray having the largest magnitude is considered the Line of Sight (LOS) component. The sum of the powers of the remaining rays thus make up the scatter power. In such a case, K-factor is thus defined as the ratio of the Line of Sight (LOS) power to the scatter power. In a communication channel, the LOS component is normally identified as being the one that exhibits the shortest delay.

4.4.4 RMS Delay Spread

The RMS delay spread measures the pulse dispersion of a communication channel. The pulse dispersions are a result of the different propagation paths (delays) taken by a signal through a channel. RMS delay spread is defined as the second central moment of the power delay profile given as:

$$\Delta_\tau = \sqrt{\overline{\tau^2} - \overline{\tau}^2} \tag{4.17}$$

where

$$\overline{\tau} = \frac{\sum_{i=1}^{K} P_i t_i}{\sum_{i=1}^{K} P_i} \qquad \overline{\tau^2} = \frac{\sum_{i=1}^{K} P_i t_i^2}{\sum_{i=1}^{K} P_i} \tag{4.18}$$

K is the number of received rays; and P_i and t_i are the power and arrival time of ith ray respectively. Substituting for (4.18) into (4.17) it is seen that;

$$\Delta_\tau = \frac{1}{\sum_{i=1}^{K} P_i} \sqrt{\sum_{i=1}^{K} \sum_{j=1}^{K} P_i P_j (t_i - t_j)^2} \tag{4.19}$$

where K is the number of received rays; and P_i and t_i are, respectively, the power and arrival time of ith ray. (4.19) can also be written as,

$$\Delta_\tau = \frac{1}{\sum_{i=1}^{K} \rho_i} \sqrt{\sum_{i=1}^{K} \sum_{j=1}^{K} \rho (t_i - t_j)^2} \tag{4.20}$$

where ρ_x is the normalized power of xth ray

$$\rho_x = \frac{P_x}{\sum_{i=1}^{N} P_i} \tag{4.21}$$

where $0 \leq \rho_x \leq 1$. From (4.20) it is evident that RMS delay spread does not rely on the ray origin, i.e., $\tau = 0$, neither does it rely transmit power, it only depends on the power ratios of the rays, in essence it only depends on delay differences. This makes it valid metric for validating the proposed SDF scheme.

4.5 DSSS-SDF-IQ over urban canyon channel model

In Section 4.3, a general review of the influence multipath transmission on the DSSS-SDF-IQ communication scheme was discused, we saw that use of DSSS can significantly increase the effective SNR at the receiver and mitigate against multipath interference. In this section, DSSS-SDF-IQ is modeled over a more practical channel model, the street canyon 6-ray model, which is characterized by both direct Line of Sight (LOS) rays and reflected rays bouncing off the ground and building walls of a typical urban street. The urban canyon (UC) model is the classical model used to investigate typical urban micro (UMi) with outdoor to outdoor (O2O) propagation deployment scenarios [148].

To characterize this channel model, ray-tracing (RT), a deterministic channel modeling approach, is employed. The RT approach offers accurate and detailed angular information making it a suitable candidate for predicting time-varying and multiple-input multiple-output (MIMO) channels for various frequency bands. Ray tracing algorithms can be implemented by using either the imaging or the ray-launching methods. In this work, the imaging method is adopted. It exploits geometries from a combination of transmission position, receiving position, and reflecting surfaces to derive a propagation path. The three critical parameters needed to estimate propagation characteristics using ray tracing are: the propagation distance, incident angle to the reflecting surface, and complex permitivity of the reflecting surface. The propagation distance and the incident angle to the reflecting surface are derived from ray-tracing estimation results whereas the complex permittivity of the reflecting surface is a predetermined static parameter.

Two types of Urban Canyon channels are modeled with the proposed Direct Sequence Spread Spectrum - Spatial Data Focusing with IQ (DSSS-SDF-IQ) : the four ray, and the 6-ray urban canyon channel model. Actually the 6-ray is a build up on 4-ray model, and the 4-ray model itself consists of a 2-ray (ground reflected model), and two other rays that exhibit single reflections on sidewalls. For clarity, the approach in this section will do a build up down from the classical 2-ray model through the 6-ray case.

4.5.1 Specular Multipath Modelling

From the study of propagating electric fields, given a channel model featuring Line of Sight (LOS) and reflected rays like the one depicted by the two-ray ground reflected model shown in Fig. 4.2a, the total received E-field, $E_{TOT} = E_{MPC} + E_{LOS}$, where E_{MPC} and E_{LOS} are the E-field due to the multipath components (MPC) and direct LOS paths respectively. The two are given as [118]:

$$E(r^{LOS}, t)_{LOS} = \frac{E_0 r_0}{r^{LOS}} \cos(\omega_c (t - \tau_{LOS})) \tag{4.22}$$

$$E(r^{MPC},t)_{MPC} = \Gamma \frac{E_0 r_0}{r^{MPC}} \cos(\omega_c(t-\tau_{MPC})) \tag{4.23}$$

where $|E(r,t)| = (E_0 r_0)/r$ represents the envelope (amplitude) of the E-field r meters away from the base station. E_0 and r_0 are free-space E-field, and a reference distance respectively, and Γ is the reflection coefficient of the E-field which can either be horizontally ($\Gamma_\perp$) or vertically ($\Gamma_{||}$) polarized, and is given as:

$$\Gamma_\perp = \frac{\sin(\theta_i) - \sqrt{\epsilon_r - \cos^2(\theta_i)}}{\sin(\theta_i) + \sqrt{\epsilon_r - \cos^2(\theta_i)}} \tag{4.24}$$

and

$$\Gamma_{||} = \frac{-\epsilon_r \sin(\theta_i) + \sqrt{\epsilon_r - \cos^2(\theta_i)}}{\epsilon_r \sin(\theta_i) + \sqrt{\epsilon_r - \cos^2(\theta_i)}} \tag{4.25}$$

where $\epsilon = \epsilon_r \epsilon_0$ is the complex permitivity of the material, and θ_i the angle of incidence [118]. The channel impulse response defines the rays received at different

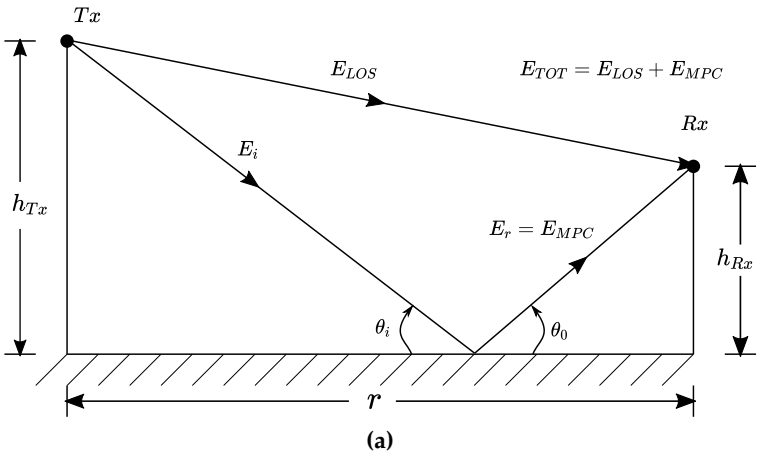

Figure 4.2: Two-ray ground reflection model

delays, as such, the ray having the largest magnitude is considered as the Line of Sight (LOS) component and the sum of the remaining rays make up the "scatter" power. Attenuation of the non-LOS ray is expressed relative to the Line of Sight (LOS) ray from (4.22) and (4.23), so that for horizontally polarized E-fields it can be presented as:

$$\frac{|E_{MPC}(r^{MPC},t)|}{|E_{LOS}(r^{LOS},t)|} = \frac{|\alpha_{MPC}|}{|\alpha_{LOS}|} = \Gamma_\perp \frac{r^{LOS}}{r^{MPC}} \tag{4.26}$$

where α is the channel attenuation coefficient.

From (4.26) and the definition of K-factor, we can deduce that:

$$\frac{1}{\sqrt{K}} = \Gamma_\perp \frac{r^{LOS}}{r^{MPC}} \tag{4.27}$$

4.5.2 Two-rays Ground-Reflection channel model

The two-rays ground-reflection model is a multipath radio propagation model that predicts the path losses between a transmitting antenna and a receiving antenna when they are in line of sight (LOS). Generally, the two antenna each have different height. The received signal having two components, the Line of Sight (LOS)

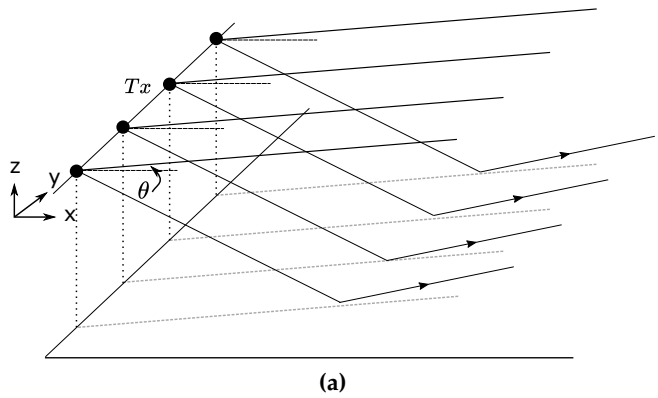

Figure 4.3: Two-ray ground reflection model geometry

component and the reflection component formed predominantly by a single ground reflected wave. In most cases this model is adequate for predicting the characteristics of line-of-sight micro-cell channels in urban environments. Fig. 4.3 illustrates its exact architecture with respect to the MISO scheme under investigation. The model consists of a N-element array (4 in this case) base station, with the transmit (TX) elements lying along the y-axis at the origin and the receive antennas located at its broadside. Rays emitted by each element propagate to the receiver via two paths, the direct line of sight and over a ground reflected path. The transmit and receive antennas are respectively positioned h_{Tx} and h_{Rx} above the ground.

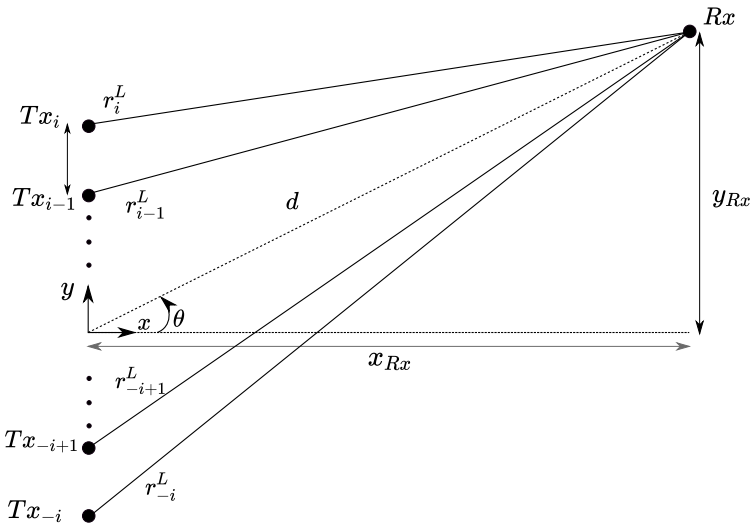

Figure 4.4: Geometry of the direct line of sight setup

Fig. 4.4 illustrates the setup geometry of the Line of Sight (LOS) paths. An N-element antenna array with an inter-element spacing of b meters lies on the y-axis of a Cartesian coordinate system whose origin is at the center of the antenna array. The transmitter elements coordinates are given as:

$$\begin{cases} x_{Tx_i} = 0 \\ y_{Tx_i} = ib \end{cases} \quad \text{with } i = \left\{ -\frac{N-1}{2}, \ldots, \frac{N-1}{2} \right\}$$

The receiver (Rx) can locate itself anywhere within the xy-plane and can be represented by the polar coordinates of its current position or via Cartesian coordinates.

$$\begin{cases} x_{Rx} = d\cos\theta \\ y_{Rx} = d\sin\theta \end{cases}$$

where d is the distance from the receiver to the center of the array and θ is the angular position of the receiver relative to the antenna array broadside. The LOS paths r_i^{LOS} corresponding to the various channels of Fig. 4.4 are given as:

$$r_i^{LOS} = \sqrt{(x_{Rx} - x_{Tx_i})^2 + (y_{Rx} - y_{Tx_i})^2} \tag{4.28}$$

$$= \sqrt{d^2 + ((ib)^2 - 2ibd\sin\theta} \tag{4.29}$$

The path length difference Δr_i^{LOS} relative to a pre-defined reference path r_{ref}^{LOS} is given as

$$\Delta r_i^{LOS} = r_i^{LOS} - r_{ref}^{LOS} \tag{4.30}$$

The SDF effect is dependent on the corresponding delay differences $\Delta\tau_i^{LOS}$ due to (4.30), which can be found by dividing it by the speed of light c as

$$\Delta\tau_i^{LOS} = \frac{\Delta r_i^{LOS}}{c} \tag{4.31}$$

In all the ray tracing simulations in this section, we shall mostly use the Line of Sight (LOS) path as reference path. For the 2-ray ground reflection model, in addition to the Line of Sight (LOS) channels we also have the ground reflected path. The exact geometric architecture combining the two is depicted in Fig. 4.5. It is made up of a 4x1 MISO system, each antenna having a Line of Sight (LOS) path and a single ground reflected multipath component. The model represents a stationery transmit base station (BS), whereas the receiver can locate itself anywhere in the xyz-plane. On consideration of the ground reflection, then a third (antenna height) coordinates are added to the geometry, as such, the transmitter and receiver coordinates are respectively given as,

$$\begin{cases} x_{Tx_i} = 0 \\ y_{Tx_i} = ib \\ z_{Rx_i} = h_{Tx_i} \end{cases} \quad \text{and} \quad \begin{cases} x_{Rx} = d\cos\theta \\ y_{Rx} = d\sin\theta \\ z_{Rx} = h_{Rx} \end{cases} \tag{4.32}$$

where h_{Rx} and h_{Tx}, are the receiver and transmitter heights respectively, b is the inter-element spacing, i is the antenna index number, and the distance d is measured along the ground plane and given as $d_i = (i-1)b\sin\theta$, $i = 1, 2, ..., N$. Using the method of images the path lengths corresponding to the two multipath components (Line of Sight (LOS) and ground reflected) in Fig. 4.5 are given as,

$$\begin{aligned} r_i^{LOS} &= \sqrt{(x_{Rx} - x_{Tx_i})^2 + (y_{Rx} - y_{Tx_i})^2 + (z_{Rx} - z_{Tx_i})^2} \\ r_i^{GR} &= \sqrt{(x_{Rx} - x_{Tx_i})^2 + (y_{Rx} - y_{Tx_i})^2 + (z'_{Rx} - z_{Tx_i})^2} \end{aligned} \tag{4.33}$$

where $z'_{Rx} = -z_{Rx}$. The channel impulse response for this ground reflected 2-ray model is thus given as:

$$h_i(t) = \alpha_i^{LOS}\delta(t - \tau_i^L)e^{-j\omega\tau_i^{LOS}} + \alpha_i^{GR}\delta(t - \tau_i^G)e^{-j\omega\tau_i^{GR}} \tag{4.34}$$

where α_i and τ_i represent the wave attenuation constant between TX_i and RX and the propagation delay respectively. $e^{-j\omega\tau_i^{MPC}}$ represents the phase shift due to wave propagation through the channel, and L and G represent the Line of Sight (LOS) and ground reflected paths respectively. $\tau_i^{LOS} = r_i^{LOS}/c$; similarly $\tau_i^{GR} = r_i^{GR}/c$, where c is the speed of light and r_i^{LOS} and r_i^{GR} are the respective path lengths of the different MPC. The channel output, $r(t)$, is the sum of the convolution of the transmitted

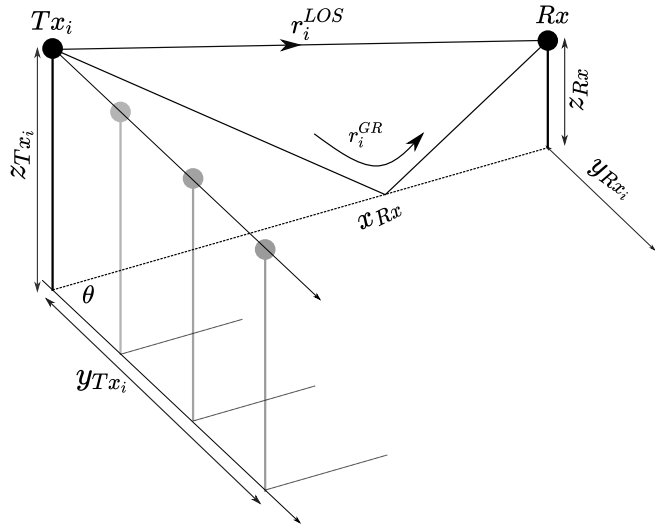

Figure 4.5: Ground reflected two r-ray channel model

signals and the corresponding channel impulse responses and is given as:

$$r(t) = \sum_{i=1}^{N}(S_i * h_i)(t) \tag{4.35}$$

Simulations

Simulations are carried out on Matlab™ software to validate the proposed SS-SDF scheme and compared with classical (true time delay) beam-forming scheme. The specifications used for the simulations are: 4X1 MISO scheme, over a ground reflected (2-ray) multipath channel model; $SNR = 11$dB; chip rate of 200 MHz; Inter-element spacing of 0.8λ; Orthogonal Gold codes of code length $L_c = 32$; roll-off factor of 0.22; and BER threshold set at 10^{-3}. The implementation assumes horizontal polarization and the relative permittivity of the ground is set to concrete ($\epsilon_r = 4.5$).

Channel Characterization

In this section the 2-ray ground reflection channel model is characterized to give us insights into how it may influence transmitted signals propagating through it. Figs. 4.6a, 4.6b and 4.7a represent plots for characterization of RMS delay spread, K-factor, and power delay profiles respectively. It is observed, that both the delay spread and K-factor diminish with increasing distance, this is actually expected in classical fading channels. Indeed, as seen in the power delay profile in Fig. 4.7a,

the closer to the transmitter the receiver, the more dominant the Line of Sight (LOS) path. The spread in time is also much less when the receiver is far away from the transmitter.

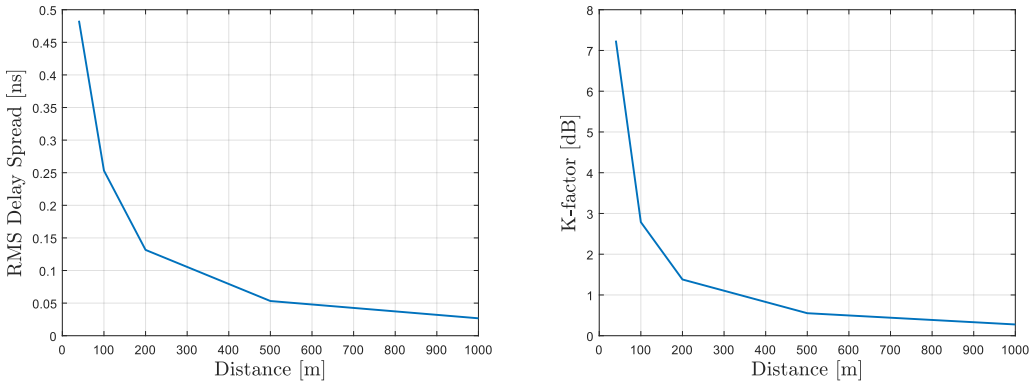

(a) (b)

Figure 4.6: Channel characterization (a) RMS delay spread (b) K-factor

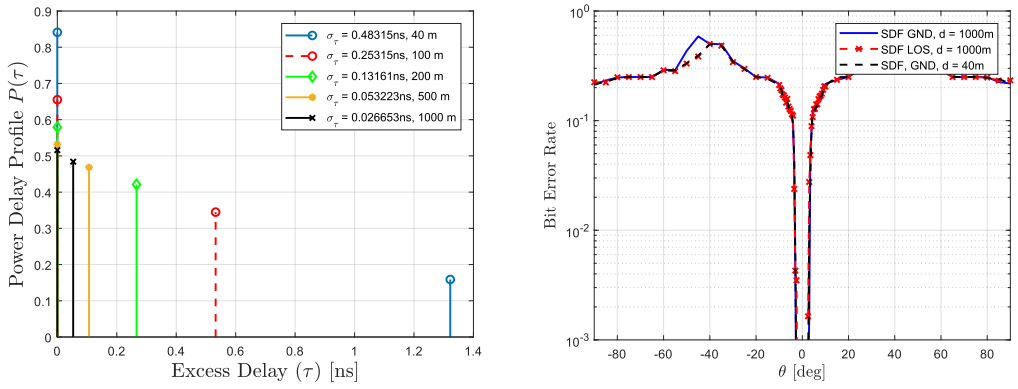

(a) (b)

Figure 4.7: (a) Channel Power Delay Profiles (b) Comparison between BER vs Theta in Line of Sight (LOS) and with 2-ray channel model $SNR = 11dB, L_c = 32$

BER vs. Receiver angular orientation

Fig. 4.7b depicts plots for BER vs. user angular position for various TX-RX distances and compared with Line of Sight (LOS) case for a case where the number of antennas is set to $N = 2$ and $BER = 13$ dB. As seen, with the 2-ray channel model, the SDF still operates well where a main beam is maintained at broadside, similarly to the LOS case. In this situation, the delay spread, take an example of the 1000m case, is equal to 0.05 ns, which is much less than the chip duration $T_c = 1/200\text{MHz} = 5\text{ns}$. In such a case, it is not possible for the system to resolve for the individual MPC, and yet, results appear to be not disturbed by the presence of the reflection on the ground, as the BER vs θ for over the ground case largely resembles that of the LOS case.

This can be explained by the fact that the height of the antennas is small compared to the distance between the transmitter and the receiver. In such a case, the reflection coefficient on the ground for the horizontal polarization is $\Gamma_\perp \approx -1$ and the channel response can be simplified as:

$$h_i(t) = \alpha \left(e^{-j\omega \frac{r_i^{LOS}}{c}} - e^{-j\omega \frac{r_i^{GR}}{c}} \right) \tag{4.36}$$

assuming a narrowband scenario (i.e., the envelope delay has been neglected) and far-field conditions. Let us write $r_i^{GR} = r_i^{LOS} + \Delta r$, the channel is now written as:

$$h_i(t) = \alpha e^{-j\omega \frac{r_i^{LOS}}{c}} \left(1 - e^{-j\omega \frac{\Delta r}{c}} \right) \tag{4.37}$$

where

$$\Delta r = \sqrt{r_i^{LOS^2} + (z_{TX} + z_{RX})^2} - r_i^{LOS} = r_i^{LOS} \left(\sqrt{1 + \frac{(z_{TX} + z_{RX})^2}{r_i^{LOS^2}}} - 1 \right) \tag{4.38}$$

Observing $(z_{TX} + z_{RX}) \ll r_i^{LOS}$, we can write:

$$\Delta r \approx r_i^{LOS} \left(1 + \frac{1}{2} \frac{(z_{TX} + z_{RX})^2}{r_i^{LOS^2}} - 1 \right) = \frac{1}{2} \frac{(z_{TX} + z_{RX})^2}{r_i^{LOS}} \tag{4.39}$$

Assuming paraxial approximation:

$$\Delta r \approx \frac{1}{2} \frac{(z_{TX} + z_{RX})^2}{d + (i-1) b \sin\theta} \tag{4.40}$$

Neglecting $(i-1) b \sin\theta$ with respect to d leads to:

$$\Delta r \approx \frac{1}{2} \frac{(z_{TX} + z_{RX})^2}{d} \tag{4.41}$$

The term in (4.41) becomes small when $d \gg (z_{TX} + z_{RX})^2$ but in any case, does not depends on θ. Injecting (4.41) into (4.37) leads to:

$$h_i(t) = \alpha e^{-j\omega \frac{r_i^{LOS}}{c}} e^{-j\frac{\omega}{2}\frac{\Delta r}{c}} 2j \sin \frac{\omega}{2} \frac{\Delta r}{c} \tag{4.42}$$

So except for a sine term on the channel's magnitude that describes the possible constructive and destructive interference, the channel phase in (4.42) is similar to the LOS channel albeit a constant phase term $\frac{\omega}{2}\frac{\Delta r}{c} + \frac{\pi}{2}$ that does not depend neither on θ nor on the antenna index. This term is therefore estimated and compensated thanks to the channel estimation. Consequently, reflections on the ground do not disturb much the SDF operation as shown by the results in Fig. 4.7b.

Fig. 4.8 compares also the performance of SDF with beamforming in the case of the 2-ray ground reflection model but with receiver located at $d = 100$ m from the transmit array, SNR set to 13 dB and code length $L_c = 8$. The blue solid and dashed curves respectively represent SDF at $N = 4$ and $N = 2$ attaining beamwidths as shown in Table 4.1. Evidently SDF exhibits better spatial selectivity than classical beamforming in this case.

In our earlier discussion, we outlined that one advantage of spread spectrum is

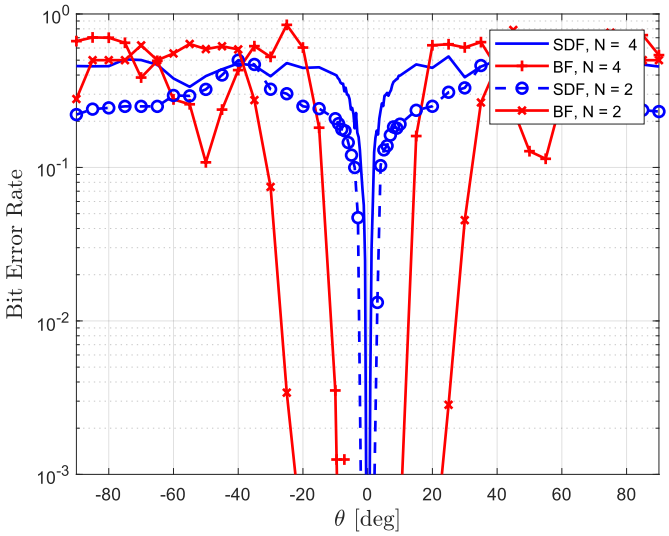

Figure 4.8: BER vs. receiver angular orientation when $SNR = 13, Lc = 8, d = 100$ [m]

Scheme	No. of Antennas (N)	Beamwidth (°)
SDF	4	1.2
BF	4	21
SDF	2	4.2
BF	2	44.2

Table 4.1: Table comparing the beamwidths of the two GND schemes when $SNR = 13, Lc = 8, d = 100$ [m]

to increase the effective SNR at the receiver. It was demonstrated that that whereas SDF exhibited consistency with change in SNR, beamforming did not. The same behavior is naturally experienced with the 2-ray model as depicted in Fig. 4.9b where beamforming experiences a beamwidth difference of approximately 16° when the code length increases from $L_c = 8$ to $L_c = 32$. The spatial selectivity achieved with respect to the the number of antennas N is shown in Fig. 4.9a, the corresponding table representing the exact results is given in Table 4.2. This plot validates the results found in the LOS case showing that the SDF scheme is more consistent to change in code length, and to an extension the effective SNR at the receiver. The performance obtained are also very similar to those obtained in the LOS channel model.

N	L_c	BF Beamwidth [°]	SDF Beamwidth [°]
	8	54.5°	4.3°
2	32	64°	5.1°
	8	20.6°	0.9°
4	32	26.1°	1.2°
	8	15.2°	0.72°
6	32	23°	0.75°

Table 4.2: Table showing a comparison of beamwidths for different N with respect to L_c for the 2-ray scenario

The actual behaviour of the SDF scheme is visualized using scatter plots in Fig. 4.10.

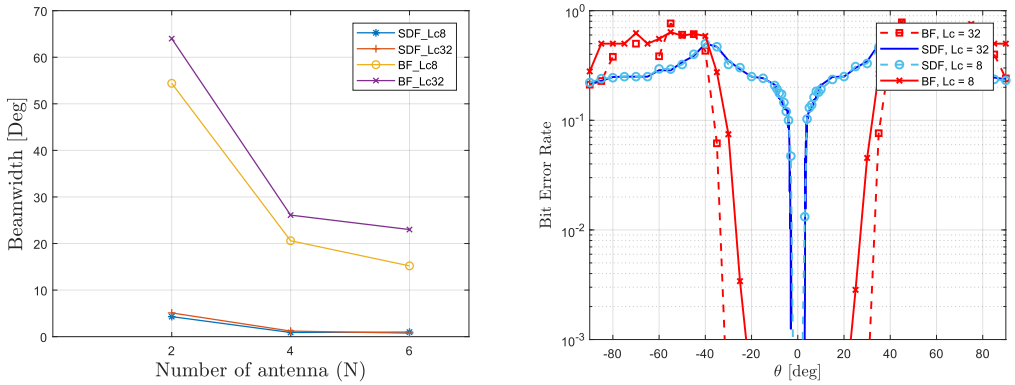

(a) **(b)**

Figure 4.9: (a) Number of antennas vs beamwidth (b) BER vs θ when $SNR = 13, N = 2, d = 100$ [m]

They represent a $N = 2$ scheme with code length set to $L_c = 32$. The red solid dots represent the transmit constellation pattern, while the blue dashed ones represent the received constellations. It is observed in Figs. 4.10a and 4.10c, that at broadside, the two dimensions have preserved the transmit constellation patterns as the ones applied at the receiver. Fig. 4.10b also retained the transmit constellation patterns, this is possible in SDF as the corresponding dimension S_1 also happens to be selected as the reference dimension for channel estimation and equalization, as such it will in most case be returning correctly decoded information despite being in the unwanted position. The same cannot be said of the other dimensions, in this case S_2. In Fig. 4.10d the rotation effect of the exponential term of equation (4.15) is observed here. In this case, when the user is located in the unwanted position the constellation is distorted and the data cannot be decoded correctly in that dimension. Indeed this effect is even further severe in the case of even more dimensions.

Remarks

The investigation of the SDF performance in 2-ray over the ground reflection channel model has been studied. Simulations carried out that demonstrated its robustness over such a scheme. Its performance has been compared with that of classical beamforming and it has been shown that SDF still exhibits better performance than classical beamforming scheme. It has also been shown that in the typical DSSS based SDF scheme the performance of the 2-ray ground reflection similar to that of the Line of Sight (LOS) case.

4.5.3 4-ray channel model: urban canyon

In the 4-ray model, in addition to the LOS and the ground reflection rays, two more rays representing single reflections from the side walls are considered. Fig. 4.11 shows the aerial view of the described scenario. The coordinates of transmitter are x_{Tx}, y_{Tx}, z_{Tx}, and those of the receiver are x_{Rx}, y_{Rx}, z_{Rx}. (4.43) represent the path lengths taken by the various multipath components (MPC), where superscript GR stands for distances for the ray reflected from the ground, LR the traveled distance for the ray reflected from left side wall, and RR the traveled distance for the ray

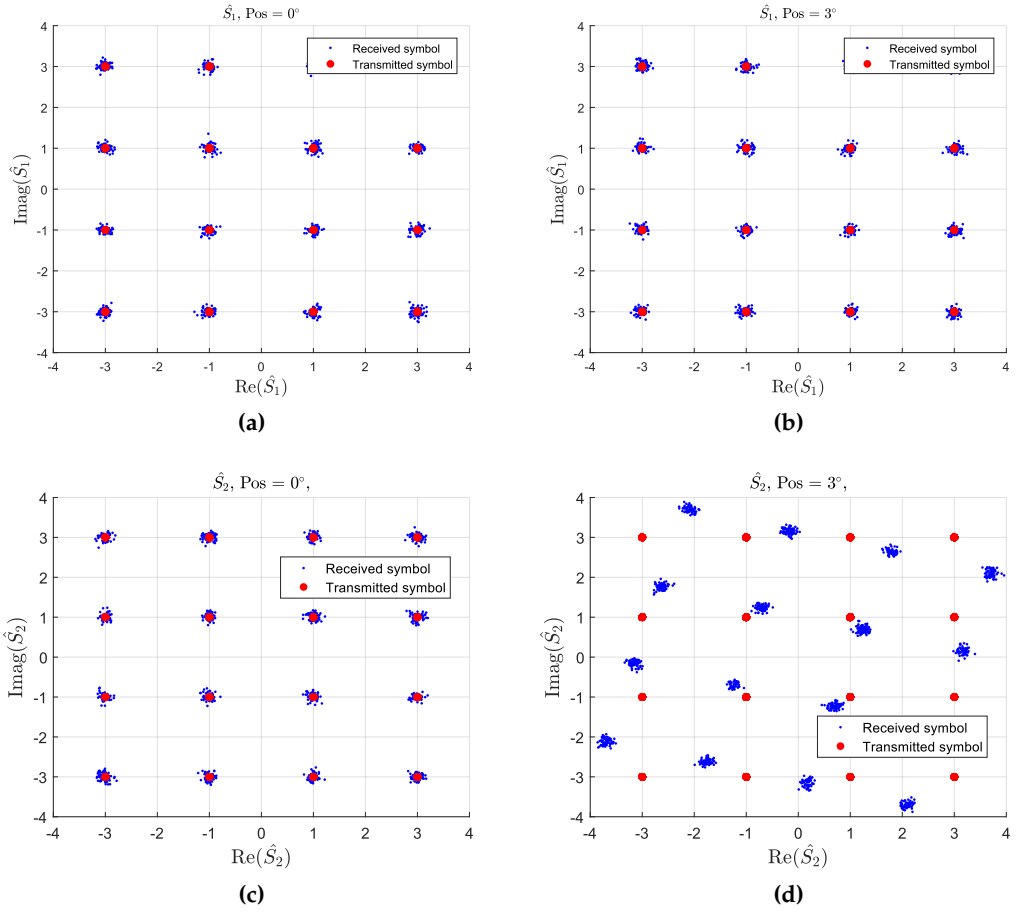

Figure 4.10: Scatter plots for symbol evolution of dimension S_1 and S_2. When $L_c = 32$, $N = 2$, $SNR = 13$ dB

reflected from right side wall.

$$r_i^{LOS} = \sqrt{(x_{Rx} - x_{Tx_i})^2 + (x_{Rx} - x_{Tx_i})^2 + (z_{Rx} - z_{Tx_i})^2} \tag{4.43a}$$

$$r_i^{GR} = \sqrt{(x_{Rx} - x_{Tx_i})^2 + (y_{Rx} - y_{Tx_i})^2 + (z'_{Rx} - z_{Tx_i})^2} \tag{4.43b}$$

$$r_i^{LR} = \sqrt{(x_{Rx} - x_{Tx_i})^2 + (y'_{Rx} - y_{Tx_i})^2 + (z_{Rx} - z_{Tx_i})^2} \tag{4.43c}$$

$$r_i^{RR} = \sqrt{(x_{Rx} - x_{Tx_i})^2 + (y''_{Rx} - y_{Tx_i})^2 + (z_{Rx} - z_{Tx_i})^2} \tag{4.43d}$$

The virtual positions of the Rx are given by,

$$z'_{Rx} = -z_{Rx} \tag{4.44}$$

$$y'_{Rx} = -y_{Rx} \tag{4.45}$$

$$y''_{Rx} = 2 \cdot D - y_{Rx} \tag{4.46}$$

where D is the width of the street. From (4.26), the respective attenuation a_i are given as:

$$a_i^{path} = \frac{\alpha_i^{path}}{\alpha_i^{LOS}} = \Gamma_{\perp}^{path} \frac{r_i^{path}}{r_i^{LOS}}$$

where *path* represents respectively GR, LR, and RR.

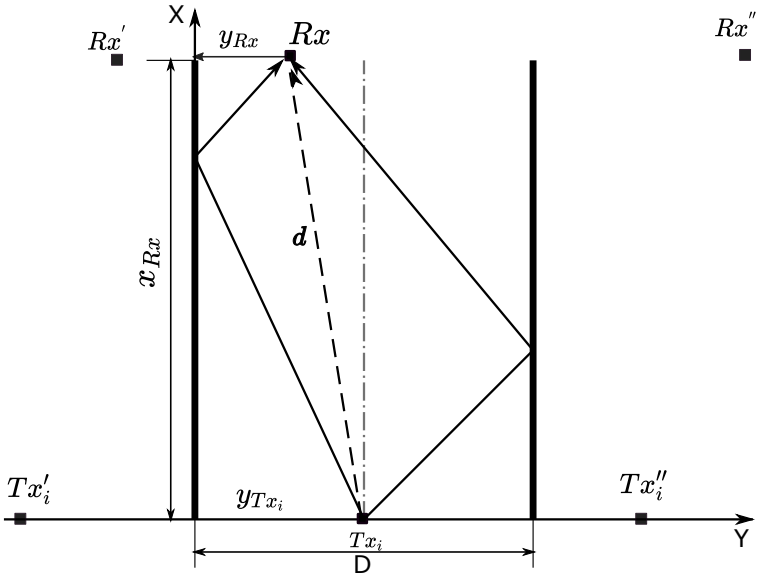

Figure 4.11: Geometry of urban canyon 4-ray model

Characterizing the 4-ray urban canyon channel model

Fig. 4.12 shows plots for the simulation characterizing the 4-ray scheme with a street of $D = 23$m. Fig. 4.12a depicts the plots for the power delay profile for a set of user distances from the transmitter viz, $40, 100,$ and 100m. As expected, the power is attenuated with increasing excess delay. Fig. 4.12b depicts the evolution of the RMS delay spread with increasing distance between the receiver and transmitter. It is observed that it is slighlty over 11ns closer to the transmitter (40m) and it reduces to just under 2ns at about 380m. In Fig. 4.12c, we observe the evolution of the K-factor which decreases as the distance between Tx and Rx increases. Fig. 4.12d depicts the effect of code length on the phase estimates at broadside when $d = 100$m. In the simulation and without loss of generality, a normalization is applied such that the phase of the LOS path of the reference channel (i.e., first antenna) is $0°$. Here the ideal case is represented by blue dotted plot representing a noiseless LOS propagation condition, the solid yellow line on the other hand depicts a LOS propagation scenario with applied noise of SNR = 11dB. The solid blue and red plots represent respectively the case of urban canyon channel with and without applied noise. It can be noticed that the longer the code length, the better the reference channel phase estimation (i.e., estimate close to $0°$) since the pilots are also spread and benefit from increases effective SNR. The last curve, the solid black plot represent a case where the calculated RMS delay spread is larger than the applied chip duration. It is observed that in this case is far off from the expected ideal. These results show that when the scheme achieve MPC mitigation (i.e., T_c small enough with respect to the channel delay spread), the channel phase estimation performs well, which is essential for proper SDF operation. This is verified with BER plots in the next section using the 6-ray model as explained.

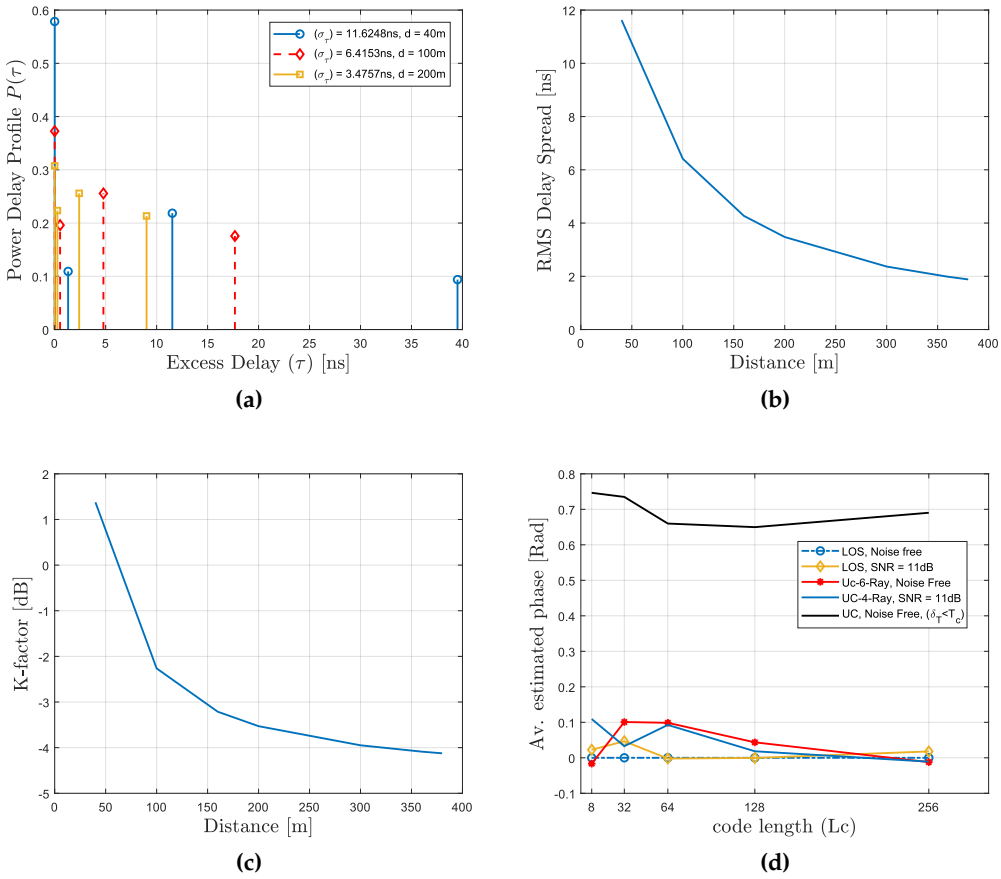

Figure 4.12: Plots showing channel characterization for 4-ray model (a) Power Delay Profile (b) RMS Delay Spread evolution with distance (c) K-factor evolution with distance (d) Phase estimates as a function of code length when $d = 100$m and $T_c = 5$ns

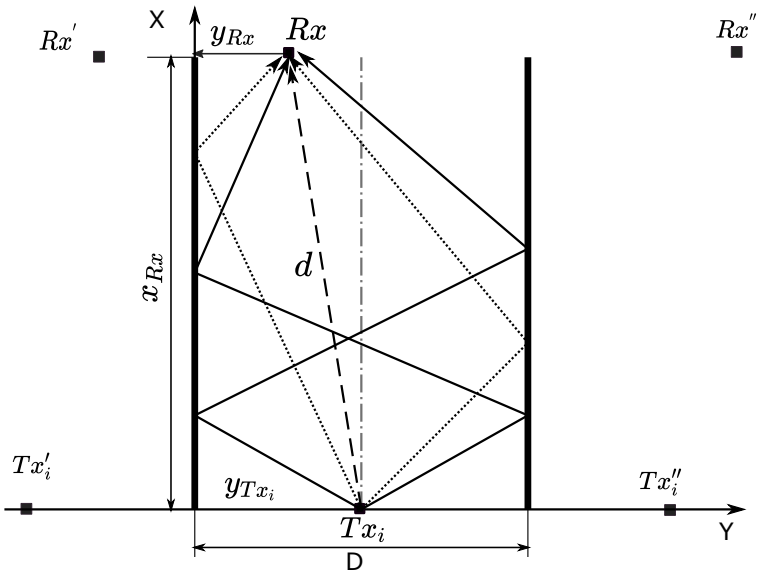

Figure 4.13: Geometry of urban canyon 6-ray model

4.5.4 6-ray channel model: urban canyon

This section investigates the influence of the street canyon 6-ray multipath channel model on DSSS-SDF-IQ. The street canyon 6-ray channel model is characterized by both direct LOS rays and reflected rays bouncing off the ground and building walls of a typical urban street set up. The difference with the 4-ray model is that double bouncing on the walls are also taken into account. Fig. 4.13 illustrates the geometry of the model. It is characterized by the following types of paths: line-of-sight (LOS), ground reflected (GR), left wall reflected (LR), right-wall reflected (RR), double reflection right-wall-left-wall (RLD), double reflection left-wall-right-wall (LRD), all towards the receiver. From imaging principles, the corresponding path distances are calculated as shown in (4.47) [149]:

$$r_i^{LOS} = \sqrt{(x_{Rx} - x_{Tx_i})^2 + (x_{Rx} - x_{Tx_i})^2 + (z_{Rx} - z_{Tx_i})^2} \tag{4.47a}$$

$$r_i^{GR} = \sqrt{(x_{Rx} - x_{Tx_i})^2 + (y_{Rx} - y_{Tx_i})^2 + (z'_{Rx} - z_{Tx_i})^2} \tag{4.47b}$$

$$r_i^{LR} = \sqrt{(x_{Rx} - x_{Tx_i})^2 + (y'_{Rx} - y_{Tx_i})^2 + (z_{Rx} - z_{Tx_i})^2} \tag{4.47c}$$

$$r_i^{RR} = \sqrt{(x_{Rx} - x_{Tx_i})^2 + (y''_{Rx} - y_{Tx_i})^2 + (z_{Rx} - z_{Tx_i})^2} \tag{4.47d}$$

$$r_i^{RLD} = \sqrt{(x_{Rx} - x_{Tx_i})^2 + (y'_{Rx} - y''_{Tx_i})^2 + (z_{Rx} - z_{Tx_i})^2} \tag{4.47e}$$

$$r_i^{LRD} = \sqrt{(x_{Rx} - xTx_i)^2 + (y''_{Rx} - y'_{Tx_i})^2 + (z_{Rx} - z_{Tx_i})^2} \tag{4.47f}$$

where the virtual position of the Rx is given by : $z'_{Rx} = -z_{Rx}$; $y'_{Rx} = -y_{Rx}$; $y''_{Rx} = 2 \cdot D - y_{Rx}$, and the Tx image coordinates are given by: $y'_{Tx} = -y_{Tx}$; $y''_{Tx} = 2 \cdot D - y_{Tx}$; D is the width of the street. r_i^{path} are the distances between Tx_i and Rx with respect to their respective x, y, z coordinates. Considering the geometry of the street canyon 6-ray model outlined above, it is evident that the receiver is bounded to movements limited by the width of the street in the xy-plane. For a street of width D, the receiver coordinates are confined within the intervals $y_{Rx} \in [-0.5D, 0.5D]$ and $\theta \in [-\sin^{-1} 0.5D/d, \sin^{-1}(0.5D/d)]$. The angular range over which the receiver is able to move, decreases when the distance d between transmitter and receiver increases. Thus at some given distance d_{max}, the receiver's angular movement range is the same as the max focusing range, beyond such a point receivers does no longer benefit from base station spatial focusing as the full width of the of the street will be illuminated by the beam.

Simulation and Results

Simulations are carried out in Matlab to investigate the robustness of the DSSS-SDF-IQ scheme over a urban canyon multipath environment. The parameters selected for this simulation are: street width $D = 23$m, the Rx stationed at various points points away from the Tx. Both Tx and Rx are below the rooftops. The relative permittivity for the side walls is set to glass wall ($\epsilon_r = 4.7$) while the ground is set to concrete at ($\epsilon_r = 4.5$). give the conductivity of both glass and concrete if taken into account. Orthogonal Gold codes of code length $L_c = 256$ are used. The SNR is set to 11 dB and the chip rate to 200 MHz (i.e., $T_c = 5$ns). The number of elements in the array is $N = 4$. The inter-elements distance is set to 0.8λ.

Urban canyon 6-ray channel model characterization

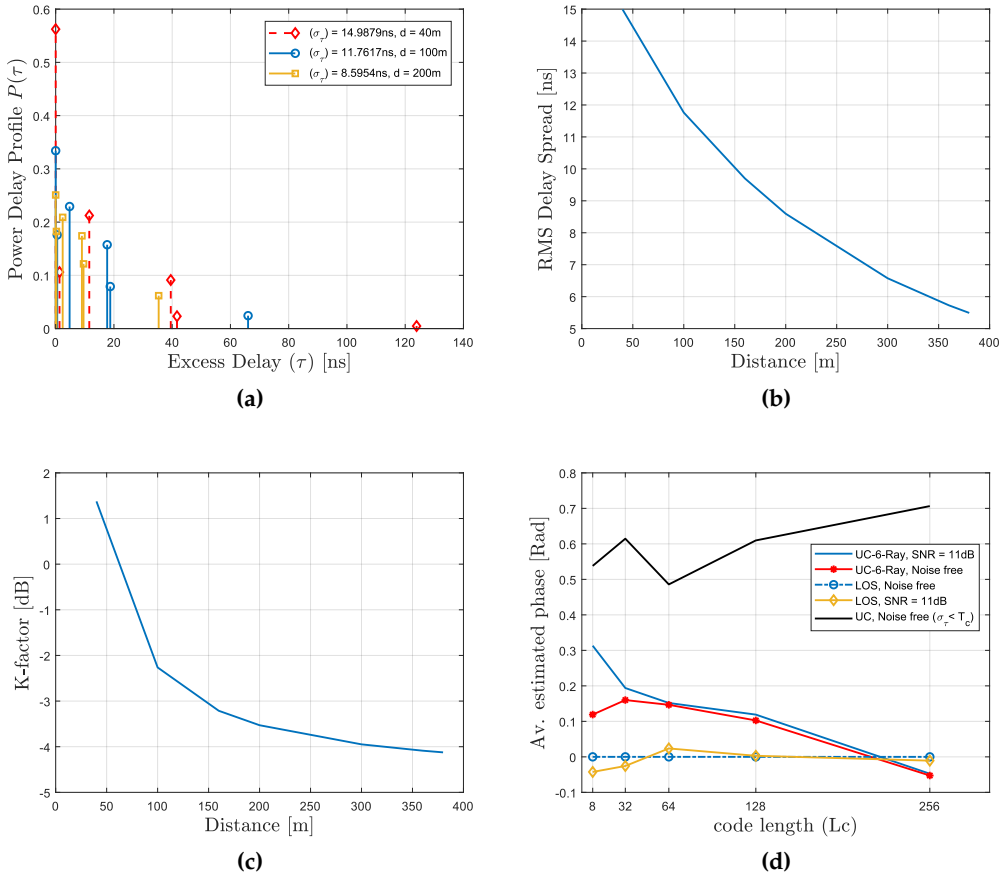

Figure 4.14: Plots showing channel characterization (a) Power Delay Profile (b) RMS Delay Spread evolution with distance (c) K-factor evolution with distance (d) Phase estimates as a function of code length when $d = 100$m

The plots in Figure 4.14 represent the characterization of the street canyon 6-ray channel model under investigation. Figure 4.14a depicts the variation of the power of each path with respect to the excess delay. In this simulation, power and delay variation along three possible receiver positions viz, 40, 100, and 200 m is observed. Given that ray tracing used here is deterministic, power and delays are one of the direct outputs from the channel model under investigation. It is observed that the channel exhibits classical fading properties where we observe the dominance of the LOS ray when the receiver is located near the transmitter and less so as it moves further away. The RMS delay spread takes a similar trajectory as shown in Fig. 4.14b. Recall that from (4.20), it was concluded that RMS delay spread does not necessarily rely on the ray origin, i.e., $\tau = 0$, neither does it rely transmit power, it only depends on the power ratios of the rays, in essence it only depends on path delay differences.

The plot in Figure 4.14c depict the evolution of the K-factor which is a measure of ratio of the power between the LOS ray and the NLOS ray. K-factor does influence the fading statistics of BER and average fading duration. In this case it is observed to decrease with distance signifying increased fading as the receiver moves further away from the transmitter.

In the literature it is clear that the process of spreading and the attendant despreading in DSSS influences the effective SNR at the receiver, also it is said that spread spectrum helps mitigate against multipath. The plots in Fig. 4.14d seek to get an insight into the aspects mentioned above when $d = 100$m. To do so the phases of the received signal are estimated at broadside when various length spreading sequences are applied for spreading. The blue dashed line represents an ideal case, i.e., noise free LOS propagation, it is observed that for all the code lengths the estimated phase is approximately 0°. The solid yellow with the diamond marker represents a LOS case with an SNR = 11dB applied to it. On it, we observe at shorter code lengths a phase deviation from the expected ideal. However it converges towards the ideal on application of longer spreading sequences.

The two following plots, the solid blue and solid red with dotted marker represent the cases of transmission over the urban canyon channel, and to an extension exhibit the effect of multipath. The solid red and solid blue plots represent the case for noise free propagation and propagation with applied noise at SNR = 11dB respectively. Together they clearly inform us that the presence of multipath does impact the phase estimation in this scheme. In addition they also tell us that actually use longer code plays a role towards reducing the effects caused by multipath, this is is observed from the fact that with increases code length the phase estimation converges towards the ideal case.

In the last plot, the solid black curve represents a case where the chip duration is greater than the RMS delay spread, i.e., $T_c = 5$ns and $\sigma_\tau = 4.2$ns. It shows that in this case, the phase estimate differs significantly from the expected ideal, so the spreading does not mitigate efficiently MPC. Therefore, the SDF operation may fail in such cases.

Direct Sequence Spread Spectrum - Spatial Data Focusing with IQ (DSSS-SDF-IQ) simulation results

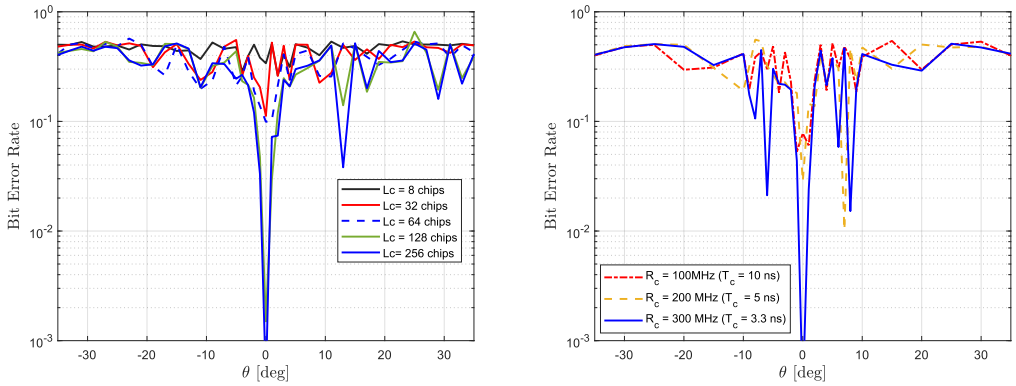

Figure 4.15: BER vs. changing user angular position. SNR = 11dB. (a) Effect of varying code lengths user at $d = 100$m (b) Effect of varying the chip rate user at $d = 200$m ($\sigma_\tau = 7.4$ns).

The plots in Fig. 4.15 represent the BER vs θ curves for the proposed urban canyon scheme (zoom in between $\theta = -35°$ and 35°). The first plot, i.e., Fig. 4.15a gives an insight into the effect of spreading sequence length to the scheme. As such with the user set at distance at $d = 100$m (delay spread = 11.49ns) from the transmit

array. Indeed from previous investigations, we know that an increase in code length increases the effective SNR, and also improves the phase estimation. It is thus observed in the plots that when we use a code length of $L_c = 256$ the scheme is able to attain the set acceptable BER threshold of 10^{-3}, attaining a beamwidth of $\approx 1^\circ$.

Fig. 4.15b on the other hand depicts the effect of varying the chip rate when $L_c = 256$ chips. From the literature, and specifically from our discussion in Section 4.2 it was clearly stated that an increase in chip rate results in better MPC mitigation. That view is validated here where it is observed that the performance of the scheme in terms of attaining the acceptable and achieving spatial selectivity is enhanced by larger chip rates.

Figures 4.16 and 4.17 depict the constellation plots of transmitted (in red single dots) and received (in blue, scattered dots) symbols respectively. Specifically, Figs. 4.16a to 4.16d represents the cases when the receiver is at broadside of the transmit array. They show that the received symbols preserve the transmit constellation pattern, as such, corresponding data points fall within decision zones that enable correct estimation, thus enhancing the probability of correct decoding. Figs. 4.17a to 4.17d, on the other hand, represents scenarios where the receiver is displaced at an angular orientation of 3° away from the pre-defined location. The transmit constellation patterns are no longer preserved in this case, as such, the probability of correctly decoding the transmitted data is significantly diminished.

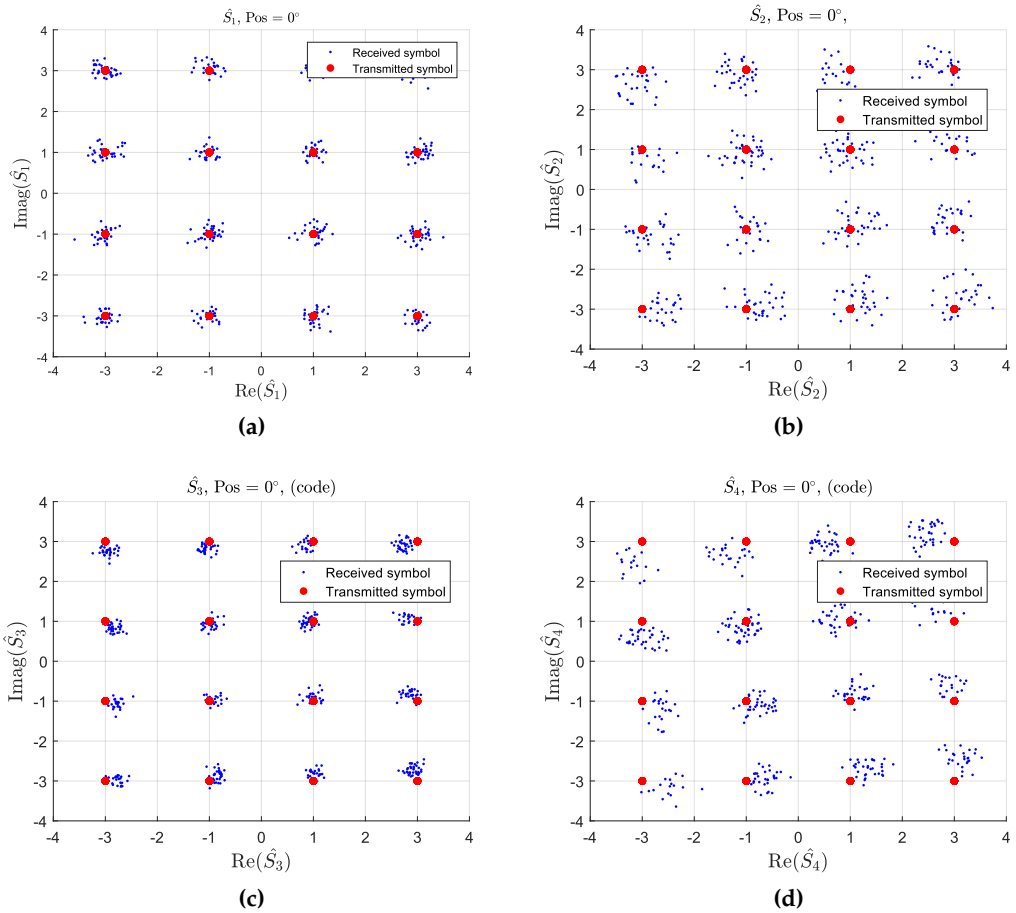

Figure 4.16: Constellation plots comparing 4 dimensions street canyon 6-ray channel model at broadside, when $SNR = 11$dB

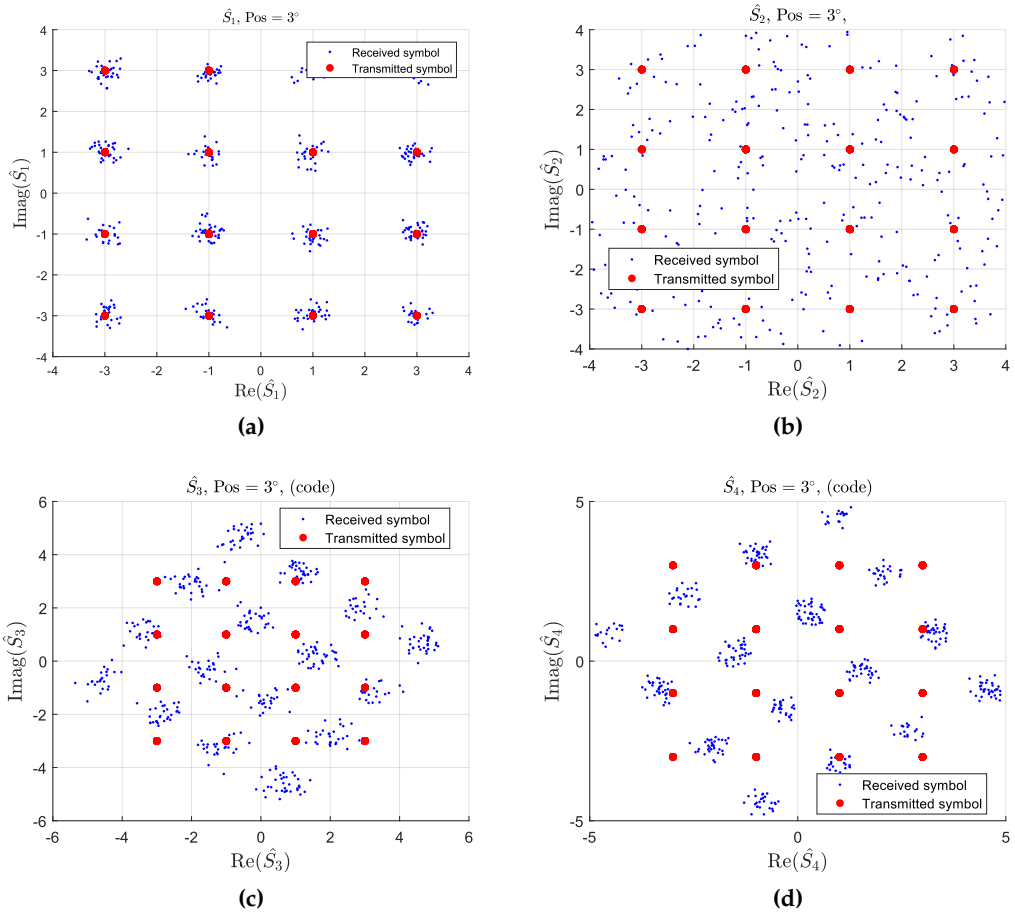

Figure 4.17: Constellation plots comparing 4 dimensions street canyon 6-ray at 3° away. when $SNR = 11$dB

A practical demonstration of the robustness of Direct Sequence Spread Spectrum - Spatial Data Focusing with IQ (DSSS-SDF-IQ) scheme

Figure 4.18: Transmitted Lenna, an SDF perspective when $L_c = 128$ chips, $N = 4$, $SNR = 11$dB

A more practical demonstration of this scheme is implemented by use of an actual image data set processed via DSSS-SDF-IQ and transmitted over the street canyon 6-ray channel model earlier characterized when the inter-element spacing of

the antenna array $b = 0.8\lambda$,SNR= 11dB, $d = 100$m, bandwidth is set at 200Mhz, number of antennas $N = 4$, and the code lenngth $L_c = 128$. The results are depicted in Figure 4.18. It consists of three images, the first one (to the left) is the transmitted image, the middle one is the image received when the receiver is located at the pre-defined location 0° (antenna array broadside at the acceptable BER threshold of 10^{-3}), and the third one (to the right) represents received image when the receiver is located 3° away from the pre-defined position (at a BER of approximately 10^{-1}). Evidently the SDF effect of increased BER in the unwanted location is explicitly demonstrated by the difference in quality between the two received images.

4.5.5 Remarks

Spatial data focusing was earlier proposed as a candidate alternative to classical power focusing schemes in wireless geocasting applications. This work proposed the spread spectrum based approach to SDF. It is demonstrated that it attains better spatial selectivity than power focusing schemes. The robustness of the scheme is subsequently investigated by implementing it over a street canyon 6-ray multipath channel model, where it is demonstrated that the scheme is actually robust in such environment, attaining a beamwidth of up to 1° at an acceptable BER threshold of 10^{-3}.

4.6 The influence of space-time geometrical channel models on SDF

Space-time channel models can be constructed from the statistics of the space-time system field function for an arbitrary channel. This statistical characterization of the channel can be expressed in terms of the space-time power spectral density of the given space-time system field function. The geometrical channel models developed depend on the choice of the coordinate systems, e.g. rectangular, cylindrical, and spherical. Using the notions of correlation distance, i.e., delay spread, various geometrical delay based channel models can be derived. Space-time geometrical channel models provide propagation information (e.g., DOA, Time-of-Arrival (TOA)) by which the performance of wireless communication systems and space-time systems, i.e., smart antennas, beamformers, SDF, can be analyzed. This section presents an investigation of one such model, the Geometrically Based Single Bounce Macrocell (GBSBM), and how it influences the SDF perfomance. GBSBM models macrocell environments characterized by relatively large antenna heights with respect to the receiver and assumes that the scatterers lie within circular ring about the receiver [118], it thus derives, for the circular model, AOA, TOA, joint TOA and AOA, and signal amplitude information, as outlined in the next section.

4.6.1 Geometrically Based Single Bounce Macrocell Channel Model

Macrocell Environment

Fig. (4.19) depicts the channel on the forward link for a macrocell environment. In this environment, it is usually assumed that the scatterers surrounding the receiver have either equal or slightly higher heights than the receiver. As such, the received signals arrive at the receiver from all directions after bouncing off the surrounding scatterers. The AOA at the receiver are uniformly distributed over $[0, 2\pi]$, given the position of the scatterers, only the azimuth plane is considered.

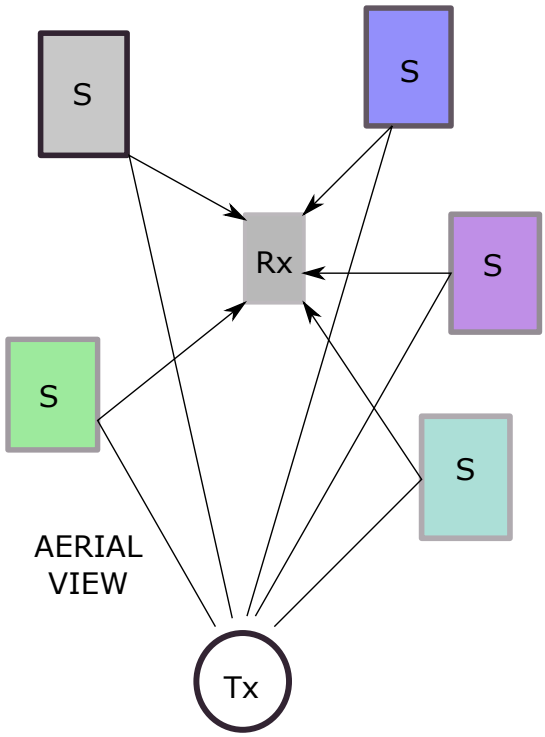

Figure 4.19: Macrocell environment — the receiver perspective (S stands for scatterer)

Geometry of the GBSBM model

Fig. 4.20 shows the geometry used to derive the GBSBM model [150]. The modelling

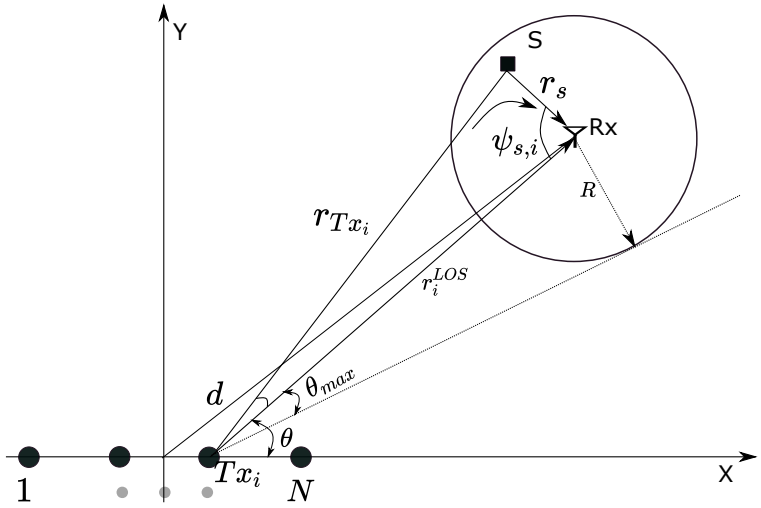

Figure 4.20: Macrocell environment — the mobile station perspective

of Geometrically Based Single Bounce Macrocell (GBSBM) model, from a geocasting perspective, makes the following assumptions [150]:

- The scatterers lie within a circular ring with radius R around the receiver
- The scatterers are assigned equal scattering coefficients with uniform random phases.

- Scatterers are omnidirectional re-radiating elements whereby the plane wave, on arrival, is reflected directly to the receiver antenna under no influence from other scatterers, i.e., single bounce behavior.

Considering a uniform distribution in a circle with radius R around the receiver as made in the assumptions above, the probability density functions (PDF) of the scatterer position parameters r_s and ψ_s, are given by [150]

$$f_{r_s}(r_s) = \frac{2r_s}{R^2} \quad 0 < r_s \leq R; \quad 0 \quad \text{elsewhere} \tag{4.48a}$$

$$f_{\psi_s}(\psi_s) = \frac{1}{2\pi} \quad 0 < \psi_s \leq 2\pi; \quad 0 \quad \text{elsewhere} \tag{4.48b}$$

and the joint probability distribution function describing the possibility of having the scatterer at position (r_s, ψ_s) is given as:

$$f_{r_s,\psi_s}(r_s, \psi_s) = f_{r_s}(r_s) f_{\psi_s}(\psi_s) \tag{4.49}$$

$$= \frac{r_s}{\pi R^2} \quad 0 < r_s \leq R \text{ and } 0 < \psi_s \leq 2\pi; \quad 0 \quad \text{elsewhere} \tag{4.50}$$

In simulation scenarios, the scatterer positions are determined by drawing independently from the distributions (4.48a) and (4.48b). Whereas the random drawing is evident for the uniform angular distribution in (4.48b), it is not straightforward for the distance in (4.48a), thus, the inversion method is applied. To do so, a uniform random number generator which can generate random variables, u, uniformly distributed on $[0, 1]$ can be used to sample from the distribution in (4.48b). The samples of r_s generated from samples for u are thus given as [151]:

$$r_s = F_{r_s}^{-1}(u) = \sqrt{R^2 u} \tag{4.51}$$

where $F_{r_s}(r_s)$ is the cumulative distribution function (CDF) of r_s. A new scatterer position is drawn for every θ of the receiver. Applying the law of cosines on triangle $T_{xi}R_xS$, yields the following expression for the path length r_{Txi} between the i-th transmit antenna and the scatterer:

$$r_{Tx_i} = \sqrt{r_s + (r_i^{LOS})^2 + 2r_i^{LOS} r_s \cos(\psi_{s,i})} \tag{4.52}$$

where r_i^{LOS} is given by, $r_i^{LOS} = (x_{Rx}^2 + (y_{Rx} - y_{Tx_i})^2)^{0.5}$. The non-LOS (NL) multipath components (MPC) path lengths between the i-th transmitter and the receiver is then given by,

$$r_i^{MPC} = r_s + r_{Tx_i} \tag{4.53}$$

Assuming K- scatterers, the impulse response for such a channel model can be represented as

$$h_i(t) = \sum_{k=0}^{K} \alpha_i k \delta(t - \tau_{ik}) e^{-j\omega\tau_{ik}} \tag{4.54}$$

where τ_{ik} and α_{ik} are the path propagation delay and attenuation factor respectively seen by the ith antenna due to the LOS path ($k = 0$) and to the K scatterers (k>0). Also, $\tau_{i0} = r_i^{LOS}/c$ and $\tau_{ik} = r_i^{MPC}/c$.

Simulations

Simulations are carried out on Matlab™ software to investigate the influence of GBSBM on DSSS-SDF-IQ. The specifications used for the simulations are: 4x1 MISO scheme, $SNR = 13$dB; chip rate of 200 MHz; Inter-element spacing of 0.8λ; Orthogonal Gold codes of code length $L_c = 128$; roll-off factor of 0.22; and BER threshold set at 10^{-3}; 10^5 bits are transmitted, for all the simulations the distance between the transmitter and receiver is set at $d = 100$m.

Geometrically Based Single Bounce Macrocell (GBSBM) channel model characteristics

Two important channel characteristics, i.e., delay spread and angular spread are characterised here with respect to the GBSBM model. Delay spread is obtained in the simulation as a function of R/d, where d is the distance between the TX array center and the mobile user. This is shown in Fig. 4.21 where the blue plots corresponding to the left y-axis depict the evolution of the ratio R/d vs. delay spread, specifically the solid and dashed blue plots represent the evaluations for 20 and 10 scatterrers respectively. d is kept constant at 100m and R is varied. The figure shows that as R/d increases, delay spread also increases linearly. The delay spreads used are obtained from an average of 100 channel realisations for 10 and 20 scatterers. On the other hand, the red plots in Fig. 4.21 depicts a comparison of the angle spread for a case of 10 and 20 scatterers (equally averaged over 100 channel realizations), as a function of the ratio R/d. d is kept at 100m while R is varied. It is observed that as the ratio R/d increases, the angle spread also increases linearly, similarly, increasing the number of scatterers increases the angle spread. Due to scattering,

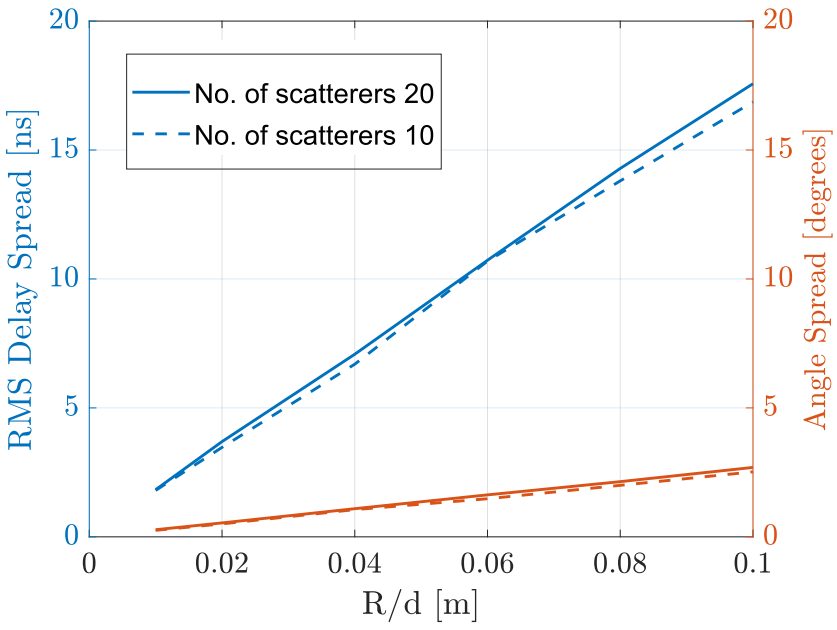

Figure 4.21: GBSBM channel characterization: Plot of delay spread and angle spread vs R/d

multipath components arrive at angles different from the direct component, angle spread is actually a measure used to determine the angular dispersion of the channel [150, 152]. From the knowledge of angle spread characteristics, a measure can be

determined which multipaths can be reduced using directional antennas, in fact in classical power focusing schemes, elimination of interfering multipaths requires the directional antennas that implement beamwidths smaller than the range of the AOA of the multipaths. In essence, narrower beams are critical for multipath rejection.

Fig. 4.22 depicts the evolution of BER vs θ comparing the cases with different numbers of applied scatterers when $R = 0.01d$m. It is observed that SDF attains spatial selectivity at the set BER threshold of 10^{-3} in all the chosen cases. In the zoomed in version in Fig. 4.22b, it is seen that actually the plots are not perfectly uniform, i.e., they experience small variability that can be attributed to the random nature of the channel realization.

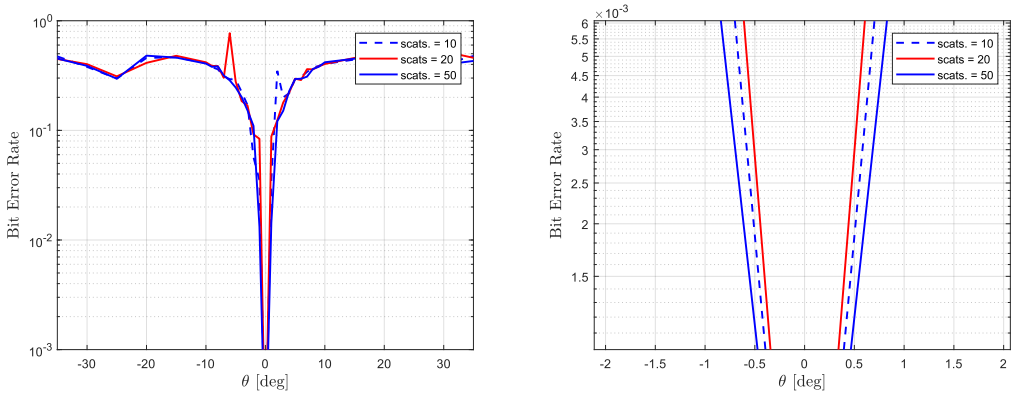

Figure 4.22: (a) BER vs θ comparison for various number of scatterers. (b) Zoomed out version when $SNR = 13$, $L_c = 128$, $d = 100m$, $R =$ 1m

The selected radius R, within which the scatterers are positioned does directly impact the propable path lengths that the rays may take, this in essence also affects the associated delays, thereby impacting the SDF scheme. The choice of R is thus critical determinant of the performance of SDF. We already saw in Fig. 4.22, that at $R = 0.01d$ the SDF scheme did attain the expected BER. Fig. 4.23 show the results of simulations where $R > 0.01d$. To do so, a constant scatter value was set in the simulation, in this case $n_{scatter} = 10$ and R varied. It is observed that with an increase in R the system does exhibit higher BER. While we could expect that with a larger delay spread, the spreading process could better mitigate MPC, it appears that large angular spread decreases SDF robustness.

Irrespective of the increasing delay spread with an increment in the R/d ratio, it is observed in the simulation that scheme exhibits higher BER. This can be attributed to the probability that there are scatterers which are located very close to the receiver and therefore the first MPC fall into the same chip as the LOS component leading to the failure of the scheme.

4.6.2 Perspective and Conclusion

This work investigated the influence of GBSBM channel model on spread spectrum based spatial data focusing. Specifically, GBSBM channel modelled, and the parameters angle spread and delay spread characterized over varied number of scatterers

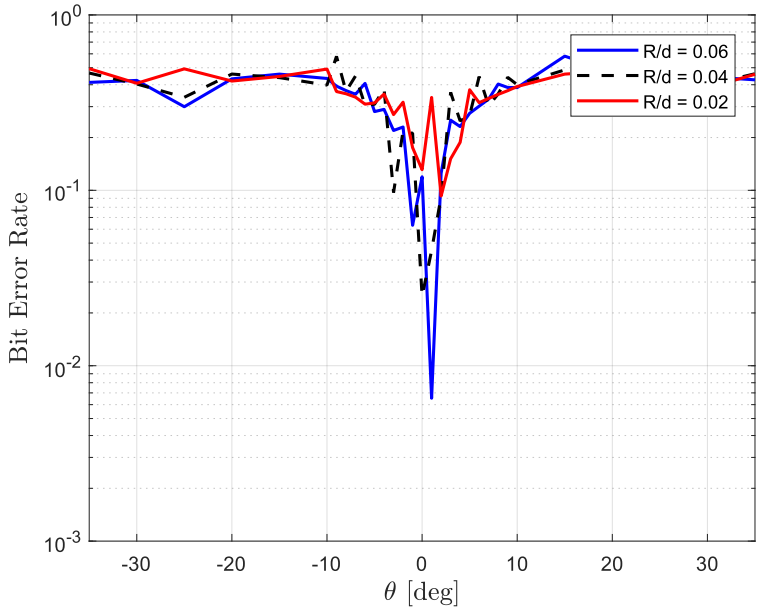

Figure 4.23: BER vs θ showing influence of R

and ratio R/d. It is observed that the performance of SDF deteriorates with increasing R, i.e., the radius within which the scatterers can be found. R on the other is dependent on d, as such deployment of SDF in GBSBM environment is solely pegged on the targeted range and the nature of scatterers in the environment.

Chapter 5

Conclusions and perspective

This research investigated the concept of Spatial Data Focusing (SDF), a technique that has been proposed as a candidate alternative to classical beamforming techniques in wireless geocasting applications. Specifically, we sought to complement our preceding research work that did exploit time and IQ resources to implement SDF, however, experienced challenges in the face of multipath propagation environments. In this PhD, it is proposed to implement spatial data focusing by simultaneously exploiting quadrature components and direct sequence spread spectrum techniques to design an SDF system that is more robust to the effect of multipath. The results obtained thus far give credence to our approach, it has been shown that the spread spectrum based spatial data focusing with IQ is sufficiently robust, even when implemented over modeled multipath environments, this conclusion has been reached based on simulations carried out over various types of multipath environments.

Geocasting, i.e., broadcasting data to pre-defined geographical locations, is pegged largely on dedicated routing protocols designed with the goal of managing tradeoffs between network flooding, latency, overhead, packet delivery and location accuracy. In most of the routing protocols, for every payload, a header is included that solely defines packet address information, both source and destination, and in some cases the complete route graph, as such may lead to privacy issues, given that in most cases participating nodes are required to share their position either with their neighbors or with the infrastructure. Some protocols work around this potential privacy threat by employing global flooding techniques, which are basically topology-free routing protocols that listen to and accept all communication in the network, however on reading the incoming information, it makes decision based on whether the data is addressed to it or not, if the information is addressed to it, it will accept it, otherwise it will automatically forward and then discard.

Whereas this approach looks practical, it is actually resource intensive. As such typical IoT nodes for example may not have adequate resources in terms of computing ability and power to sustain such an activity over long duration. With this limitation they may thus resort to other positioning techniques that depend on infrastructure with fixed positions for supplementary services, such techniques include Angle-of-Arrival and Time-Difference-of-Arrival computations, this takes us back full cycle on the question of resource intensity.

Considering the challenges described above, this PhD research set to mitigate them by proposing and investigating an alternative wireless geocasting technique at the physical layer. To do so, we introduce the concept of spatial selectivity in the broadcast of data at the last mile wireless access. The approach we take is less demanding in terms of both required infrastructure, and routing computations. In essence, we seek to add directional capabilities to base stations allowing them to

wirelessly broadcast data that can only be decoded at pre-defined geographical locations, and so geocasting. Classically geocasting is implemented via power focusing techniques that employ antenna arrays for focusing. The key limitation with this approach is that, to be able to illuminate narrower directions, it is required to proportionally increase the aperture size of the transmitting antenna array, taking us straight back to the question of increasing infrastructure for improved performance and the attendant limitations earlier described.

To overcome this limitation, we proposed the concept of SDF, where data is processed in such a manner that it can only be decoded at predefined locations. In this thesis we did discuss the general concept of geocasting as is implemented in the present, outlining it strengths and limitations. We also highlighted multiple research activities focused in geocasting, most of them found in the Vehicular Ad-hoc Networks area of research. We subsequently reviewed the state of the art of different techniques that enable directional capability in base stations. This includes, beamforming, Directional Modulation and Time Reversal techniques. We then introduced the framework of the proposed spatial data focusing technique. Both numerical and symbolic approach to the scheme have been reviewed in this, work and convergence between the two demonstrated for purposes of proof of concept. For purposes of improving the performance of the scheme, specifically, the question of efficient channel estimation and equalization, the IQ degree of freedom was introduced the scheme, that enabled significant improvement in performance. We finally modeled the scheme over various types of multipath environments to investigate its robustness over such environments. The results show that indeed as was envisaged, the scheme is robust over multipath environments.

We have shown in this thesis that this scheme is spatially more selective than focusing the power and therefore overcomes to a large extent the limitation due to the inversely proportional relationship between beam and aperture size. Future research may be interesting to assess the robustness of the scheme and its capability to perform multipath mitigation with experiments on real streets. Also, the robustness to large angular spread channel should be given full consideration as it has been shown it can jeopardize achieving acceptable BER. Equally the actual design of physical SDF-based system would be a very interesting direction of research.

Publications

Journal

- Odhiambo, M., Molineaux, G., De Doncker, P., Sarrazin, J., "IQ-Direct Sequence Spread-Spectrum Spatial Data Focusing validated over urban canyon 6-ray multipath channel", *to be submitted*

Conferences

- Odhiambo, M., Golstein, S., Sarrazin, J., De Doncker, P., and Horlin, F. "Spatial data focusing, implementation using spread spectrum modulation techniques", JNM, Caen, France, May 2019
- Odhiambo, M., et al. "IQ Based Direct Sequence Spread Spectrum Spatial Data Focusing implemented over a 6 Ray Urban Canyon Channel Model", URSI-France Scientific Days, Palaiseau, France, Mar. 2020, URL:https://hal.sorbonne-universite.fr/hal-02870220
- J. Sarrazin, M. Odhiambo, S. Golstein, P. De Doncker, F. Horlin, "Spatial Data Focusing: An Alternative to Beamforming for Geocasting Scenarios", USNC-URSI Radio Science Meeting (Joint with AP-S Symposium), July 2018, pp. 139–140. DOI:10.1109/USNC-URSI.2018.8602761
- Molineaux, G., Golstein, S., Odhiambo, M., Horlin, F., De Doncker, P., and Sarrazin, J. S. J. “Spatial data focusing using time and IQ resources for wireless geocasting”, Proc. of the IEEE Global Communications Conference, GLOBECOM, 09-13 December, 2019, Waikoloa, HI, USA, Dec. 2019
- G. Molineaux, M. Odhiambo, F. Horlin, P. De Doncker, J. Sarrazin, “OFDM-based Spatial Data Focusing for High Resolution 2-Dimensional Wireless Geocasting”. In:2020 IEEE 31st Annual International Symposium on Personal, Indoor and Mobile Radio Communications. 2020, pp.1–6. DOI:10.1109/PIMRC48278.2020.9217222
- Golstein, S., Odhiambo, M., Horlin, F., De Doncker, P., Sarrazin, J. "Spatial data focusing, implementation using spread spectrum modulation techniques", JNM, Caen, France, May 2019
- Sarrazin, J., Odhiambo, M., Golstein, S., Horlin, F., De Doncker, P., “Spatial Data Focusing: an Alternative to Beamforming in Geocasting Scenarios”, IRACON COST Meeting 2018, Cartagena, Spain, May 2018
- Golstein, S., Odhiambo, M., Horlin, F., De Doncker, P., Sarrazin, J. "Spatial Data Focusing using time resources", IRACON COST Meeting 2019, Dublin, Ireland, Jan. 2019

Bibliography

[1] Aydin Rajaei et al. “Efficient geocasting in opportunistic networks”. In: *Computer Communications* 127 (2018), pp. 105–121.

[2] L. C. Godara. “Application of antenna arrays to mobile communications. II. Beam-forming and direction-of-arrival considerations”. In: *Proceedings of the IEEE* 85.8 (Aug. 1997), pp. 1195–1245. ISSN: 1558-2256. DOI: 10.1109/5.622504.

[3] J. Sarrazin et al. “Spatial Data Focusing: An Alternative to Beamforming for Geocasting Scenarios”. In: *2018 USNC-URSI Radio Science Meeting (Joint with AP-S Symposium)*. July 2018, pp. 139–140. DOI: 10.1109/USNC-URSI.2018.8602761.

[4] J. Razavilar, F. Rashid-Farrokhi, and K. J. R. Liu. “Software radio architecture with smart antennas: a tutorial on algorithms and complexity”. In: *IEEE Journal on Selected Areas in Communications* 17.4 (Apr. 1999), pp. 662–676. ISSN: 1558-0008. DOI: 10.1109/49.761043.

[5] A. Bachir and A. Benslimane. “A multicast protocol in ad hoc networks inter-vehicle geocast”. In: *The 57th IEEE Semiannual Vehicular Technology Conference, 2003. VTC 2003-Spring.* Vol. 4. 2003, 2456–2460 vol.4.

[6] C. Maihofer and R. Eberhardt. “Geocast in vehicular environments: caching and transmission range control for improved efficiency”. In: *IEEE Intelligent Vehicles Symposium, 2004*. 2004, pp. 951–956.

[7] C. Maihöfer, T. Leinmüller, and E. Schoch. “Abiding geocast: Time-stable geocast for ad hoc networks”. In: Jan. 2005, pp. 20–29. DOI: 10.1145/1080754.1080758.

[8] H. Joshi, M. Sichitiu, and M. Kihl. “Distributed Robust Geocast Multicast Routing for Inter-Vehicle Communication”. In: *Proceedings of WEIRD Workshop on WiMax, Wireless and Mobility* (May 2007).

[9] M. Kihl et al. “Reliable Geographical Multicast Routing in Vehicular Ad-Hoc Networks”. In: Jan. 2007, pp. 315–325. DOI: 10.1007/978-3-540-72697-5_27.

[10] T. Atechian and L. Brunie. “DG-CastoR: Direction-based geocast routing protocol for query dissemination in VANET”. In: (Jan. 2008).

[11] Y. Chen, Y. Lin, and S. Lee. “A Mobicast Routing Protocol in Vehicular Ad-Hoc Networks”. In: *GLOBECOM 2009 - 2009 IEEE Global Telecommunications Conference*. 2009, pp. 1–6.

[12] M. Artimy, W. Robertson, and W. Phillips. “Vehicular Ad Hoc Networks: An Emerging Technology Toward Safe and Efficient Transportation”. In: Mar. 2008, pp. 405 –432. ISBN: 9780470396384. DOI: 10.1002/9780470396384.ch14.

[13] B. Balasubramanian, F. Bonomi, and M. Chiang. *Fog for 5G and IoT*. John Wiley & Sons Inc, 2017. ISBN: 9781119187158,111918715X.

[14] Y. Ko and N. Vaidya. "Flooding-Based Geocasting Protocols for Mobile Ad Hoc Networks". In: *MONET* 7 (Dec. 2002), pp. 471–480. DOI: 10.1023/A:1020712802004.

[15] R. Baldessari, C. J. Bernardos, and M. Calderon. "GeoSAC - Scalable address autoconfiguration for VANET using geographic networking concepts". In: *2008 IEEE 19th International Symposium on Personal, Indoor and Mobile Radio Communications*. 2008, pp. 1–7.

[16] Wim Vandenberghe et al. "Vehicular ad hoc networking based on the incorporation of geographical information in the IPv6 header". In: *EURASIP Journal on Wireless Communications and Networking* 2012.1 (2012), p. 316.

[17] B. Karp and H. Kung. "GPSR: Greedy Perimeter Stateless Routing for Wireless Networks". In: *Proceedings of the Annual International Conference on Mobile Computing and Networking, MOBICOM* (Oct. 2000). DOI: 10.1145/345910.345953.

[18] M. Khan et al. "Multicast routing protocols in wireless sensor networks (WSNs)". In: *Journal of Computing* 4 (Sept. 2012), pp. 9–17.

[19] G. Shah, M. Khan, and M. Sher. "A QOS based multicast communication framework for wireless sensor actor networks (WSANS)". In: *International Journal of Innovative Computing, Information and Control (IJICIC)* 7 (Oct. 2011), pp. 7003–7021.

[20] Roberto Baldessari et al. *Car-2-Car Communication Consortium - Manifesto*. Manifesto: Available at http://www.car-to-car.org, last accessed 13. March 2020. Jan. 2007.

[21] EUROPEAN TELECOMMUNICATIONS STANDARDS INSTITUTE. *Intelligent Transport Systems (ITS); Vehicular Communications; GeoNetworking; Part 1: Requirements*. ETSI EN 302 636-1 V1.2.1. CAR 2 CAR Communication Consortium, Feb. 2014.

[22] EUROPEAN TELECOMMUNICATIONS STANDARDS INSTITUTE. *Intelligent Transport Systems (ITS); Vehicular Communications; GeoNetworking; Part 2: Scenarios*. ETSI EN 302 636-2. CAR 2 CAR Communication Consortium, Nov. 2013.

[23] EUROPEAN TELECOMMUNICATIONS STANDARDS INSTITUTE. *Intelligent Transport Systems (ITS); Vehicular Communications; GeoNetworking; Part 3: Network architecture*. ETSI TS 102 636-3 V1.1.1. CAR 2 CAR Communication Consortium, Mar. 2010.

[24] EUROPEAN TELECOMMUNICATIONS STANDARDS INSTITUTE. *Intelligent Transport Systems (ITS); Vehicular Communications; GeoNetworking; Part 4: Geographical addressing and forwarding for point-to-point and point-to-multipoint communications; Sub-part 2: Media-dependent functionalities for ITS-G5*. ETSI TS 102 636-4-2 V1.2.1. CAR 2 CAR Communication Consortium, Apr. 2020.

[25] A. Festag et al. "CAR-2-X Communication SDK - A Software Toolkit for Rapid Application Development and Experimentations". In: *2009 IEEE International Conference on Communications Workshops*. 2009, pp. 1–5.

[26] W. Enkelmann. "FleetNet - applications for inter-vehicle communication". In: *IEEE IV2003 Intelligent Vehicles Symposium. Proceedings (Cat. No.03TH8683)*. 2003, pp. 162–167.

[27] M. Kasemann et al. *A Reactive Location Service for Mobile Ad Hoc Networks*. Technical Report TR-02-014. Department of Computer Science, University of Mannheim, Mar. 2003.

[28] H. Füßler et al. "A position-based router: design, implementation and measurement". In: *Inter-vehicle-communications based on ad hoc networking principles. Hrsg.: W. Franz*. Universitätsverlag Karlsruhe, Karlsruhe, 2005, pp. 145–174. ISBN: 3-937300-88-0.

[29] J. Cheambe, J. Tchouto, and c. Tittel. "The pinboard application: Location based messaging for vehicular communications". In: Jan. 2005, pp. 259–286. DOI: 10.5445/KSP/1000003684.

[30] R. J. Hall et al. "Scaling Up a Geographic Addressing System". In: *MILCOM 2013 - 2013 IEEE Military Communications Conference*. 2013, pp. 143–149.

[31] R. J. Hall. "An Internet of Drones". In: *IEEE Internet Computing* 20.3 (2016), pp. 68–73.

[32] R. J. Hall. "An Improved Geocast for Mobile Ad Hoc Networks". In: *IEEE Transactions on Mobile Computing* 10.2 (2011), pp. 254–266.

[33] Robert Hall and Josh Auzins. "A Tiered Geocast Protocol for Long Range Mobile Ad Hoc Networking". In: *MILCOM* 0 (Oct. 2006), pp. 1–8. DOI: 10.1109/MILCOM.2006.302558.

[34] R. J. Hall. "A Geocast Based File Transfer Protocol". In: *MILCOM 2013 - 2013 IEEE Military Communications Conference*. 2013, pp. 150–156.

[35] M. Chiang, B. Balasubramanian, and F. Bonomi. *Fog for 5G and IoT*. 1st. Wiley Publishing, 2017. ISBN: 1119187133.

[36] R. J. Hall. "The itron family of geocast games". In: *IEEE Transactions on Consumer Electronics* 58.2 (2012), pp. 171–177.

[37] R. Peng and M. L. Sichitiu. "Angle of Arrival Localization for Wireless Sensor Networks". In: *2006 3rd Annual IEEE Communications Society on Sensor and Ad Hoc Communications and Networks*. Vol. 1. 2006, pp. 374–382. DOI: 10.1109/SAHCN.2006.288442.

[38] T. T. Vo et al. "Mutual Coupling Modeling and Calibration in Antenna Arrays for AOA Estimation". In: *2018 2nd URSI Atlantic Radio Science Meeting (AT-RASC)*. 2018, pp. 1–4. DOI: 10.23919/URSI-AT-RASC.2018.8471273.

[39] A. Jafari et al. "UWB Interferometry TDOA Estimation for 60-GHz OFDM Communication Systems". In: *IEEE Antennas and Wireless Propagation Letters* 15 (2016), pp. 1438–1441. DOI: 10.1109/LAWP.2015.2512327.

[40] T. Van der Vorst et al. "Anchor Selection In Angle-Of-Arrival Estimation-Based Localization Using Polynomial Chaos Expansions". In: *2020 IEEE 91st Vehicular Technology Conference (VTC2020-Spring)*. 2020, pp. 1–5. DOI: 10.1109/VTC2020-Spring48590.2020.9129420.

[41] H. Wang and M. Kaveh. "Coherent signal-subspace processing for the detection and estimation of angles of arrival of multiple wide-band sources". In: *IEEE Transactions on Acoustics, Speech, and Signal Processing* 33.4 (1985), pp. 823–831. DOI: 10.1109/TASSP.1985.1164667.

[42] Guowei Shen, R. Zetik, and R. S. Thoma. "Performance comparison of TOA and TDOA based location estimation algorithms in LOS environment". In: *2008 5th Workshop on Positioning, Navigation and Communication*. 2008, pp. 71–78. DOI: 10.1109/WPNC.2008.4510359.

[43] Ahmadreza Jafari et al. "TDOA estimation method using 60 GHz OFDM spectrum". In: *International Journal of Microwave and Wireless Technologies* 7.1 (2015), 31–35. DOI: 10.1017/S1759078714000324.

[44] K. C. Ho, X. Lu, and L. Kovavisaruch. "Source Localization Using TDOA and FDOA Measurements in the Presence of Receiver Location Errors: Analysis and Solution". In: *IEEE Transactions on Signal Processing* 55.2 (2007), pp. 684–696. DOI: 10.1109/TSP.2006.885744.

[45] C. A. Balanis. *Antenna Theory: Analysis and Design*. Wiley-Interscience, 2005.

[46] Upamanyu Madhow. *Introduction to Communication Systems*. Cambridge University Press, 2014. DOI: 10.1017/CBO9781139137058.

[47] W. L. Stutzman and G. A.nThiele. *Antenna Theory and Design, 3rd Edition*. New York: Wiley, 2013, p. 304.

[48] K. McClaning. *Wireless receiver design for digital communications*. 2nd ed. Rayleigh, NC: SciTech Publishing, 2011. Chap. 6.

[49] G. Lloyd M. Reil. *Millimeter-wave beamforming: Antenna arrays and characterization*. White Paper. Rohde and Schwarz, 2016.

[50] C. Powell. *Technical Analysis: Beamforming vs MIMO Antennas*. White Paper. Radio Frequency Systems, 2014.

[51] S. Ahmadi. *5G NR, Architecture, Technology, Implementation, and Operation of 3GPP New Radio Standards*. Academic Press, 2019. ISBN: 978-0-08-102267-2.

[52] X. Gu et al. "W-band scalable phased arrays for imaging and communications". In: *IEEE Communications Magazine* 53.4 (2015), pp. 196–204.

[53] M. Emmelmann, B. Bochow, and C. Kellum. "Vehicular Networking: Automotive Applications and Beyond". In: *Fraunhofer FOKUS* (Apr. 2010). DOI: 10.1002/9780470661314.

[54] V. Navda et al. "MobiSteer: using steerable beam directional antenna for vehicular network access". In: *MobiSys '07*. 2007.

[55] P. Subramanian A et al. "A measurement study of inter-vehicular communication using steerable beam directional antenna". In: *VANET '08*. 2008.

[56] H. Stübing, A. Shoufan, and S. A. Huss. "Integrating Secure Beamforming into Car-to-X Architectures". In: *SAE Int. J. Passeng. Cars – Electron. Electr. Syst.* V120-7 (2011), p. 9. ISSN: 1946-4614. DOI: 10.4271/2011-01-0204.

[57] H. Stübing, A. Shoufan, and S. A. Huss. "Enhancing Security and Privacy in C2X Communication by Radiation Pattern Control". In: *2010 IEEE 71st Vehicular Technology Conference*. 2010, pp. 1–5.

[58] H. Stübing, A. Shoufan, and S. A. Huss. "Secure C2X Communication based on Adaptive Beamforming". In: *14. VDI International Conference on Electronic for Vehicles, Baden-Baden*. 2009. URL: http://tubiblio.ulb.tu-darmstadt.de/99648/.

[59] Working Group Communication. *TF Antenna Status Report*. Task Force Antenna, Status Report 3.0. C2C-CC, 2011.

[60] H. Stübing, A. Shoufan, and S. A. Huss. "A Demonstrator for Beamforming in C2X Communication". In: *2010 IEEE 71st Vehicular Technology Conference*. 2010, pp. 1–2.

[61] H. Stübing and A. Jaeger. "Secure Beamforming for Weather Hazard Warning Application in Car-to-X Communication". In: *Design Methodologies for Secure Embedded Systems*. Ed. by Alexander Biedermann and H. Gregor Molter. Berlin, Heidelberg: Springer Berlin Heidelberg, 2011, pp. 187–206. ISBN: 978-3-642-16767-6.

[62] Hagen Stübing. "Multilayered security and privacy protection in Car-to-X networks: solutions from application down to physical layer". PhD thesis. Darmstadt University of Technology, 2013. ISBN: 978-3-658-02530-4. URL: http://d-nb.info/1033489484.

[63] W. Stallings. *Wireless communications and networks*. Upper Saddle River, New Jersey, USA: Prentice-Hall, 2002.

[64] Matthieu Bloch and Joao Barros. *Physical-layer security: from information theory to security engineering*. Cambridge ; New York: Cambridge University Press, 2011. ISBN: 9780521516501.

[65] A. Mukherjee et al. "Principles of Physical Layer Security in Multiuser Wireless Networks: A Survey". In: *IEEE Communications Surveys Tutorials* 16.3 (2014), pp. 1550–1573.

[66] M. P. Daly and J. T. Bernhard. "Directional Modulation Technique for Phased Arrays". In: *IEEE Transactions on Antennas and Propagation* 57.9 (2009), pp. 2633–2640.

[67] M. P. Daly, E. L. Daly, and J. T. Bernhard. "Demonstration of Directional Modulation Using a Phased Array". In: *IEEE Transactions on Antennas and Propagation* 58.5 (2010), pp. 1545–1550.

[68] Y. Ding and V. F. Fusco. "A Vector Approach for the Analysis and Synthesis of Directional Modulation Transmitters". In: *IEEE Transactions on Antennas and Propagation* 62.1 (2014), pp. 361–370.

[69] Y. Ding and V. Fusco. "Vector representation of Directional Modulation transmitters". In: *The 8th European Conference on Antennas and Propagation (EuCAP 2014)*. 2014, pp. 367–371.

[70] Yuan Ding and Vincent Fusco. "A Review of Directional Modulation Technology". In: *International Journal of Microwave and Wireless Technologies* -1 (July 2015). DOI: 10.1017/S1759078715001099.

[71] Y. Ding and V. Fusco. "BER Driven Synthesis for Directional Modulation Secured Wireless Communication". In: *International Journal of Microwave and Wireless Technologies* 6 (Oct. 2013). DOI: 10.1017/S1759078713000913.

[72] H. Shi and A. Tennant. "Secure physical-layer communication based on directly modulated antenna arrays". In: *2012 Loughborough Antennas Propagation Conference (LAPC)*. 2012, pp. 1–4.

[73] H. Shi and A. Tennant. "Enhancing the security of communication via directly modulated antenna arrays". In: *IET Microwaves, Antennas Propagation* 7.8 (2013), pp. 606–611.

[74] S. HongZhe and T. Alan. "Direction dependent antenna modulation using a two element array". In: *Proceedings of the 5th European Conference on Antennas and Propagation (EUCAP)*. 2011, pp. 812–815.

[75] H. Shi and A. Tennant. "Characteristics of a two element direction dependent antenna array". In: *2011 Loughborough Antennas Propagation Conference*. 2011, pp. 1–4.

[76] H. Z. Shi and A. Tennant. "An experimental two element array configured for directional antenna modulation". In: *2012 6th European Conference on Antennas and Propagation (EUCAP)*. 2012, pp. 1624–1626.

[77] H. Shi and A. Tennant. "Secure communications based on directly modulated antenna arrays combined with multi-path". In: *2013 Loughborough Antennas Propagation Conference (LAPC)*. 2013, pp. 582–586.

[78] H. Shi and A. Tennant. "Covert communication using a directly modulated array transmitter". In: *The 8th European Conference on Antennas and Propagation (EuCAP 2014)*. 2014, pp. 352–354.

[79] H. Shi and A. Tennant. "Simultaneous, Multichannel, Spatially Directive Data Transmission Using Direct Antenna Modulation". In: *IEEE Transactions on Antennas and Propagation* 62.1 (2014), pp. 403–410.

[80] T. Hong, M. Song, and Y. Liu. "Dual-Beam Directional Modulation Technique for Physical-Layer Secure Communication". In: *IEEE Antennas and Wireless Propagation Letters* 10 (2011), pp. 1417–1420. ISSN: 1548-5757. DOI: 10.1109/LAWP.2011.2178384.

[81] T. Mavridis et al. "Information Spatial Focusing Scheme for UWB Wireless Communications in Smart Environments". In: *IEEE Antennas and Wireless Propagation Letters* 14 (2015), pp. 20–23. DOI: 10.1109/LAWP.2014.2354059.

[82] Feng Shu et al. *Directional Modulation: A Secure Solution to 5G and Beyond Mobile Networks*. 2018. arXiv: 1803.09938 [cs.IT].

[83] Jinsong Hu, Feng Shu, and Jun Li. "Robust Synthesis Method for Secure Directional Modulation With Imperfect Direction Angle". In: *IEEE Communications Letters* 20.6 (June 2016), pp. 1084–1087. ISSN: 1089-7798. DOI: 10.1109/LCOMM.2016.2550022. URL: http://ieeexplore.ieee.org/document/7446283/ (visited on 01/05/2021).

[84] Christopher M. Bishop. *Pattern recognition and machine learning*. Information science and statistics. New York: Springer, 2006. ISBN: 9780387310732.

[85] Siming Wan et al. "Power Allocation Strategy of Maximizing Secrecy Rate for Secure Directional Modulation Networks". In: *IEEE Access* 6 (2018), pp. 38794–38801. ISSN: 2169-3536. DOI: 10.1109/ACCESS.2018.2815779. URL: https://ieeexplore.ieee.org/document/8315448/ (visited on 01/05/2021).

[86] Yunhua Zhang, Yuan Ding, and Vincent Fusco. "Sidelobe Modulation Scrambling Transmitter Using Fourier Rotman Lens". In: *IEEE Transactions on Antennas and Propagation* 61.7 (July 2013), pp. 3900–3904. ISSN: 0018-926X, 1558-2221. DOI: 10.1109/TAP.2013.2254453. URL: http://ieeexplore.ieee.org/document/6484901/ (visited on 01/05/2021).

[87] Yuan Ding and Vincent F. Fusco. "Establishing Metrics for Assessing the Performance of Directional Modulation Systems". In: *IEEE Transactions on Antennas and Propagation* 62.5 (May 2014), pp. 2745–2755. ISSN: 0018-926X, 1558-2221. DOI: 10.1109/TAP.2014.2307318. URL: https://ieeexplore.ieee.org/document/6746064 (visited on 01/05/2021).

[88] M. Fink. "TIME-REVERSED ACOUSTICS". In: *Scientific American* 281.5 (1999), pp. 91–97. ISSN: 00368733, 19467087. URL: http://www.jstor.org/stable/26058488.

[89] M. Fink et al. "Time-reversed acoustics". In: *Reports on Progress in Physics* 63.12 (Dec. 2000), pp. 1933–1995. DOI: 10.1088/0034-4885/63/12/202. URL: https://doi.org/10.1088%2F0034-4885%2F63%2F12%2F202.

[90] S. Kim et al. "Spatial resolution of time-reversal arrays in shallow water". In: 2001.

[91] W. Hodgkiss et al. "A long-range and variable focus phase-conjugation experiment in shallow water". In: *Journal of the Acoustical Society of America* 105 (1999), pp. 1597–1604.

[92] G. F. Edelmann et al. "An initial demonstration of underwater acoustic communication using time reversal". In: *IEEE Journal of Oceanic Engineering* 27.3 (2002), pp. 602–609. DOI: 10.1109/JOE.2002.1040942.

[93] S. Kim et al. "Robust time reversal focusing in the ocean." In: *The Journal of the Acoustical Society of America* 114 1 (2003), pp. 145–57.

[94] G. Lerosey et al. "Time reversal of electromagnetic waves and telecommunication". In: *Radio Science* 40.06 (2005), pp. 1–10. DOI: 10.1029/2004RS003193.

[95] B. Henty and D. Stancil. "Multipath-enabled super-resolution for rf and microwave communication using phase-conjugate arrays." In: *Physical review letters* 93 24 (2004), p. 243904.

[96] Kyritsi et al. "MISO time reversal and delay-spread compression for FWA channels at 5 GHz". In: *IEEE Antennas and Wireless Propagation Letters* 3 (2004), pp. 96–99. DOI: 10.1109/LAWP.2004.830015.

[97] P. Kyritsi et al. "Time reversal techniques for wireless communications". In: *IEEE 60th Vehicular Technology Conference, 2004. VTC2004-Fall. 2004*. Vol. 1. 2004, 47–51 Vol. 1. DOI: 10.1109/VETECF.2004.1399917.

[98] Hung Tuan Nguyen et al. "Time reversal in wireless communications: a measurement-based investigation". In: *IEEE Transactions on Wireless Communications* 5.8 (2006), pp. 2242–2252. DOI: 10.1109/TWC.2006.1687740.

[99] P. Blomgren et al. "Spatial Focusing and Intersymbol Interference in Multiple-Input–Single-Output Time Reversal Communication Systems". In: *IEEE Journal of Oceanic Engineering* 33.3 (2008), pp. 341–355. DOI: 10.1109/JOE.2008.925083.

[100] S. Golstein et al. "Physical Layer Security in Frequency-Domain Time-Reversal SISO OFDM Communication". In: *2020 International Conference on Computing, Networking and Communications (ICNC)*. 2020, pp. 222–227. DOI: 10.1109/ICNC47757.2020.9049811.

[101] Sidney Jonathan Golstein et al. *Physical Layer Security in a SISO Communication using Frequency-Domain Time-Reversal OFDM Precoding and Artificial Noise Injection*. 2020. arXiv: 2011.06840 [cs.IT].

[102] Q. Xu et al. "Security-Aware Waveform and Artificial Noise Design for Time-Reversal-Based Transmission". In: *IEEE Transactions on Vehicular Technology* 67.6 (2018), pp. 5486–5490. DOI: 10.1109/TVT.2018.2813318.

[103] S. Li et al. "Artificial noise inserted secure communication in time-reversal systems". In: *2018 IEEE Wireless Communications and Networking Conference (WCNC)*. 2018, pp. 1–6. DOI: 10.1109/WCNC.2018.8377356.

[104] S. Li et al. "Artificial noise aided path selection for secure TR communications". In: *2017 IEEE/CIC International Conference on Communications in China (ICCC)*. 2017, pp. 1–6. DOI: 10.1109/ICCChina.2017.8330343.

[105] Richard B. Ertel et al. "Overview of spatial channel models for antenna array communication systems". English (US). In: *Adaptive Antennas for Wireless Communications*. United States: John Wiley and Sons Inc., Jan. 2009, pp. 20–32. ISBN: 0780360168. DOI: 10.1109/9780470544075.ch1.

[106] Hans Steyskal. "Digital beamforming antennas - An introduction". In: *Microwave Journal* 30 (Jan. 1987), p. 107.

[107] D. Parker and D. C. Zimmermann. "Phased arrays - part 1: theory and architectures". In: *IEEE Transactions on Microwave Theory and Techniques* 50.3 (2002), pp. 678–687.

[108] J Blass. "Multidirectional antenna—a new approach to stacked beams". In: *IRE International Convention Record. New York (NY)* 8 (Mar. 1960), pp. 48–50.

[109] Molineaux, G., Golstein, S., Odhiambo, M., Horlin, F., De Doncker, P., & Sarrazin, J. S. J. "Spatial data focusing using time and IQ resources for wireless geocasting". In: *Proc. of the IEEE Global Communications Conference, GLOBECOM (09-13 December, 2019: Waikoloa, HI, USA)*. Dec. 2019.

[110] G. Molineaux et al. "OFDM-based Spatial Data Focusing for High Resolution 2-Dimensional Wireless Geocasting". In: *2020 IEEE 31st Annual International Symposium on Personal, Indoor and Mobile Radio Communications*. 2020, pp. 1–6. DOI: 10.1109/PIMRC48278.2020.9217222.

[111] Golstein, S., Odhiambo, M., Horlin, F., De Doncker, P., Sarrazin, J. "Spatial data focusing, implementation using spread spectrum modulation techniques". In: *Actes des 21èmes Journées Nationales Micro-ondes, JNM (15-17 May, 2019: Caen, France)*. May 2019.

[112] Sarrazin, J., Odhiambo, M., Golstein, S., Horlin, F., De Doncker, P., "Spatial Data Focusing: an Alternative to Beamforming in Geocasting Scenarios". In: *IRACON COST Meeting 2018,Cartagena, Spain)*. May 2018.

[113] Golstein, S., Odhiambo, M., Horlin, F., De Doncker, P., Sarrazin, J. "Spatial Data Focusing using time resources". In: *IRACON COST Meeting 2019, Dublin, Ireland)*. Jan. 2019.

[114] Odhiambo, M., Golstein, S., Sarrazin, J. S. J., De Doncker, P., & Horlin, F. "Spatial data focusing, implementation using spread spectrum modulation techniques". In: *Actes des 21èmes Journées Nationales Micro-ondes, JNM (15-17 May, 2019: Caen, France)*. May 2019.

[115] Michael Odhiambo et al. "IQ Based Direct Sequence Spread Spectrum Spatial Data Focusing implemented over a 6 Ray Urban Canyon Channel Model". In: *Conference URSI-France 2020*. URSI-France Scientific Days. Palaiseau, France, Mar. 2020. URL: https://hal.sorbonne-universite.fr/hal-02870220.

[116] V. P. Ipatov. *Spread Spectrum and CDMA: Principles and Applications*. New York, NY, USA: John Wiley and Sons, 2005.

[117] G. J. Proakis. *Digital Communications*. New York, NY, USA: McGraw-Hill, 2008.

[118] T. S. Rappaport. *Wireless communications principles and practice*. 2nd ed. Upper Saddle River, NJ, USA: Prentice Hall, 2002.

[119] P. Wang, J. Xiao, and L. Ping. "Comparison of orthogonal and non-orthogonal approaches to future wireless cellular systems". In: *IEEE Vehicular Technology Magazine* 1.3 (2006), pp. 4–11.

[120] B. M. Popovic. "Generalized chirp-like polyphase sequences with optimum correlation properties". In: *IEEE Transactions on Information Theory* 38.4 (1992), pp. 1406–1409.

[121] L. P. Linde and J. D. Vlok. "Power and spectrally efficient four-dimensional super-orthogonal WCDMA building block for next generation wireless applications". In: *IEEE Communications Letters* 10.7 (2006), pp. 519–521.

[122] D. Huffman. "The generation of impulse-equivalent pulse trains". In: *IRE Transactions on Information Theory* 8.5 (1962), pp. 10–16.

[123] U. Parlitz and S. Ergezinger. "Robust communication based on chaotic spreading sequences". In: *Physics Letters A* 188.2 (1994), pp. 146 –150. ISSN: 0375-9601. DOI: https://doi.org/10.1016/0375-9601(84)90009-4.

[124] B. Sklar. *Digital Communications: Fundamentals and Applications, 2nd Ed.* Prentice Hall, 2001.

[125] R. L. Peterson, R. E. Ziemer, and D. E. Borth. *Introduction to Spread Spectrum Communications*. 1st ed. Prentice Hall International Editions, 1995.

[126] Y. Lin. "'Shift and add' property of m-sequences and its application to channel characterisation of digital magnetic recording". In: *IEE Proceedings - Communications* 142.3 (1995), pp. 135–140.

[127] S. W. Golomb. *Shift Register Sequences*. 1st ed. Holden-Day, 1967.

[128] E. H. Dinan and B. Jabbari. "Spreading codes for direct sequence CDMA and wideband CDMA cellular networks". In: *IEEE Communications Magazine* 36.9 (1998), pp. 48–54.

[129] L. Ariel and H. Motti. *Wireless Transceiver Design: Mastering the Design of Modern Wireless Equipment and Systems*. 2nd ed. Wiley, 2016. ISBN: 1118937406.

[130] D. V. Sarwate and M. B. Pursley. "Crosscorrelation properties of pseudorandom and related sequences". In: *Proceedings of the IEEE* 68.5 (1980), pp. 593–619.

[131] S. Golomb and R. Scholtz. "Generalized Barker sequences". In: *IEEE Transactions on Information Theory* 11.4 (1965), pp. 533–537.

[132] R. Turyn and J. Storer. "On Binary Sequences". In: *Proceedings of the American Mathematical Society* 12.3 (1961), pp. 394–399. ISSN: 00029939, 10886826. URL: http://www.jstor.org/stable/2034204.

[133] D. G. Luenberger. "On Barker codes of even length". In: *Proceedings of the IEEE* 51.1 (1963), pp. 230–231.

[134] C. k. Chan and W. H. Lam. "Generalised Barker-like PN sequences for quasisynchronous spread-spectrum multiple-access communication systems". In: *Communications, IEE Proceedings-* 142 (May 1995), pp. 91 –98. DOI: 10.1049/ip-com:19951854.

[135] Xianbin Wang, Y. Wu, and B. Caron. "Transmitter identification using embedded pseudo random sequences". In: *IEEE Transactions on Broadcasting* 50.3 (2004), pp. 244–252.

[136] V. Milosevic, V. Delic, and V. Senk. "Hadamard transform application in speech scrambling". In: *Proceedings of 13th International Conference on Digital Signal Processing*. Vol. 1. 1997, 361–364 vol.1.

[137] Tai-Kuo Woo. "Orthogonal variable spreading codes for wideband CDMA". In: *IEEE Transactions on Vehicular Technology* 51.4 (2002), pp. 700–709.

[138] F. Adachi et al. "Coherent Multicode DS-CDMA Mobile Radio Access". In: *IEICE Transactions on Communications* 79 (1996), pp. 1316–1325.

[139] L. Hanzo et al. *OFDM and MC-CDMA for broadband multi-user communications, WLANs, and broadcasting*. J. Wiley, 2003. ISBN: 0470858796.

[140] S. Jos, P. Kumar, and S. Chakrabarti. "Performance Comparison of Orthogonal Gold and Walsh Hadamard Codes for Quasi-Synchronous CDMA Communication". In: Jan. 2009, pp. 395–399. DOI: 10.1007/978-3-540-92295-7_47.

[141] Don Torrieri. *Principles of Spread-Spectrum Communication Systems*. 4th ed. Springer International Publishing, 2018. ISBN: 978-3-319-70568-2,978-3-319-70569-9.

[142] R. C. Dixon. *Spread spectrum systems with commercial applications*. 3rd ed. New York, NY, USA: John Wiley and Sons, 1994.

[143] G. Turin. "An introduction to matched filters". In: *IRE Transactions on Information Theory* 6.3 (1960), pp. 311–329.

[144] A. Goldsmith. "Wireless communications, 1st. ed". In: New York, NY, USA: Cambridge Univ. Press, 2005. Chap. 13-14.

[145] M. B. Pursley. "Direct-sequence spread-spectrum communications for multipath channels". In: *IEEE Transactions on Microwave Theory and Techniques* 50.3 (2002), pp. 653–661.

[146] P. Kyösti. *Radio channel modelling for 5G telecommunication system evaluation and over the air testing. D.Sc dissertation*. University of Oulu, 2018.

[147] 3GPP. *Circular angle spread. Teleconference, 3rd Generation Partnership Project (3GPP)*. 2003.

[148] 38.901 (2018). *Study on channel model for frequencies from 0.5 to 100 GHz. Technical Specification (TS) Release 15, 3rd Generation Partnership Project (3GPP).* IEEE personal communications, vol. 5, no. 1, pp. 10–22. 2018.

[149] D. Bojanjac, R. Nađ, and G. Šišul. "Ray tracing model of pedestrian urban zone". In: *Proceedings ELMAR-2010*. Sept. 2010, pp. 289–292.

[150] P. Petrus, J. H. Reed, and T. S. Rappaport. "Geometrically based statistical channel model for macrocellular mobile environments". In: *Proceedings of GLOBECOM'96. 1996 IEEE Global Telecommunications Conference*. Vol. 2. 1996, 1197–1201 vol.2.

[151] J. C. Liberti and T. S. Rappaport. "A geometrically based model for line-of-sight multipath radio channels". In: *Proceedings of Vehicular Technology Conference - VTC*. Vol. 2. 1996, 844–848 vol.2.

[152] P. Petrus, J. H. Reed, and T. S. Rappaport. "Geometrical-based statistical macrocell channel model for mobile environments". In: *IEEE Transactions on Communications* 50.3 (2002), pp. 495–502.